UNIVERSITY OF CAPE COAST

OPTICAL STUDIES AND CHARACTERIZATION OF *PLASMODIUM FALCIPARUM* INFECTED HUMAN RED BLOOD CELLS

JERRY OPOKU-ANSAH

2016

© Jerry Opoku-Ansah

University of Cape Coast

UNIVERSITY OF CAPE COAST

OPTICAL STUDIES AND CHARACTERIZATION OF *PLASMODIUM*

FALCIPARUM INFECTED HUMAN RED BLOOD CELLS

BY

JERRY OPOKU-ANSAH

Thesis submitted to the Department of Physics of the School of Physical Sciences, College of Agriculture and Natural Sciences, University of Cape Coast, in partial fulfilment of the requirements for the award of Doctor of Philosophy Degree in Physics

JULY 2016

DECLARATION

Candidate's Declaration

I hereby declare that this thesis is the result of my own original research and
that no part of it has been presented for another degree in this university or
elsewhere.

…………………………..   Date: …………………

Jerry Opoku-Ansah

(Candidate)

Supervisors' Declaration

We hereby declare that the preparation and presentation of the thesis were
supervised in accordance with the guidelines on supervision of thesis laid
down by the University of Cape Coast.

………………………….   Date: …………………

Prof. Moses Jojo Eghan
 (Principal Supervisor)

………………………….   Date: ………………….

Prof. Johnson Nyarko Boampong
(Co-Supervisor)

ii

ABSTRACT

In this work, three optical techniques: spectral imaging, laser-induced fluorescence (LIF) and spectrophotometry were used to study and characterize uninfected red blood cells (RBCs) (*u*-RBCs) and *P.falciparum* infected RBCs (*i*-RBCs). Unstained blood smear slides were prepared from blood samples of volunteers who were tested positive for *P.falciparum* infections (*i*-blood) and after treatment (*u*-blood). Optical characteristics of the *i*-RBCs in spectral images, captured in reflection, scattering and transmission modes, showed increased transmission, and decreased reflection and scattering of light intensity. Histograms fitted with Gaussian curves of aspect ratio (AR) and integrated optical density (IOD) showed mean AR value <1.2 and IOD <2000 a.u for *u*-RBCs, AR 1.5-2.0 and IOD 5000-13000 a.u for the *i*-RBCs. In identifying the *u*-RBCs and the *i*-RBCs in ring, trophozoite and schizont stages, two spectral bands: 435 nm and 660 nm were found to be common markers in all the three modes. Another spectral band, 470 nm was found to be a shared marker in both reflection and scattering modes. In transmission mode, 590 nm, 625 nm and 700 nm were identified as unique markers for the ring, trophozoite and schizont stages respectively. In both reflection and scattering modes, 525 nm, the 590 nm and the 625 nm were found to be single markers for the ring, trophozoite and schizont stages respectively. LIF results revealed that spectra peak wavelengths of *i*-blood were red-shifted. The LIF spectra of *i*-blood samples under Lorentzian curves showed increase in fluorescence spectra peak intensity ratio. The spectrophotometry technique showed reduction in haemoglobin of *i*-blood at blood absorption bands. These optical techniques may be potentially applied for improved *P.falciparum* diagnosis.

KEYWORDS

Laser-induced fluorescence

Malaria diagnosis

Optical techniques

Parasite density

Plasmodium falciparum

Principal component analysis (PCA)

Red blood cells (RBCs)

Spectral bands

Spectral imaging

Spectrophometry

ACKNOWLEDGEMENTS

This thesis would not have come to a successful completion without the support of numerous people who have contributed in diverse ways. First and foremost, I am extremely grateful to Prof. Moses Jojo Eghan, my principal supervisor and Prof. Johnson Nyarko Boampong, my co-supervisor, for their tremendous mentoring, insightful supervision, valuable guidance, scholarly inputs and consistent encouragement I received throughout my development as a researcher.

I would especially like to express my sincere appreciation to the Office of the External Activity of the Abdus Salam International Centre for Theoretical Physics, Italy and the International Science Programme (ISP) of Uppsala University, Sweden for financial support. I appreciatively thank all members of the African Spectral Imaging Network (AFSIN) for valuable advice in science discussions. Many thanks go to all Professors, lecturers and staff, both teaching and non-teaching of the Department of Physics especially Dr. Benjamin Anderson for their support. All members of LAFOC research group have all extended their support in a very special way, and I gained a lot from them, through their personal and scholarly interactions, their suggestions at various points of my research programme. I am also grateful to the entire administrative staff of LAFOC for their unflinching support.

I am much indebted to my wife, Elizabeth, and my cherished children, Jerica and Jerry Jr. for their unparalleled sacrifices, spiritual and moral support in this feat. My sincere thanks go to all other people who were behind my progress throughout my studies. Pardon me if I did not mention your name.

DEDICATION

I dedicate this thesis to my family for constant support and unconditional love.

I love you all dearly.

TABLE OF CONTENTS

LIST OF TABLES

LIST OF FIGURES

xiv

xviii

LIST OF PLATES

LIST OF ABBREVIATIONS

CDC	Centre for Diseases Control
DFID	Department for International Development
dHb	Deoxygenated Haemoglobin
ERC	Ethical Review Committee
GHS	Ghana Health Service
Hb	Haemoglobin
IR	Infra-Red
HbO_2	Oxygenated Haemoglobin
NIR	Near Infra-Red
PCA	Principal Component Analysis
RBCs	Red Blood Cells
UV	UltraViolet
VIS	Visible

CHAPTER ONE

INTRODUCTION

Background

Optical techniques are methods of using light to investigate samples and provide useful information out of the samples. The optical techniques involve the use of excitation light sources from the optical region, that is, ultraviolet (UV), visible (VIS) and infrared (IR) regions of the electromagnetic (EM) spectrum (Demtroder, 2003; Svanberg, 2012). Excitations from the optical region bring about electronic, vibrational and rotational transitions. Electronic transitions are provided by the UV and the VIS excitations while vibrational and/or rotational transitions are provided by the IR excitations. Therefore, optical techniques when applied, carry information about electronic, vibrational and rotational transitions. Due to their low demands on instrumentations and no sample preparation requirement, optical techniques tend to provide useful information for studying the samples. The fingerprints of the optical techniques allow for differentiated statement about different molecular samples (Anderson et al., 2004; Tuchin, 2007; Jacques & Pogue, 2008; Svanberg, 2012). The back-bone of the optical techniques involves photon transport which usually starts with the measurement of reflection, transmission, absorption, scattering or fluorescence properties of the sample. These basic optical properties of the sample unearth features such as molecular composition, crystal structure, scattering coefficient and absorption coefficient of the sample.

1

Optical techniques are the most promising, multidisciplinary and valuable techniques being applied in a vast range of research fields ranging from biomedicine, through zoology, remote sensing, food sciences, and to agriculture due to their often nondestructive and noninvasive nature as well as their rapid evaluation possibilities (Svanberg, 2004; 2009; Ellis et al., 2005; Brydegaard et al., 2011; Aparicio & Harwood, 2013). They are said to be the available techniques that can provide cellular or molecular level information, with almost single molecule sensitivity, allowing probing of cellular structure and dynamics for understanding of the mechanisms of physiological regulation (Michaelis, et al., 2000; Prasad, 2003). Optical techniques have been utilized as powerful tools for environmental monitoring, air quality monitoring, water and vegetation status assessment, as well as flying insect identifications via remote sensing. Besides, optical diagnostic techniques have been remotely used for quantifying agricultural and epidemiological importance (Anderson et al., 2004; Svanberg, 2004; Brydegaard et al., 2011). They are routinely used to identify and study compounds, and complex mixtures. The usefulness of optical techniques results from the characteristic and distinctive interaction of each compound with EM radiation (Milosevic & Berets, 1993).

With regards to applications of optical techniques, instrumentations for nuclear magnetic resonance spectroscopy (NMRS), X-ray emission spectroscopy (XES), ultraviolet (UV)-visible(VIS) (UV-VIS) spectroscopy, Fourier transform infrared spectroscopy (FTIRS), Absorption spectroscopy (AS), fluorescence spectroscopy (FS) and Raman spectroscopy (RS) represent some of the common measurement techniques for atomic and molecular

2

studies of samples. For example, XES is a surface-sensitive quantitative technique that measures the elemental composition at parts per thousand range, empirical formula, chemical state and electronic state of the elements that exist within the sample. The XES spectra are obtained by irradiating the sample with a beam of X-rays while simultaneously measuring the kinetic energy and number of electrons that escape between 0 to 10 nm of the sample being studied. FTIRS uses excitations from lower frequencies to provide vibrational information of the molecules present in a given sample (Nakamoto, 1977; Colthup, 2012). To avoid absorption of water which destroys the measured spectra of samples, detections in the IR region requires that sample preparations are done with either Nujul oil or Potassium Bromide (KBr) (Harwood et al., 1989). A RS is a technique based on inelastic scattering of monochromatic light source, usually from a laser source, observing a change in frequency of scattered light originating from a sample exposed to the monochromatic light source (Raman, & Krishnan, 1928). The inelastic scattered photons are observed as spectral peaks so that by analyzing the location and amplitude of these peaks in the EM spectrum, chemical composition of the sample can be identified (Lewis, & Edwards, 2001; McCreery, 2005).

Absorption measurement techniques can equally be used to investigate the presence of molecular species having energies which are in resonance with the spectral line(s) of the radiation source (Knee, 1996). Some examples of AS measurement techniques include tunable diode laser absorption spectroscopy (TDLAS), differential optical absorption spectroscopy (DOAS), wavelength modulation spectroscopy (WMS), differential absorption light detection and

3

ranging (LIDAR) (DIAL) and gas in scattering medium absorption spectroscopy (GASMAS) (Sigrist, 1994; Platt & Stutz 2008). Using WMS technique, even in the presence of a large background, an implanted gas produces minute but thin signal that can be detected by the GASMAS technique (Sjöholm et al., 2001; Somesfalean et al., 2002). The GASMAS technique provides new opportunities for studying gases enclosed in a natural or a synthetic material. This new technique can be used for characterization and diagnosis of free gases in scattering solids and turbid liquids.

Fluorescence spectroscopy (FS) is another common optical technique in which emissions due to the actual absorption of photons into an atom is studied (Sauer et al., 2010). Fluorescence emission is caused by electronic transitions of atoms and this occurs in the optical region of the EM spectrum. This technique is appropriate for analyzing molecules because of its sensitivity and specificity (Lakowicz, 2006). Fluorescence emissions depend on the excitation wavelength. Generally not all substances do fluoresce for a particular excitation. This makes FS a frequency dependent phenomenon. In FS, three basic elements can be considered: a source of light, a sample holder, and a detector. The light source can be lasers, light emitting diodes (LEDs) and lamps. These light sources have spectral outputs either as a continuum of energy over a wide range or as a series of discrete lines. Majority of the light sources in FS instrumentation lack stability over long periods. Currently, lasers are commonly used as sources in FS to overcome this challenge (de Oliveira Silva et al., 2010; Kalnina et al., 2010; Al-Salhi et al., 2011; Masilamani et al., 2011).

4

Laser-induced fluorescence (LIF) is a type of optical spectroscopic technique which analyzes fluorescence of a sample. This photonic process involves transitions between electronic and vibrational states of polyatomic fluorescent molecules (fluorophores). LIF has numerous measurement aspects, including its intensity and excitation wavelength. Quantities such as fluorescence decay time, anisotropy, polarization conditions, quantum yields and Stokes' shifts, which can be accessible for analysis, are also associated with LIF. These parameters for the detection of samples allow alleviating some difficulties which may occur when applying LIF, for example, matrix and quenching effects. There are also cases where one parameter may give little or no information at all; in this case, other parameters may be used. However, there are substances which show an extremely low fluorescence yield or even no fluorescence at all due to other fast decay pathways such as intersystem crossing. When using LIF, the extraordinary characteristics such as high spectral intensity and well defined wavelength of the lasers are specifically utilized. These allow for a selective excitation of samples and manufacturing of compact instruments. By using LIF, it is possible to record the excitation spectra and the excitation wavelength as an additional parameter (Barocsi et al., 2000; Gustafsson et al., 2000; Anderson et al., 2004).

Laser-induced fluorescence is a photon emission process that occurs during molecular relaxation from electronic excited states. In this spectroscopy, generally, light is issued by the excitation laser source through a unified candidate or waves and collides with the sample. The sample absorbs part of the incident light and fluorescence happens in the sample. LIF reflects the structural characteristics of endogenous spectra of fluorophores inside

5

tissue (Fauaz et al., 2010). LIF diagnostic methods have been used to investigate the structural and spectral characteristics of normal and diseased tissues for differentiation (Bengtsson et al., 2005; Karadaglic et al., 2009; de Goes Rocha et al., 2010; Fauaz et al., 2010). Fluorescence as well as other optical techniques are also applied for imaging of samples. These optical imaging techniques include fluorescence imaging (FI), X-ray imaging (XRI), magnetic resonance imaging (MRI) and spectral imaging (SI) (Kane & Lee, 2007; Demtröder, 2008; 2013; Frey & Warda, 2008; Cosentino, 2013).

In fluorescence imaging (FI), an external light of appropriate wavelength is used to excite a target fluorescent molecule, followed almost immediately by release of lower-energy light for imaging. Targets for FI may be endogenous molecules such as hemoglobin (Hb), fluorescent proteins and related molecules, or optical contrast agents with fluorescent molecules. FI can be used for cellular and molecular imaging in small-animal models, indicating optical contrast that has the potential to extend from preclinical research to patient care (Graves et al., 2003). *In vivo* FI encompasses a wide range of resolution and imaging depths, including subcellular analysis at 400 mm with intravital microscopy and imaging with 1- to 3-mm spatial resolution at 10 cm with fluorescence molecular tomography (FMT) (Graves et al., 2003). In addition, fiber-optic endoscopes with confocal or 2-photon laser FI will facilitate clinical use of fluorescence molecular imaging with targeted optical contrast agents (Polglase et al., 2005).

To obtain fluorescence in deeper tissues, investigators have developed strategies for near-infrared fluorescence (NIRF) with emission wavelengths between 650 and 900 nm. At these wavelengths, absorption of light by Hb,

6

lipids, and water is low, and tissue autofluorescence also is enhanced. As a result, the sensitivity for NIRF imaging agents is improved, potentially allowing for optical imaging signals to be detected at depths of 7-14 cm (Weissleder & Ntziachristos, 2003). Differential absorption of light by tissues also produces images that are weighted toward optical reporters and probes that are located closer to the surface of a subject. While this limitation is being overcome with 3-dimensional imaging and analysis techniques such as the FMT, optical techniques typically allow relative quantification of imaging signals (Montet et al., 2005).

Magnetic resonance imaging (MRI) is an imaging technique that uses a magnetic field and pulses of radio wave energy to produce images of organs and structures inside a body. In many cases, the MRI provides different information about the structures in the body that can be seen with an X-ray, ultrasound, or computed tomography (CT) scanning. In XRI, radiations are usually generated in vacuum tubes by bombarding a metal target with high-speed electrons. Images are produced using a radiograph by passing the resulting radiation through a body onto a photographic plate or digital recorder, or by rotating both source and detector around the body to produce an images using the CT. MRI has been utilized to study signals between oxygenated and deoxygenated blood to indirectly quantify changes in blood flow associated with neuronal activity (Buxton, 2002). With advances in small-animal MRI, it is now possible to study the effects of pharmacological agents, such as alcohol and other drugs, in very small animals such as mice with sufficient resolution and without the confounding factor of drug-

7

anesthetic interactions (Chen et al., 1997; Benveniste & Blackband, 2002; Van der Linden et al., 2007).

Spectral imaging (SI) is an important imaging technology that combines optical spectroscopy with imaging. SI is the technique of acquiring images at more than one spectral band providing physical and chemical information out of the images. The SI technique is dependent of light source used during acquisition. A major advantage for SI probes and instrumentation, particularly those targeted towards eventual clinical applications, is overcoming attenuation and scattering of light by tissues. For light in the VIS region, optical signals from absorption molecules such as Hb are optimized by approximately 10-fold per centimetre of the tissue (Contag et al., 1995).

Spectral imaging has been used in many applications emphasizing methods used in quantifying biological processes. These applications include biometric pattern recognition (face, fingerprint and iris), the MRI, retinal physiology, non-image forming (NIF) responses of light and plant physiology among others (Teikari, 2008). SI extends the capabilities of biological and clinical studies to simultaneously study multiple features such as organelles and proteins qualitatively and quantitatively. SI can combine the strength of light microscopy imaging with that of spectroscopy to provide a new advantageous tool. Each of these fields is well developed and is being used intensively in many fields including the life sciences. The product of a SI system is a stack of images of the same object or scene, each at a different spectral narrow band. SI can capture light from frequencies beyond the VIS light range, such as IR. This can allow extraction of additional information that the human eye fails to capture with its receptors for red (R), green (G) and

8

blue (B) (RGB) colours. For accurate reproduction of the original colour through digital imaging systems, the SI technology is promising. By using the spectral information, the reproduced colour accuracy is considerably improved as compared to conventional RGB based systems.

Spectral imaging has been suggested as a method for non-destructive identification of pigments. The use of SI to tentatively identify pigments has an important advantage justifying its application: the rapid and low-cost survey of large areas (Frey & Warda, 2008; Teikari, 2008; Brydegaard et al., 2009; Cosentino, 2013). SI has been used for colour analysis, colour constancy, object recognition, digital staining and the analysis of works of art (Hu et al., 2005; Teikari, 2008; Bautista & Yagi, 2011). SI cannot only provide spatial and structural information about a sample, but it can also provide intracellular spectral data (Levenson & Hoyt, 2000; Hu et al., 2005; Park et al., 2007; Teikari, 2008).

The focus of SI techniques for imaging is driven in large part by its sensitivity for imaging optical contrast agents and reporting molecules *in vivo*. The lower limits of detection for SI may reach picomolar or even femtomolar concentrations. Combined with the minimal background of techniques such as bioluminescence imaging and fluorescence imaging in the NIR spectrum, the signal-to-noise ratio (SNR) for detecting specific molecular signals equals or exceeds that which can be achieved with other imaging modalities. There are enormous benefits of applying these optical imaging techniques to samples. Most importantly, light can provide exquisite sensitivity to functional changes via intrinsic changes in the optical properties of the sample. Absorbing and fluorescent dyes, as well as cutting-edge transgenic methods, can also provide

9

highly specific optical contrast enhancement. Additional advantages of the optical imaging techniques include the use of nonionizing radiation and inexpensive instruments. Besides, optical imaging techniques are able to measure a range of functional contrast, can readily be exploited via a wide range of approaches, from studies of intricate cellular mechanisms of normal and diseased tissues, to *in-vivo* noninvasive imaging.

Spectral imaging has been found useful for investigating tissue irregularities based on the interaction of the EM radiation with the tissue (Bremard et al., 1993; Ong et al., 2002; Wood et al., 2003; 2004; Svanberg, 2004; Somesfalean, 2004). SI is emerging as a powerful technique for diagnosing diseases (Luker & Luker, 2008; de Oliveira Silva et al., 2010; Kalnina et al., 2010; Al-Salhi et al., 2011; Masilamani et al., 2011). Imaging of brain tissues has also seen major improvement with the application of MRI (Ogawa et al., 1990; Belliveau et al., 1991; Kwong et al., 1992; Matthews et al., 2006). Optical imaging are continually being used in neurosurgical planning and the study of cognitive and perceptual responses and developmental changes (Matthew et al., 2006).

The SI technique has become more than just a step towards clinical diagnosis, but tools which can be utilized to aid in drug development for treatment. Applications of the SI technique has also included studies and investigations of acute and chronic stroke, Alzheimer, epilepsy, migraine, effects of cocaine and mechanisms of neurovascular coupling (Cannestra et al., 2001; Bolay et al., 2002; Pouratian et al., 2002; Devor et al., 2003; Ayata et al., 2004; Spires et al., 2005; Berwick et al., 2005; Bahar et al., 2006; Suh et al., 2006; Hillman et al., 2007). SI technique provides significantly more

10

flexibility, since preparations can be much more controlled and diseases and treatments can be systematically compared. Extrinsic dyes and cross-validation techniques such as electrophysiology can be utilized and developed without the need for clinical regulatory approval. Imaging microscopic samples also offer significant advantages, allowing higher resolution, improved sensitivity, high versatile and quantitation.

The optical techniques have also been used for the studies of *Plasmodium falciparum* (*P.falciparum*) infected red blood cells (RBCs), hereafter, referred to as *i*-RBCs. SI reveals hidden diseases and has brought feasibilities to *P.falciparum* diagnosis in most remote areas (Wongsrichanalai et al., 2007; Coffey, 2012). The human malaria parasite, *P.falciparum*, is responsible for over a million deaths every year mostly infants, pregnant women and young children in areas endemic for the parasites (Ross et al., 2006; Sio et al., 2006; Shekalaghe et al., 2009; WHO, 2011). In *P.falciparum* patients, a prompt and accurate diagnosis is the key to effective disease management (Sachs & Melaney, 2002; Amexo et al., 2004; Hay et al., 2004; Paton et al., 2011; Wongsrichanalai et al., 2011). According to a World Health Organization report 2013, a child dies of malaria every half a minute (WHO, 2013).

A number of diagnostic techniques have been proposed over the years for diagnosing *P.falciparum* infections. These techniques include fluorescent microscopy, rapid antigen detection, polymerase chain reaction (PCR), indirect immunofluorescence antibody assay (IFA) and enzyme-linked immunosorbent assays (ELISA) (Sulzer et al., 1969; Spencer et al., 1979; Bruce-Chwatt, 1984; Snounou, et al., 1993; Makler et al., 1998; Wilson et al.,

2011). Despite these advances, light microscopy is the accepted and efficient technique commonly used for *P.falciparum* diagnosis in most hospitals and clinics, especially in developing countries. This involves manual assessment of the parasites from thick or thin Giemsa-stained blood smear slides (Pammenter, 1988; Payne, 1988; WHO, 1991; Bloland, 2001; Ross et al., 2006; Sio et al., 2006; Tek et al., 2006).

Manual assessment of the parasites is, however, expensive, prolonged, grueling, requires an expert microscopist and can sometimes be biased (Payne, 1988; Oaks et al., 1991; Bloland, 2001; Coleman et al., 2002; Mitiku et al., 2003; Bates et al., 2004; Ross et al., 2006; Sio, et al., 2006; Tek et al., 2009; Paton et al., 2011; Savkare & Narote, 2011; Merdasa et al., 2013). Moreover, the accuracy of the final assessment eventually depends on the expertise and experience of the microscopist (Pammenter, 1988). It has been shown experimentally that the agreement rates among microscopists for assessing malaria parasites are surprisingly low (Wilson et al., 2011).

This lack of point-of-care diagnosis brought about the development of malaria antigen test, rapid diagnostic tests (RDTs), which has threshold for detecting more than 100 parasites per microliter of blood within a quarter of an hour (Moody, 2002; Wongsrichanalai et al, 2007). These immunochromatographic tests are commercially available in kits with all the necessary reagents. Besides, they are user-friendly, easier to perform and the associated procedure does not require extensive training or equipment to perform or to interpret the results (Peyron et al., 1994; Singh et al., 1997). RDTs test formats (e.g., in a plastic cassette enclosure, or attached to cardboard) promote ease-of-use and safety in comparison to the earlier assays

of the early and mid-1990s. RDT consumption, especially in developing countries, has increased for the past few years. Unskilled clinicians can be trained in RDTs techniques within a day (Premji, et al., 1994; Banchongaksorn, et al., 1997).

As an alternative to Giemsa stain manual microscopy and RDTs, numerous optical diagnostic techniques have been developed for assessing the *i*-RBCs based on parasites' byproduct (hemozoin) detection as a characteristic for *P.falciparum* infection and antimalarial activity. The hemozoin is formed from the food vacuole of *P.falciparum* parasites as they digest Hb for nutrient in their host RBCs. The hemozoin is crystallized by the parasites to sequester free heme from the Hb, which is toxic to the parasite (Egan et al. 2001; Ziegler et al., 2001; Loyevsky et al., 2001). Activity crystallization inhibitors resulting from biocrystallization of toxic-free heme released by the parasite in its food vacuole have been used for hemozoin detection in the *i*-RBCs (Kawamoto, 1991; Hänscheid et al., 2000; Lee et al., 2010; Cho et al., 2011; Hempelmann, 2007). Besides, dark-field (DF) microscopy has been used to observe the morphological features of the *i*-RBCs, in the blood based on hemozoin (Wolter, 1932; Jamjoom, 1983; Wood et al., 2009). Another hemozoin-based method is the use of cross or orthogonal polarization (xP) imaging applications to the *i*-RBCs research (Lawrence & Olson, 1986; Romagosa et al., 2004). A combination of DF and xP microscopy have also been used in flow cytometry systems for the *i*-RBCs diagnosis via hemozoin detection. A method known as depolarized side-scatter or depolarized laser light has been used with the flow cytometry for hemozoin detection in the *i*-RBCs (Mendelow et al., 1999; Josephine & Nissapatorn, 2005). Bioluminescence

13

signals, fluorescence microscopy, point-scanning laser confocal microscopy and photoacoustic microscopy imaging have all been used for the hemozoin detection (Rice et al., 2001; Graves et al., 2003; Levenson & Mansfield, 2006; Zhang et al., 2006; 2007; 2011). In addition, wide-field confocal polarization microscopy, laser desorption mass spectroscopy and third harmonic generation imaging have also been applied in the hemozoin detection (Scholl et al., 2004; Campbell et al., 2007; Bélisle et al., 2008). The parasite has also been detected using magneto-optical testing and photo migration in the field of tissue optics (Friebel et al., 2006; Mens et al., 2010). In spite of all these advances, no research work has focused on combining different optical techniques to study and characterize the *i*-RBCs on unstained blood smear slides prepared from blood samples of humans.

Purpose of Study

Overall Purpose

Generally, this work aims at applying three (3) optical techniques: LIF (both excitation spectral and imaging applications), spectrophotometry and SI, to study and characterize uninfected RBCs, henceforth, referred to as *u*-RBCs and the infected RBCs (*i*-RBCs) on staining-free blood smear slides. The blood smear slides will be prepared from uninfected blood (*u*-blood) samples and *P.falciparum* infected blood (*i*-blood) samples collected from volunteers. The work focuses on the study and characterization of the *u*-RBCs and the *i*-RBCs based on level of infections, that is, parasite densities (PDs) and intraerythrocytic life cycle stages (ring, trophozoite and schizont) of the *P.falciparum* parasite.

14

Specific Purposes

First and foremost, the aim of this work is to conduct feasibility studies on the *u*-blood samples and the *P.falciparum i*-blood samples from the volunteers employing LIF excitation spectral technique. This is to estimate PDs in the *P.falciparum i*-blood samples. Besides, the work aspires to, and with the aid of a spectrophometer, estimate PDs by determining and comparing optical densities (ODs) of the *u*-blood and the *i*-blood samples at different blood absorption spectral bands.

More so, the work aims at applying SI technique for the PD estimation. Geometrical as well as optical variables: aspect ratio (AR) and integrated optical density (IOD), with the aid of *Image Pro Plus 5.0* software, will be retrieved from spectral images containing the *u*-RBCs and the *i*-RBCs. These spectral images will be captured from a multispectral light-emitting diode imaging microscope (MSLEDIM). This MSLEDIM system captures spectral images in transmission, reflection and scattering modes.

Furthermore, the work seeks to find spectral bands that can be used as markers for identifying the *u*-RBCs and the *i*-RBCs in the three erythrocytic life cycle stages: ring, trophozoite and schizont. The spectral images acquired from the MSLEDIM will be used. Finally, a multi-functional imaging microscope (MFIM), capable for capturing transmission, reflection and fluorescence images will be assembled. This imaging system has the flexibility and adjustability for other optical imaging applications. Fluorescence images depicting the *u*-RBCs and the *i*-RBCs will be captured using the MFIM as a way of testing the assembled microscope for the *i*-RBCs detection.

Arrangement of Thesis

This thesis consists of five main chapters. Chapter one gives an introduction to optical techniques, malaria diagnosis and their associated challenges, an optical solution and the related concepts as well as applications to spectral image acquisition. The purpose of the work and the arrangement of the thesis are also included in this chapter. Chapter two reviews literature on spectroscopy and its concepts, light-tissue interaction principles, optical microscopy, optics of haemoglobin, spectral imaging, malaria diagnosis, as well as the principle underlying the experimental techniques used in this work.

Chapter three looks at the instrumentation for the MFIM, experimental methods and procedure for the research work. Results, analysis and discussions from laser-induced fluorescence excitation spectra, optical density determinations, spectral images acquired from the MSLEDIM and fluorescence images captured from the MFIM, are presented in Chapter four. In the fifth chapter, conclusions are drawn and relevant recommendations given to assist in further research.

CHAPTER TWO

LITERATURE REVIEW

Spectroscopy

Spectroscopy is termed as the study of the interaction between electromagnetic (EM) radiation and matter. In a wide sense, it can be said to be an experimental determination of the energy level structures and energy quanta absorbed or released in the transition between such energy levels of a physical system. For that purpose, transition processes, spontaneously or induced, between different energy states are studied.

The term spectroscopy was first used in the late 19th century and provided the empirical foundations for atomic and molecular physics (Schaepman et al., 2009). This concept comprises any interaction with radiative energy as a function of its wavelength or frequency. Spectroscopic data is often represented by a spectrum, a plot of the response of interest as a function of wavelength or frequency. Spectroscopy can be classified based on the region of the EM radiation being used in the study.

In spectroscopy, the quantity that is measured is intensity, either of energy transmitted or reflected. The collection of light intensities at different wavelengths gives a spectrum. To measure a spectrum, the light is dispersed into its different wavelength components and the intensity at each wavelength is measured (Stuart, 2004). There are different methods to disperse the light and almost all of them are used in various imaging systems. The main difference between spectroscopy and electronic imaging is that usually only

17

one single point of the region of interest is recorded in spectroscopy but analyzed in a large range of wavelengths. Peaks at particular wavelengths hint on specific chemical ingredients or compounds connected with dedicated material properties and their chemical or physical behaviour.

Generally, spectroscopy involves EM radiation with a set-up that comprises of three components: radiation source, analyzer and detector as shown in (Figure 1). The radiation source might be a regular light source, but may also be the sample under study. The sample may emit radiation of its own, but it may also send out emission in response to the radiation of it from an external source.

| Light source | $\longrightarrow$ | Analyzer | $\longrightarrow$ | Detector |
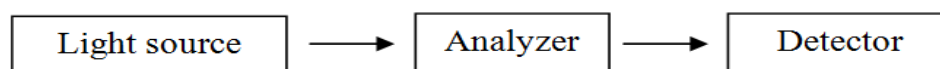
Figure 1: A modified set-up for spectroscopy (Svanberg, 2009).

The analyzer and the detector differ depending on the spectral range. The spectrum is the variation of the intensity of the radiation as a function of the frequency or wavelength.

In the electromagnetic spectrum, spectral range for human vision is investigated within the optical region extending from 400 nm (violet) to 750 nm (dark red). Low transition energies correspond to changes in molecular rotation which yield radio or microwave frequencies. High transition energies, due to electronic reorganization in inner atomic electronic shells yield sub-nanometre wavelengths, or tens of kilo electron volts for emissions. Transition energies ΔE corresponding to a transfer between two energy levels can be expressed as:

18

$$\Delta E = \frac{hc}{\lambda} \tag{1}$$

where h is Planck's constant, c is the speed of light and λ is wavelength of light source.

Light-Tissue Interaction

Interaction of light with tissue is the combined effect of the properties of the light source and the characteristics of the tissue. Fundamentally, interaction of light radiation with tissue depends in part on the wavelength of the light and the dimensions of the particles involved in the interaction. These particles can be of atomic size to complex molecule in the case of biological materials.

For biological materials, the tissue type and the state as well as the medium of the biological sample primarily influence the optical properties of the sample. Therefore, these optical properties are used to characterize light propagation through these materials. In general, when the light source is monochromatic in nature, for example a diode laser, the variables involved in the light-tissue interaction process is limited.

There are several factors that influence the light-tissue interaction. The power density provided by the source is considered one of the main factors. The amount of source power coupled into the medium under irradiation is a function of the light power output. At a constant power density, that is, the power per unit area, the radiant fluence rate in the sample at the core of the spot size increases with the spot size.

19

When light irradiation reaches the tissue surface at an angle, a progressively higher percentage of photons will be reflected off the surface at an increasing angle of oblique incidence. For example, collimated irradiation presents a greater challenge than diffuse irradiation in deriving an expression for the light distribution inside a turbid medium that is irradiated by a light beam.

Generally, when light impinges on a tissue, it can be reflected back towards the source, refracted or scattered, and results in a change in the angle of propagation, absorbed by the molecules in the sample, or transmitted. Besides, part of the absorbed light may be re-emitted as fluorescence light. Figure 2 shows some possible interactions between light and tissue. Depending on the specific material one or two of these processes dominate over the other.
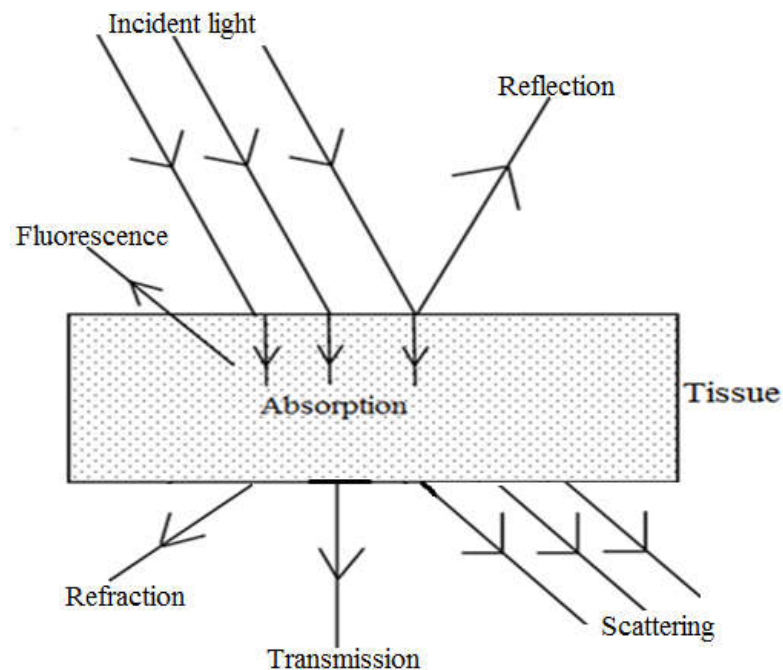
Figure 2: Some possible interactions between light and tissue; reflection, transmission, refraction, absorption, fluorescence and scattering.

20

Optical properties are different for distinctive biological tissues, and these differences are not always distinguishable by visual examination. The optical parameters are in fact a function of delivery protocol of the light source, tissue composition, and temperature and water content of the tissue. Different tissue and tissue constituents will interact with light according to their specific optical parameters, and require individual attention in the classification of their optical properties.

Reflection Spectroscopy

Reflection is the change in direction of a light at an interface between two different media so that the light returns into the medium from which it came from. Reflection of light is either specular (mirror-like) or diffuse (retaining energy, but losing image of original medium) depending on the nature of the boundary. Generally, a certain fraction of the light is reflected from the boundary and the remainder is refracted.

When a light wave travels in an incident medium with same speed, one part of the law of reflection is given as:

$$\theta_i = \theta_r \qquad (2)$$

where θ_i is the angle of incidence and θ_r is the angle of reflection. Thus, angle of incidence equals angle of reflection.

Transmission Spectroscopy

Transmission of light through a medium is a repetitive process of scattering and re-scattering. Each such event introduces a phase shift into the light field, which ultimately shows up as a shift in the apparent phase velocity

21

of the transmitted light from its nominal value of speed of light of the medium. The transmittance (T) of light, with incident intensity I_0 and transmitted intensity I is given as:

$$T = \frac{I}{I_o} \qquad (3)$$

i.e. the fractional intensity of the original light detected.

In general, variables involved in the light-matter interaction process are limited when the light source is monochromatic in nature. When light irradiation reaches the medium surface at an angle, a progressively higher percentage of light will be reflected off the surface at an increasing angle of oblique incidence.

Scattering Spectroscopy

Scattering of light radiation is the deflection of light rays in random directions by particles in a medium, or in the interface between two media with different refractive indices. Scattering from a surface or an interface can also be called diffuse reflection. Scattering may be due to surfaces which can be described as troughs and valleys that are slightly larger than the incident wavelength. Scattering often can occur when light travels in transparent solids and liquids, but is more prevalent in gases. Bubbles, impurities and inhomogeneities in a medium can also cause scattering (Katzir, 1993).

Light wave can be scattered by a sample if its wavelength does not match the energy-level transitions of atoms and molecules it incidence. Scattering process is defined as *elastic* if the wavelength of the scattered light is equal to the wavelength of the incident light or *inelastic* if the wavelengths

22

differ. Thus, for inelastic scattering, energy is transferred between the incident light and the particles in the medium. Rayleigh and Mie scattering are elastic, while Raman scattering is inelastic.

Elastic scattering of light occurs when charged particles in a medium are set into oscillatory motion by the electric field of the incident wave, and re-emit (as opposed to absorb) light of the same frequency as the primary wave. Scattering occurs at non-resonance frequencies. Hence, the scattered intensities are relatively weak since the forced vibrational amplitudes of the particles are much smaller than those at natural resonances. In most solids and liquids, however, intermolecular interactions broaden the absorption frequencies such that both scattering and absorption of light occur at all wavelengths.

As a result of scattering, the velocity of light in all tissue is less than it is in vacuum. In an optically dense or homogeneous medium, i.e. one in which the molecular separation is much smaller than the wavelength of the incident light, individual atoms or molecules in a medium will scatter the incident radiation in all directions. The phase difference of the scattered light relative to the primary wave will depend on the frequency of the primary wave. In any direction the total scattered field is then a superposition of all the scattered wavelets propagating in that direction.

The scattered waves will interfere with the incident wave, modifying its phase and hence the velocity of the light through the medium. The refractive index (RI) of a medium is given by

$$n = \frac{c}{v} \tag{4}$$

23

where c is the speed of light in vacuum and v the speed of light in the medium. The refractive index depends on the number of molecules per unit volume and their polarisability, since the total scattered wave that interferes with the incident wave depends on the amplitude and phase relations between the individual scattered wavelets.

Furthermore, the RI for a given medium changes with the frequency of the incident light. This phenomenon is known as dispersion and is due in part to the frequency-dependence of the relative phase change between the incident and scattered waves. Theory has shown, however, that to explain dispersion in real media over a broad spectrum, including the resonance frequencies, the absorption of light must also be considered. Thus, the complex RI is defined as:

$$N = n + ik \qquad (5)$$

where the real part, n, as defined in equation (4), determines the speed of the wave and the imaginary part, k, determines the absorption of the wave as it propagates through the medium. From Maxwell's equations, k can be related to the absorption coefficient μ_{abs} as follows:

$$k = \frac{\mu_{abs}\lambda}{4\pi} \qquad (6)$$

Various theories have been put forward to describe the scattering of light by particles of different shapes and sizes. In general, these fall into two categories: single scattering and multiple scattering theories. In single scattering theory, it is assumed that the particle separation is sufficiently large, or the number of particles sufficiently small, such that the total scattered wave due to all the particles is small compared to the incident wave (Bohren &

24

Huffman, 1983; van de Hulst, 1981). In other words, the assumption is that the particles do not further interact with the light that has been scattered from neighbouring particles.

Single scattering by particles small in diameter compared to the wavelength of the incident light is often known as Rayleigh scattering. When unpolarised light is incident on a small particle the intensity distribution of the scattered light is almost isotropic, since the secondary wavelets emitted by the oscillating charges are approximately in phase with one another. At an angle of 90° to the direction of propagation of the incident light, however, the charges oscillate linearly in one direction only, and thus the light appears to an observer to be linearly polarized.

According to Stark effect, an electric dipole moment P, induced in a polarized particle, is subject to an electric field of resultant amplitude (E), initial amplitude (E_o), frequency (v) and time (t) as shown in equation 7. Polarization will vary at the frequency.

$$E = E_o \sin(2\pi v t) \tag{7}$$

The total radiated intensity of Rayleigh scattered light, I is of the form

$$I = \frac{16\pi^4 c \alpha^2 E_o{}^2}{3\lambda^4} \tag{8}$$

where α is the polarizability tensor, c is the speed of light and λ is the wavelength of light source (Svanberg, 1992; Vo-Dinh, 2003). Equation 8 shows that the intensity of Rayleigh scattered light is inversely proportional to the fourth power of wavelength of light source.

The most important aspect of Rayleigh scattering is its wavelength-dependence, which varies with the inverse fourth power of the wavelength of

25

the illuminating light. Determining the scattered field patterns from particles that are large compared to the wavelength of the illuminating light is an enormously complex task, due to the significant phase differences between the scattered wavelets which must be taken into consideration. However, various approximations can be made to simplify the problem, as is the case in Rayleigh-Gans theory (Rayleigh, 1881). In this formulation, the large particle is theoretically split up into many small particles. It is then assumed that the scattered field from each particle of a smaller size is completely independent of the scattered fields from all the others that is described by Rayleigh scattering.

The scattered wavelets from individual particles will interfere with another and the theory must take account of the phase differences, relative to some common origin, between them. Provided the small particles are identical in terms of their size, shape and orientation, it can be shown that all wavelets propagating in the forward direction, i.e. the direction of propagation of the incident beam, are in phase with one another (Bohren & Huffman, 1983). Hence, the amplitudes of the scattered wavelets simply sum to give the total scattered field amplitude in the forward direction. In all other directions, constructive and destructive interference will occur.

If particles are much larger than the wavelength of the incident light, the process is called Mie scattering. This form of scattering describes spherical particles. Mie scattering is not strongly wavelength dependent. The intensity of Mie scattered light varies from λ^{-4} in the Rayleigh limit to about λ^{-2} for large particles. Mie theory exactly describes both absorption and scattering by a spherical particle of arbitrary radius and RI (Mie, 1908). The analysis

26

involves the formal solution of Maxwell's electromagnetic theory for homogeneous spheres using the appropriate boundary conditions (Bohren & Huffman, 1983; van de Hulst, 1981), which in the limit of a small particle reduces to the relatively simple solution for a Rayleigh scatterer. As with the Rayleigh-Gans theory, the scattering is most intense in the forward-direction. However, unlike the Rayleigh-Gans scatterer, the amplitudes of the scattered wavelets in any direction will never be exactly the same, due to the inclusion of absorption effects, therefore complete destructive interference cannot occur.

In the case of single scattering therefore, a new exponential relationship can be defined for the collimated-beam intensity I, relative to the incident intensity I_o, transmitted a length l through an absorbing medium in which only single scattering occurs as

$$I = I_o e^{\mu_t l} \qquad (9)$$

where μ_t is the total attenuation coefficient, given by

$$\mu_t = \mu_{abs} + \mu_s \qquad (10)$$

μ_{abs} is absorption coefficient and μ_s is scattering coefficient, the probability that a photon will be scattered per unit length. The reciprocal of the total attenuation coefficient, μ_t^{-1} is known as the mean free path, and is the distance travelled by a photon between interactions. In reality, there are many systems for which the assumption that the particles are independent of one another is invalid and multiple scattering becomes important (Ishimaru, 1978).

Biological tissue illuminated by near infra-red (NIR) light is just one example in which multiple scattering cannot be ignored. On encountering a scattering particle within a homogeneous medium, photons travelling in a

27

direction s_1 are scattered into a new direction s_2. The new direction generally does not occur with equal probability and can be described by the differential scattering coefficient $d\mu_s(s_1, s_2)$. Integrating over all angles gives μ_s, the total scattering coefficient

$$\mu_s = \int_{4\pi} d\mu_s(s_1, s_2)ds \qquad (11)$$

Here, it is assumed that the scattering coefficient is independent of the original direction s_1 of the photons, and that it depends only on the scattering angle between the incident and scattered photons. This may hold true for randomly structured media, but many media have orientation-dependent structure and the scattered intensity distribution will therefore depend on the incident direction. The scattering phase function p is the normalized version of the differential scattering coefficient

$$p(s_1, s_2) = \frac{1}{\mu_s} d\mu_s \qquad (12)$$

such that $\int_{4\pi} p(s_1, s_2)ds_2 = 1$. The mean cosine g of the scattering angle θ, the angle between the incident s_1 and scattered s_2 directions, is known as the anisotropy factor

$$g = \int_{4\pi} p(\theta)\cos(\theta)ds_2 \qquad (13)$$

If the scattering is completely isotropic then p is equal for all angles and g will be equal to zero. As the particle size increases, however, the intensity distribution increases in the forward direction and p for small angles is much higher than for all other angles. Therefore, the mean cosine tends towards a value of unity, the higher the g value the more forward-peaked the

28

scattering. Combining the scattering coefficient and the anisotropy factor gives

the transport scattering coefficient.

$$\mu_{s_2} = (1-g)\mu_{s_1} \tag{14}$$

From the definition of μ_{s_2} follows the expression for the transport attenuation

coefficient

$$\mu_{t_2} = \mu_{abs} + \mu_{s_2} \tag{15}$$

and its reciprocal, $\mu_{t_2}^{-1}$, the transport mean free path. Another useful

definition is the scattering cross-section σ_s, which describes the ability of a

particle to scatter light. It is expressed as the effective surface area that a

perfectly absorbing disk would have in order to produce the same attenuation

of a collimated beam, measured by a collimated detector, as the scattering

particle. The scattering coefficient and the scattering cross-section are related

as follows

$$\mu_s = \rho\sigma_s \tag{16}$$

where ρ is the particle number density in the medium.

Scattering of light in tissue is caused by inhomogeneities such as cell

membranes or intracellular structures. The scattering arises due to a relative RI

mismatch at the boundaries between two such media or structures, e.g.

between the extracellular fluid and the cell membrane. Cells vary greatly in

size, from blood platelets of approximately 4 μm to nerve cells as much as a

metre in length. However, all cells consist of three main components: the cell

membrane, the cytoplasm and the nucleus. The cell membrane, which

constitutes the outer boundary of the cell, is made up of a phospholipid

bilayer, approximately 8 nm in thickness, with numerous proteins embedded

in it. The cytoplasm is the intracellular 'matrix' held within the bounds of the cell membrane. It consists of the cytosol, a water-based fluid within which the other constituents are suspended, the organelles, each of which have a special function in the cell mechanism, and non-functioning units known as inclusions, which include lipid droplets in fat cells and melanin granules in certain skin cells.

Cells receive their energy supply from organelles called mitochondria, the number of which reflects a cell's need for energy. The mitochondria, approximately 1-4 μm by 0.3-0.5 μm in size (Jamieson & Palade, 1967), are surrounded by a double layer of membrane similar to the outer cell membrane. The nucleus is the largest organelle in the cell and constitutes its control centre. The size of the nucleus varies with cell type, with an average diameter in the order of 5 μm (Marieb, 1995). The nucleus, like the mitochondria, is surrounded by a double-layered phospholipid membrane.

In order to understand how light is scattered in tissue it is helpful to study the structures responsible for scattering on a microscopic, i.e. cellular or sub-cellular, level. Each microscopic scattering particle or object will give rise to its own scattering phase function, which depends on the physical properties of the object. A single scattering event in tissue can be considered to arise from an 'averaged scattering object, representing a distribution of scattering objects with an averaged phase function. The contribution of each type of object to the averaged scattering properties in tissue will depend on their individual scattering properties and their relative concentrations.

Mourant et al., (1998) studied suspensions of mammalian cells in order to determine the dominant scattering centres in tissue. Comparing their

30

measurements of the transport scattering coefficient μ_{s_2} and the anisotropy factor g with predictions from Mie theory, they determined that the observed scattering was due to particles with a distribution of sizes, equivalent to spheres with diameters ranging from about 0.2 to at least 1 μm. They also measured the phase functions of isolated cell nuclei and mitochondria and compared them to the phase function measured for the cells. The authors concluded that the majority of light scattering from a cell at small angles is due to the nucleus, the smaller organelles such as the mitochondria being responsible for scattering at larger angles.

In a more recent study, Mourant et al. (2002) determined that approximately 55% of scattering from cells at angles greater than 40 was due to the internal cellular structures. By comparing scattering from cells and nuclei at different growth phases, they concluded that the nucleus and its sub-structures are responsible for a maximum of approximately 40% of the scattering at any angle and that, as confirmed by the known change in mitochondrial content with growth phase, other organelles in the cytoplasm must also contribute significantly to the observed high-angle scatter.

Beauvoit et al., (1995) and Carter, 1996 demonstrated a linear increase in μ_{s_1} with mitochondrial protein content for various adult rat tissues. The mitochondrial volume fraction was estimated to vary widely in the cells under investigation, from around 8% in brain to as much as 28% in liver cells. In one tissue type, white adipose tissue (WAT), μ_{s_1} was very high and did not exhibit the same linear dependence on mitochondrial protein content as the other tissue types. The authors commented that the high volume fraction of lipid particles in WAT (approximately 88%) and the relatively high refractive index

31

of lipid particles (approximately 1.49 for pure triglyceride (Ross, 1967) could be responsible for the observed anomaly.

In a similar study of scattering from adult rat liver, Beauvoit & Chance (1998) estimated that the mitochondria were responsible for approximately 73% of total scattering observed from hepatocyte suspensions (Carter, 1996). Based on the mitochondrial content in whole liver, they determined that μ_{s_1} due to the mitochondria was very close to their measured value of μ_{s_1}. They therefore suggested that, on the premise that the isolated mitochondria are optically comparable to those *in situ* in the liver, the mitochondrial compartment must be the dominant scatterer in liver tissue.

Another approach to examining the relationship between light scattering and cellular structure is to study the spatial variation in the refractive index on a microscopic level. Beuthan et al., (1996) have studied the refractive index of biological cells using a technique called phase microscopy (Beuthan et al., 1996). The phase shift $\Delta\varphi$ of an incident wave (relative to its wavelength) on passing through a sample is related to the difference in RI Δn between the sample and the surrounding medium

$$\Delta\varphi = \frac{2\pi d \Delta n}{\lambda} \qquad (17)$$

where λ is the wavelength of the light and d is the diameter of the sample.

Beuthan et al., (1996) produced phase images of living and dried cells and mitochondria. They showed that the phase shift produced by the mitochondria was small compared to the mean shift due to the whole cell. On inspection of the cross-sectional phase images, they noted that only the nucleus and the cell membrane appeared visibly different from the bulk of the

32

cell. The cell and the mitochondria were modelled using Rayleigh-Gans theory, for which the differential scattering cross-section and phase function can be determined using the relative RI of the particle. They noted that the contribution of a particular particle to the total scattering coefficient observed in bulk tissue could then be calculated from the product of the cross-section and number density of the particle (Beuthan et al., 1996).

In the same study, Beuthan et al. (1996), point out that the high RI of lipids in the phospholipid membranes (approximately 1.48) relative to the RI of the cytoplasm (approximately 1.38) is likely to be a significant cause of scattering from the cell. Modelling the cell as a coated sphere, however, with a coating thickness of 10 nm and a relative RI of 0.1, they determined that the scattering cross-section of the outer cell membrane alone is sufficient to describe only 1% of the typical scattering coefficient in tissue (Beuthan et al., 1996). Moreover, a simple model of the mitochondria, which contain between 20 and 40% of the total membrane volume of the cell (Alberts et al., 1983), as spheres of mean RI equal to 1.4 implies that a number density of greater than 1000 mitochondria per cell is required to explain the total scattering coefficient. This has in fact been seen to be the case in hepatic cells, where the number density of mitochondria is estimated to be around 1740 (Carter, 1996).

Rayleigh scattering and Mie scattering are the two most dominant scattering types in blood cells. They result from microscopic and macroscopic constituents such as cellular membranes, RI mismatch between intra- and extra-cellular fluids mitochondria, ribosomes and fat globules. The scattering of light by RBCs is distinct since the RBCs have no nucleus or other intracellular organelles, making them extremely efficient carriers of oxygen.

33

In the work of Ross (1967), the RI of the RBC was revealed to be 1.4 ± 0.01 and that of blood plasma to be 1.34 (Ross, 1967). Scattering by a single RBC is not easily modeled, however, since it is too large to employ Rayleigh-Gans theory and presents difficulties to Mie theory because of its irregular shape. In spite of this, various authors have made use of these theories (Steinke & Shepherd, 1986) have compared their results to experimental data.

Using Mie theory for an uncoated, spherical particle and typical values for the RIs, Steinke and Shepherd (1988) modelled scattering from the RBCs in saline suspensions (Steinke & Shepherd 1988). They found a reasonable agreement between experimental and theoretical values for the scattering cross-section σ_s, but a rather poor correlation between results for the g values, Mie theory predicting a higher anisotropy factor g, i.e. more forward-peaked scattering, than that found experimentally. As they decreased the concentration of the saline solution, the agreement between theoretical and experimental values of g improved.

Optical microscopic images of blood cells provide a wavelength that is specifically linked to the physical properties of the cells and it is dependent of light source used during acquisition. It thus gives an objective measurement which has high reproducibility and makes it possible to analyze cells using wavelengths outside the visible spectrum, in particular ultraviolet (UV) or near-infrared (NIR) (Hu et al., 2005; Bautista & Yagi, 2011).

34

Absorption Spectroscopy

Absorption spectroscopy is the analytical technique based on measuring the amount of light absorbed by a sample at a given wavelength. Absorption spectroscopy, particularly in the UV and visible (VIS) portions of the EM spectrum, is one of the most versatile and widely used techniques. This is concerned with the measured absorption of radiation in its passage through a gas, a liquid or a solid. The wavelength region generally used is from 190 nm to about 1000 nm, and the absorbing medium is at room temperature (Andor technology, 2006). Absorption of a photon results in a change of the electronic energy accompanied by changes in the vibrational and rotational energies. Each vibronic transition, i.e. a particular electronic plus vibrational transition, corresponds to an absorption band consisting of rotational lines. In liquids and solids, the rotational lines are broad and overlap so that no rotational structure is distinguishable.

Absorption of light is the way by which energy of a photon is taken up by matter, typically by the electrons of an atom (Anderson & Parrish, 1981; Bersha, 2010). The absorbed light energy is transformed to other forms of energy such as heat in the medium. The spectral distribution of light due to the absorption process depends on the distribution, concentration and absorption spectra of the absorptive elements. Atoms and molecules of matter absorb energy at certain frequencies or wavelengths. If the photon energy, its frequency and wavelength, is suitable to the atom or molecule, it may absorb the energy and get excited. Every atom or molecule has a unique set of absorption line and this makes identification of a sample possible through absorption analysis (Svanberg, 1992; Somesfalean, 2004).

35

Absorption spectroscopy deals with photon absorption by electrons distributed within specific orbitals in a population of molecules. Upon absorption, one electron reaches an upper vacant orbital of higher energy. Thus, light absorption would induce the molecule excitation. Transition from ground to excited state is accompanied by a redistribution of an electronic cloud within the molecular orbitals. This condition is implicit for transitions to occur. According to the Franck-Condon principle, electronic transitions are so fast that they occur without any change in nuclei position, that is, nuclei have no time to move during electronic transition. For this reason, electronic transitions are always drawn as vertical lines.

An absorption spectrum is the result of electronic, vibrational, and rotational transitions. The spectrum maximum (the peak) corresponds to the electronic transition line, and the rest of the spectrum is formed by a series of lines that correspond to rotational and vibrational transitions. Therefore, absorption spectra are sensitive to temperature. Raising the temperature increases the rotational and vibrational states of the molecules and induces the broadening of the recorded spectrum.

The profile of the absorption spectrum depends extensively on the relative position, which depends on the different vibrational states. The intensity of the absorption spectrum depends, among others, on the population of molecules reaching the excited state. More population of molecules at the the excited state correspond to high intensity of the absorption spectrum. Therefore, recording absorption spectrum of the same molecule at different temperatures should yield, in principle, an altered or modified absorption

36

spectrum. A spectrum is characterized by its peak position (the maximum), and the full width at half maximum, which is equal to the difference

$$\delta v = v_2 - v_1 \qquad (18)$$

where v_1 and v_2 correspond to the frequencies that are equal to half the maximal intensity.

Absorption of light by a medium is directly correlated to the incident radiation and the absorption coefficient of the medium. A medium with a high coefficient of absorption will absorb a large amount of light if the wavelength of the incident light corresponds to the absorption band of the medium. Conversely, light can propagate a long distance without or with very little absorption in a medium with a low absorption coefficient.

When light radiation is incident on tissue composed of discrete electrical charges, the charges are forced to oscillate at the frequency of the incident electric field. The range of frequencies covered by radiation in the electromagnetic spectrum is comparable to the natural frequencies at which atoms or molecules will vibrate in the absence of an applied field. Thus, when the radiation is incident on a system of tissue, resonance will occur around the natural frequencies, whereby energy is transferred from the incident field to the system and its amplitude of vibration is greatly increased.

Although the lifetime of the excited state is around 10^{-7} to 10^{-8} seconds, the atoms or molecules will usually lose their energy by colliding with one another within 10^{-12} seconds, thereby raising the kinetic energy of the other particles involved in the collisions. Hence, the energy associated with the incident field is most often dissipated as heat within the medium. This process is known as absorption. The overall effect of absorption is a reduction

37

in the intensity of the light beam traversing the medium (Bohren & Huffman, 1983).

A relationship between the absorption of light in a purely absorbing medium and the thickness of the medium was first determined by Bouguer (Bouguer, 1729). Some years later Lambert (Lambert, 1760) derived the following mathematical expression for the relationship, known as the Lambert-Bouguer law:

$$\frac{dI}{I} = -\mu_{abs}dl \tag{19}$$

which describes how each successive layer dl of the medium absorbs the same fraction dI/I of the incident intensity I for a constant μ_{abs}, the latter known as the absorption coefficient with units of inverse length (usually mm^{-1}). For an incident intensity I_o, therefore, the transmitted intensity I through a distance l will be

$$I = I_o e^{-\mu_{abs}l} \tag{20}$$

The absorption coefficient μ_{abs} can thus be interpreted as the probability that a photon will be absorbed by the medium per unit length. The reciprocal of the absorption coefficient, known as the absorption length, is the distance required for the intensity of the beam to fall to e^{-1} of the initial intensity. The absorbance of the medium is defined as the $\log_{10}$ inverse of the transmittance (equation 3)

$$A = \log_{10}\left(\frac{1}{T}\right) = \log_{10}\left(\frac{I_o}{I}\right) = \beta l \tag{21}$$

38

where the unit of absorbance is the optical density (OD). Hence, the units of β are OD per unit length (usually ODcm^{-1}). Expressing equation (21) in base 10 logarithms gives

$$I_o = I10^{\beta l} \text{ and } I = I_o 10^{-\beta l} \tag{22}$$

where the constant β is known as the extinction coefficient. The extinction coefficient and the absorption coefficient are conceptually the same, differing only by the base of the logarithm used in the Lambert-Bouguer expression. For the same unit length, therefore, the extinction coefficient is related quantitatively to the absorption coefficient by a factor of 0.434. In 1852, Beer determined that the absorption coefficient of a compound is linearly related to its concentration c diluted in a non-absorbing medium (Beer, 1852)

$$\mu_{abs} = \alpha c \tag{23}$$

where α is known as the specific absorption coefficient. In a solution containing a mixture of n absorbing compounds, the total absorbance is the sum of the individual extinction coefficients multiplied by the distance l

$$A = (\beta_1 + \beta_2 + ... + \beta_n)l = (\varepsilon_1 c_1 + \varepsilon_2 c_2 + ... + \varepsilon_n c_n)l \tag{24}$$

The Beer-Lambert law is only valid under certain limited conditions: the light entering the medium must be monochromatic and perfectly collimated, and the medium itself must be purely and uniformly absorbing. Therefore, certain errors will arise when applying the law to practical spectroscopic measurements since, for example, even lasers are not perfectly monochromatic. The consequences on experimental measurements of the limitations imposed by the Beer-Lambert law has been discussed elsewhere (Cope, 1991).

There are many compounds in biological tissue which absorb light radiation, collectively known as tissue chromophores, each of which has its own unique spectrum. As expressed in equation (24), the total extinction coefficient of a mixture of compounds is equal to the sum of their individual extinction coefficients, weighted by their relative concentrations. Therefore, approximating tissue as a homogeneous mixture of compounds, the overall light absorption in tissue at a given wavelength depends on the type and concentration of chromophores present.

Mathematically, if the energy of the incident flux is normalized to 1, then the absorbance (A), reflectance (R), scattering (S) and transmittance (T) sum to unity as expressed in equation 25 (Palmer & Grant, 2009):

$$A + R + S + T = 1 \qquad (25)$$

In general, a measure of A, R, S and T of the incident light depend on the wavelength of the incident radiation. Thus, these four processes can either be quantified for a monochromatic radiation or for a polychromatic radiation. In addition, the A, R, S and T of the incident light might also depend on polarization and geometric distribution of the incident radiation, which has to be specified.

Fluorescence Spectroscopy

Fluorescence occurs when a molecule absorbs light photons from the ultra violet (UV)-visible (VIS) light spectrum, known as excitation, and then rapidly emits light photons as it returns to its ground state. It characterizes the relationship between absorbed and emitted photons at specified wavelengths. It is a precise quantitative analytical technique that is inexpensive and easily

measured. Intensity of emitted light depends on a number of factors, including intensity of incident exciting light (the more powerful the exciting light, the stronger the emitted fluorescence intensity). In fluorescence measurement, fluorescent molecules are attached to the objects, or the object itself is the source of light (Richard et al., 2002). In many cases there is a direct functional relationship between the concentration of fluorescent molecules and the amount of fluorescence intensity.

All chemical compounds absorb energy which causes excitation of electrons bound in the molecule, such as increased vibrational energy or, under appropriate conditions, transitions between discrete electronic energy states. For a transition to occur, the absorbed energy must be equivalent to the difference between the initial electronic state and a high-energy state. This value is constant and characteristic of the molecular structure. This is termed the excitation wavelength. If conditions permit, an excited molecule will return to ground state by emission of energy through heat and/or emission of energy quanta such as photons. The emission energy or wavelengths of these quanta are also equivalent to the difference between two discrete energy states and are characteristic of the molecular structure. Figure 3 shows a simplified diagram of absorption and fluorescence emissions produced by molecules.

41
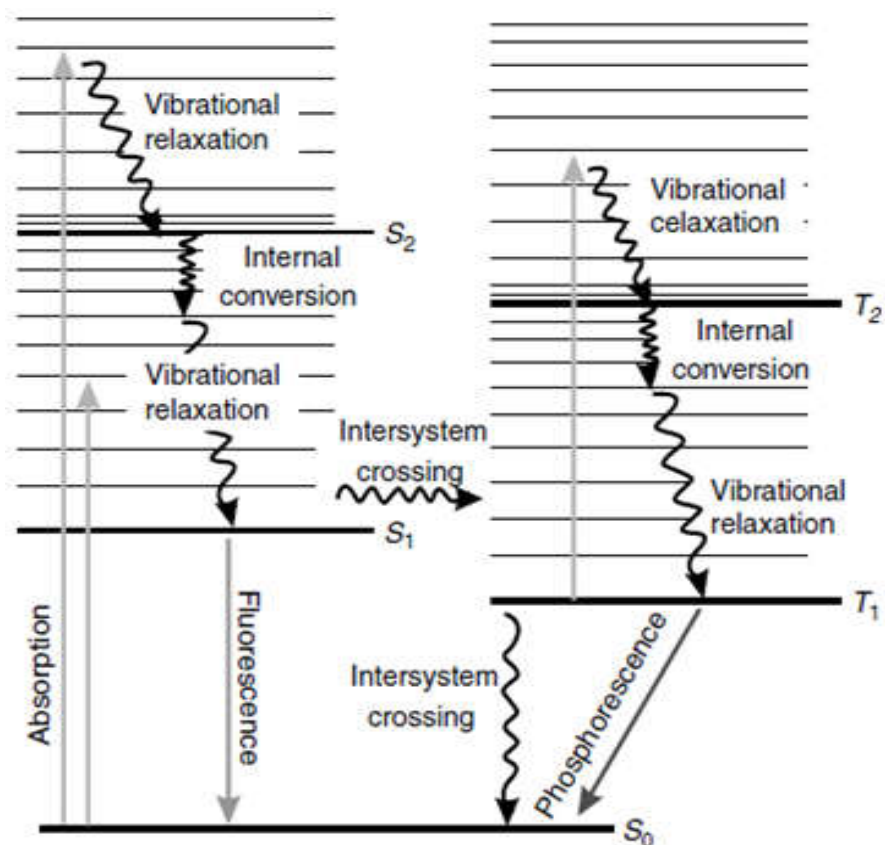
Figure 3: Jablonski diagram describing the electronic levels of common
organic molecules and possible transitions between different singlet
and triplet states (Jablonski, 1935).

At room temperature, most molecules occupy the lowest vibrational
level of the ground electronic state, and on absorption of light they are
elevated to produce excited states. Absorption of light (photons) by a
population of molecules induces electrons passage from the singlet ground
electronic level S_0 to an excited state S_n.

An excited molecule will return to the ground state S_0 following two
successive steps: the molecule at S_n returns to the lowest excited state S_1 by
dissipating a part of its energy in the surrounding environment. This
phenomenon is usually called internal conversion. From the excited state S_1,
the molecule will reach the ground state S_0 via different competitive processes.

42

Emission of a photon (fluorescence) and heat with a radiative rate constant in which part of the absorbed energy is dissipated in the medium. This type of energy is nonradiative and occurs with a rate constant. The excited molecules can release some of their energy to molecules located nearby. This energy transfer occurs with a rate constant (collisional quenching), or with a rate constant (energy transfer at distance).

A transient passage occurs to the excited triplet state T_1 of energy lower than S_1 with a rate constant (inter-system crossing). For each excited state, there is an excited state of lower energy. The triplet state is an excited state and so is energetically unstable. Therefore, de-excitation of the molecule from the triplet state occurs via competitive processes similar to those described for the de-excitation of the excited singlet state S_1: emission of a photon with a rate constant. This phenomenon is called phosphorescence. Dissipation of nonradiative energy with a rate constant and transfer of energy to another molecule at distance or by collision.

A chromophore that emits a photon is called a fluorophore. Many chromophores do not necessarily fluoresce. In this case, energy absorbed is dissipated within the environment as thermal energy, collisional energy as the result of permanent collisions with the solvent molecules, and also energy transfer to other molecules. The absence of fluorescence is the result of total energy transfer from the porphyrin ring to iron. The Jablonski diagram shown in figure 3 is also called the electronic transitions diagram, since electrons of chromophores and/or fluorophores are responsible for the different described transitions.

43

Absorption allows a chromophore to reach an excited state, and so photon absorption induces excitation. The absorbed energy is higher than the emission energy. In fact, the total energy absorbed by the molecule is released in the medium in different ways, such as photon emission. Thus, the energy of the emitted photons is lower than the energy of the absorbed photons.

Many phenomena other than fluorescence emission contribute to fluorophore de-excitation. These other alternatives to fluorescence are radiationless loss, phosphorescence, photo-oxidation, and energy transfer. Thus, the weaker the competitive phenomena, the higher the de-excitation via fluorescence. Emission occurs from the excited state S_1, independently of the excitation wavelength. Therefore, the emission energy would be independent of the excitation wavelength. The fluorescence energy is higher than that of phosphorescence.

Absorption and fluorescence do not require any spin reorientation. However, intersystem crossing and phosphorescence require a spin reorientation. Therefore, absorption and fluorescence are much faster than phosphorescence. Absorption occurs within a time equal to 10^{-15} s, and the fluorescence lifetime goes from 10^{-9} s to 10^{-12} s. Phosphorescence is a long transition that can last from milliseconds to seconds, minutes, or even hours.

Energy of electronic transition is equal to the energy difference between the starting energy level and the final level as described in equation 1. Each transition occurs with a specific energy and so at a specific and single wavelength. However, spectra are observed as a result of the contribution of rotational and vibrational levels to absorption and de-excitation energy. The

44

fluorescence spectrum generated shows a maximum corresponding to the emission transition.

The absorption spectrum occurs from the ground state. Therefore, it will characterize the electronic distribution in this state. Fluorescence and phosphorescence occur from excited states, and so they are the mirrors of electronic distribution within the excited states. Any modification of the electronic distribution in these states, such as in the presence of a charge transfer, will modify the corresponding spectrum. One such example is the reduction of cytochromes. The addition of an electron to the ground state, for example, modifies the electronic distribution within the molecule affecting the absorption spectrum.

Emission (E) occurs from a population of n excited fluorophores with intensity I:

$$I = nE \qquad\qquad (26)$$

The emission lifetime is within the picosecond-to-nanosecond range. Thus, emission is a very fast process, and so in order to observe fluorescence emission, the fluorophore should be excited continuously.

Temperature variation induces modification of global and local motions of the fluorophore environment and of the fluorophore itself, modifying its fluorescence emission feature. The intensity, position of the emission wavelength, and lifetime are some of the observables that will characterize a fluorophore. Each fluorophore has its own fluorescence properties and observables. These properties are intrinsic to the fluorophore and are modified with the environment. A fluorescence spectrum is the plot of the fluorescence intensity as a function of wavelength.

The energy absorbed by a fluorophore is more important than the energy of an emitted photon. Referring to equation (1), the absorbed energy is

$$E_{abs} = \frac{hc}{\lambda_{abs}} \qquad (27)$$

and emission energy is

$$E_{em} = \frac{hc}{\lambda_{em}} \qquad (28)$$

Since $E_{em} < E_{abs}$, then

$$\lambda_{em} > \lambda_{abs} \qquad (29)$$

where λ_{abs} and λ_{em} are absorption and emission spectra peaks respectively. Thus, the emission spectrum has its maximum shifted to longer wavelengths compared to the maximum of absorption spectrum (Albani, 2007). This is referred to as the Stokes shift. When absorption and/or the emission spectra of a fluorophore possess two or more bands, the Stokes shift is equal to the difference that separates the two most intense bands of the two spectra.

Laser-induced fluorescence of plants and trace-gas assessments has gained considerable interest in several biological, environmental and medical processes and applications. This is because many conventional analytical methods work by separation of species, which is time consuming and expensive. Therefore molecular detection or excitation by laser-based technique has become, particularly, a favourable approach. Combination of laser-based methods with techniques which do not require large quantities of molecular species, but even very few molecules, has opened up many fascinating possibilities to study physical processes of and on such molecules.

In the past few years, a variety of laboratory and field instruments based on fluorescence spectroscopy have been introduced. Some instruments

46

use a nitrogen laser (337 nm excitation wavelength) as the excitation source, while others use the 3rd or 4th harmonic of the Nd:YAG laser with excitation wavelength of 266 nm or 133 nm, respectively (Svanberg, 2004). However, these instruments are not as compact as when diode lasers are used (Gustafsson et al., 2000; Anderson et al., 2004). The other advantage of the diode laser is that it can be operated with 9 V battery.

In recent times, diode laser as a source has been widely applied on biological materials for assessments and diagnostics. This is because diode lasers enable sensitive detection of photophysical parameters, which are very difficult to assess with conventional techniques using lamps. These diode laser based methods measure the optical parameters of the biological materials in their natural environment reducing or even avoiding the influence of the measurements on the measured parameter.

Several optical-based analytical methods have been developed using diode lasers. The high intensity and spectral quality of diode laser light enable highly sensitive detection of various substances. Some of these methods which were not feasible with low-intensity light sources have become readily applicable.

Great advances that have been made in the development of diode lasers in the operative spectral regions ranges from the UV through the VIS to the NIR at room temperatures and have shown promising applications. One of these is the use of diode lasers as light sources for spectroscopic applications. The small size and high operationability of diode lasers are paving way for a new generation of compact, portable and relatively inexpensive sensors. These sources have been used for chemical species detection, gas sensing and

47

temperature. Other areas of application include velocity, pressure, mass flux, combustion, atmospheric sciences and medicine.

Diode laser-based spectroscopy applies the concept of light interaction with matter on the principle that every atom and molecule may absorb and or scatter or emit light. Such phenomena tend to associate specific characteristic spectral features of the material under study to enable the atom or molecule in the material to be identified. Important information on the properties of the atoms or molecules in that medium, thus the material, can be gained for diagnosis, characterization, discrimination and classification of the material for subsequent applications in diverse fields.

There are basically three main types of diode laser-based spectroscopic techniques used for various purposes and they are outstanding for a variety of applications. These are absorption, scattering and emission (fluorescence) techniques. They divide themselves conveniently into groups with respect to the process of interaction. Depending on the type of application, and in turn the type of species to be detected, the different techniques have different applicability. These techniques have been used to obtain information about solids, liquids and gases in various applications in biological, medical and environmental fields (Svanberg, 2004). However, much is left to be done on biological materials using the above techniques.

The reason for the success of the diode laser-based spectroscopic techniques is that laser light has a number of spectacular properties that make it useful for detection of atoms and molecules in solid, liquid and especially gas phase. The most important attribute of diode lasers for spectroscopic applications is that it often has a narrow frequency width. Of special

importance is their ability to detect the presence of small or unknown concentrations of species in gas phase under various types of conditions. There are a number of diode laser-based techniques that have been developed during the past two to three decades and the general denominator is their high sensitivity and selectivity.

The narrow frequency width is the basis for the high species selectivity that laser techniques possess. Another is that it has a high directionality with the aid of a lens system. This implies, among other things, that it can be sent over long distances, as is done in techniques for probing the atmosphere, or focused down to micrometer-sized spots. Additionally, there are safety advantages in non-invasive sampling and the use of fibre optics light transmission so that the monitoring and control of equipment can be kept at a safe location. In order to be able to run a given instrumentation under optimum or at least suitable conditions, one has to have a good understanding of the underlying mechanisms of the techniques. This is indeed a matter of crucial importance for the applicability and reliability of the techniques.

The wavelength of all individual diode lasers can be slightly tuned by temperature and current control. The tuning range depends on the laser materials and structure. Due to the linewidth and limited tunability additional optical techniques are normally required for their application as spectroscopic light sources. Several techniques have been developed in order to operate the diode laser in a single mode with narrow linewidth and to extend the tuning range.

For spectroscopic purposes, especially absorption spectroscopy, in the NIR the detection sensitivity decreases because weaker vibrational transitions

49

are detected. However, this is outweighed in many cases by the tremendous practical advantages of easy to use, robust, reliable devices operating at room temperature with relatively high output emission power and at a single discrete wavelength. In addition, inexpensive spectrometer components can be used. The very narrow wavelength spread of the light emission can ensure that interferences from other transitions are negligible. The ability to directly vary the output emission, that is, by modulation in order to improve detection sensitivities, also remains as a technical advantage.

Due to its low demand on systems and samples, fluorescence spectroscopy has been one of the most used optical methods for analysis. After the absorption of photons, the excited molecule emits a characteristic fluorescence spectrum. Like a fingerprint, it allows a differentiated statement about the fluorescing molecule.

Fluorescence has numerous measurement aspects, including intensity and excitation wavelength dependence, and quantities such as fluorescence decay time, anisotropy, polarization conditions, quantum yields and Stokes' shifts, which can be accessible for analysis. These parameters for the detection of substances allow alleviating some difficulties which may occur when applying fluorescence spectroscopy, for example, matrix and quenching effects. There are also cases where one parameter may give little or no information at all; in this case, other parameters may be used. However, there are substances which show an extremely low fluorescence yield or even no fluorescence at all due to other fast decay pathways such as intersystem crossing.

When using diode laser-induced fluorescence (DLIF) spectroscopy, the extraordinary characteristics such as the high spectral intensity and well defined wavelength of diode lasers are specifically utilized. These allow a selective excitation of the sample and the manufacture of compact instruments (Barocsi et al., 2000; Gustafsson et al., 2000; Anderson et al., 2004). By using these lasers, it is possible to record the excitation spectra and thus the excitation wavelength as an additional parameter.

Simplicity, speed, sensitivity, non-destructiveness, and the ability to analyse both organic and inorganic materials using fluorescence spectroscopy are the main strengths of DLIF. Besides outstanding sensitivity and good selectivity, particular advantages of DLIF technique include the capabilities for *in situ* analysis and remote sensing. The major advantage of *in situ* laser-Induced fluorescence (LIF) measurements is absence of sampling and sample preparation procedures preceding the analysis. Such procedures are error-prone, time consuming and expensive.

A general concept for *in situ* analysis is to increase the dimensionality of the measured data. Since the substances have to be analyzed in a complex matrix and in the presence of other interfering compounds, higher information content is crucial for a subsequent analysis since there is no clean-up step and no separation involved. Therefore, the LIF system should be able to record multi-dimensional fluorescence data, for example, fluorescence intensity versus emission wavelength and time.

51

Optical Microscopy

Optical microscopy is the most efficient and reliable diagnostic technique being applied today. It is highly sensitive and specific in the sense that samples are visualized and identified by their features. One advantage of optical microscopy is that it can be used for species identification (Ross et al, 2006). The optical microscopy technique has been used for the detection of malaria parasites in the vertebrate host and it involves direct microscopy of fixed tissue or blood cells stained with differential stains such as Giemsa or with fluorescent dyes which are deoxyribonucleic acid (DNA) or ribonucleic acid (RNA) specific (Van Den Berg et al., 1991).

Resolution of an optical microscope is defined as the minimum separation needed between two media under examination in order for the microscope to discern them as separate media. If two media are separated by a distance shorter than the minimum distance (δ), they will appear as a single medium viewed under the microscope.

Generally, a measure of the resolving power of the lens of a microscope objective is given by its numerical aperture (NA):

$$NA = n \sin \alpha_o \tag{30}$$

where α_o is the angle spanned by the objective lens seen from the medium, and n is the refractive index of the medium (≈ 1 for air). State of the art microscope objectives can have a numerical aperture of up to 0.95. Because $\sin \alpha_o$ is always less than or equal to unity, the NA can never be greater than unity for a microscope objective lens in air.

$$\delta = \frac{0.61\lambda}{NA} \tag{31}$$

52

where λ is the wavelength of light. From this it is clear that a good resolution (small δ) is connected with a high NA. A combination of optical microscopic imaging and spectroscopy quantify several biological investigations (Teikari, 2008).

Spectral Imaging

Spectral imaging (SI) has proven extremely useful in numerous imaging applications, including object and material recognition, colour analysis and constancy, remote sensing and astronomy (Wellman, 1981; Mika, 1990; Sun & Anderson, 1993; Monnet, 1995; Abrardo et al., 1999; Hauta-Kasari et al., 1999; Slater & Healey, 1999; Stokman et al, 2000). The fields which find applications for SI are growing in number, for example, medical imaging, agriculture, archaeology, and art (Gat, 2000). Besides, SI has been suggested as a non-destructive method for identifying pigments (Frey & Warda, 2008; Cosentino, 2013).

Spectral imaging provides images at multiple wavelengths and hence generates precise optical spectra at every pixel (Richard et al., 2002). A spectral image can be considered as a three dimensional image cube $I(x, y, \lambda)$ where a 2-dimensional image records the spatial information of a sample, and the third dimension represents spectral wavelength. SI is an active field, made possible through the advances in charge-coupled device (CCD) detectors, dispersion optics, and spectral image processing algorithms (Yuval et al., 2006).

53

Imaging is the science and technology of acquiring spatial and temporal data information from objects for the purpose of obtaining information. At this time, digital imaging is the most advanced and applicable method where data are recorded using a digital camera, such as a charged coupled device (CCD). In biological studies, the images can be measured either by common optical methods such as optical microscopy or by more advanced methods that provides additional physical or chemical information about the objects.

Imaging spectroscopy is the simultaneous acquisition of spatially coregistered images, in many narrow, spectrally contiguous bands, measured in calibrated radiance units, from a remotely operated platform (Schaepman et al., 2009). Imaging spectroscopy is particularly useful for studying inhomogeneous samples or scenes. Examples include spatial classification based on spectral signatures, use of spectral libraries for material identification, mixture composition analysis, plume detection, etc (Gat, 2000).

Digital imaging was originally a field that has been developed in the early sixties to solve physical and technical problems by simulation, design and processing of pictorial data for analysis, visual inspection, measurement and visualization (Yuval et al., 2006). Currently, digital imaging has received a high level of maturity with a well founded rationale for many application fields (Matthias, 2006). It is the most advanced and applicable method where data is recorded using a digital camera, such as CCD. A digital image may be created directly from a physical scene by a camera or similar devices. Many technical images, which are not subject of our study, such as those acquired with tomographic equipment, or radio telescopes are actually obtained by

54

complex processing of non-image data. The best example of such imaging is magnetic resonance imaging (MRI). MRI is a medical imaging technique most commonly used in radiology to visualize detailed internal structures and limited functions of the body. It provides much greater contrast between the different soft tissues of the body making it very useful (Bersha, 2010).

The fields of classical imaging and optical spectroscopy have developed independently. While imaging deals with pictorial information that uses the description of material by their surfaces in terms of brightness, texture and color depending on the illumination in the two-dimensional field of view of the optics, spectroscopy classifies material properties due to their radiation in particular spectral bands but mostly limited to a single point of the object's surface (Stuart, 2004). Combining imaging devices and spectrographs to record point spectra for entire surfaces of objects leads to the new and emerging field of SI. Both spectroscopy and imaging are well developed and being used broadly in many fields.

The combination of optical imaging and spectroscopy creates a three-dimensional (3D) data set that contains many images of the same object, where each one of them is measured at a different wavelength, providing wealth of information that enables solutions for challenging tasks in various application sectors (Yuval et al., 2006). Imaging provides the intensity at every pixel of the image $I(x, y)$, spectroscopy provides a single spectrum, $I(\lambda)$ and therefore SI provides a spectrum at each pixel $I(x, y, \lambda)$ (Yuval et al., 2006). Figure 4 shows a spectral image data set and a spectral image cube. As a result, the spectral image provides a complete spectrum of the object at every pixel location throughout the lateral dimensions. Thus, a spectral image

55

cube can be considered as either a collection of images, each of which is measured at a specific wavelength, or as a collection of different wavelengths at each pixel location. The spectral image $I(x, y, \lambda)$ is commonly referred to in the scientific literature as image cube, spectral cube, and spectral hyper cube etc.
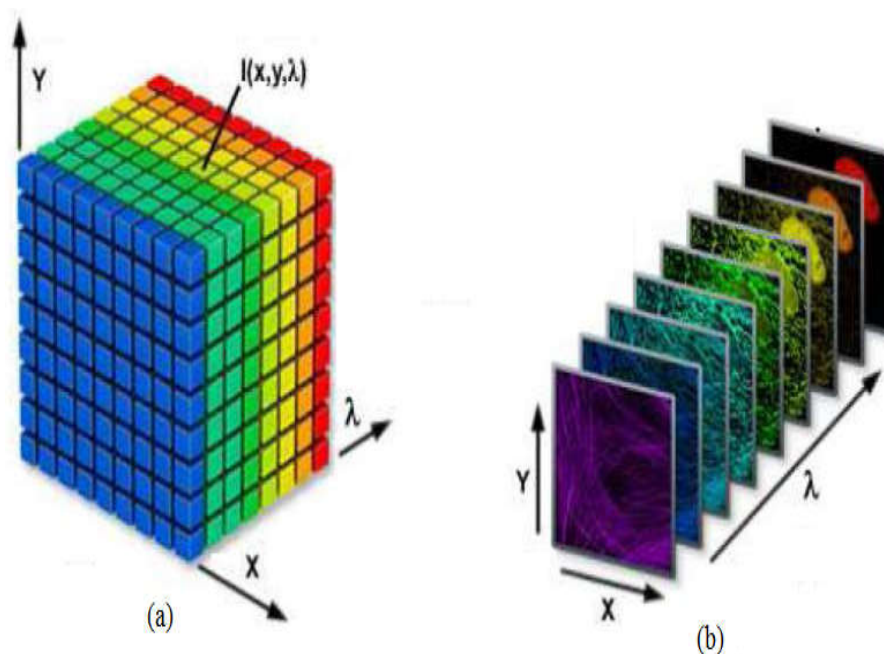
Figure 4: Description of a spectral image data set: (a) each point in the cube represents a single number and the spectral image is described as $I(x, y, \lambda)$ and (b) represents a series of spectral images (Dickson & Davidson, 2010).

There are two basic approaches for SI techniques. The first approach acquires a sequence of two dimensional images at different wavelengths. This can be implemented by using a rotating filter wheel or a tunable filter in front of a monochrome camera. The second approach acquires a sequence of line images, where for each pixel on this line, a complete spectrum is captured. This implementation requires an imaging spectrograph coupled to a monochrome matrix camera. One dimension of the camera (spatial axis)

56

records the line pixels and the other dimension (spectral axis) the spectral information for each pixel. To acquire a complete spectral image, either the object, or the spectrograph needs to be moved in small steps, until the whole object has been scanned (Matthias, 2006).

In digital imaging spectroscopy, each pixel acquires many bands of light intensity data from the spectrum (Schaepman et al., 2009). Simultaneous imaging in multiple spectral bands across the spectrum enables us to visualize details far beyond the capabilities of the human eye. When imaging is done at spectral bands between 2 to 100, we have multispectral imaging (MSI) and hyperspectral imaging (HSI) for more than 100 spectral bands. MSI and HSI systems, operated from ground, airborne and space-based platforms, have found a variety of applications. These technologies have applications in fields that range from environmental monitoring, geology, military surveillance, among others.

Spectral signatures acquired in MSI make it possible to discriminate among different types of materials (Nischan et al., 2003). Combined with telescopes, MSI exposes the secrets of the universe (Coffey, 2012). A multispectral image can be seen as:

$$F : R^2 \rightarrow R^m \qquad (32)$$

where R is the image and m is the number of bands. This function corresponds to a point (x, y) to a vector of functions:

$$F = f_1(x, y), f_2(x, y), ..., f_m(x, y) \qquad (33)$$

where f is intensity, and x and y, coordinates in the plane.

Spectral image cubes are analogous to a stack of pictures of an object, a sample, or a scene, where each image is acquired at a narrow spectral band.

Digitized by UCC, Library

Each pixel in the image cube, therefore, represents the spectrum of the scene at that spectral band (Gat, 2000). The nature of imagery data is typically multidimensional, spanning three spatial, one spectral, and one temporal dimension. Each point in this multidimensional space is described by the intensity of the radiance which is emitted, reflected, or a combination of both (depending on the phenomenology under investigation). Since detector arrays in image capture devices are two dimensional at most, they can only capture two dimensions of the data at a time, and another dimension displaced in time (Gat, 1999).

The data collected by imaging spectroscopy devices facilitates quantitative and qualitative characterization of spectral measurements. The results can be used for the identification of materials, such as biological samples and atmospheric trace gases based on the measurement of their relative concentrations, and subsequently the assignment of the proportional contribution of mixed pixel signals (e.g. spectral unmixing), the derivation of their spatial distribution (e.g. mapping), and finally their evolution over time (multi-temporal analysis) (Park et al., 2007; Jalil, 2008; Coffey, 2012). On a microscopic level, blood cells are spatially distributed by their refractive indices (Jacques, 1998; Bersha, 2010).

Colour discrimination varies widely in biological and technological vision systems. Even though humans can distinguish differently, millions of colour combinations, they cannot perceive all the optical and spectral information in their environment. This is because human eyes (as well as conventional colour films and colour digital cameras) separate visible light, no matter how spectrally complex, into only three colour components red, green

58

and blue (RGB), called the primary colours of light. Light with completely different spectral content can have precisely the same RGB coordinates. This is however not the case in multispectral imaging microscopy (MSIM) (CRI, 2010).

Multispectral imaging microscopy is obtained when optical imaging spectroscopy is done at several spatial locations at microscopic level, with transmittance ( ), at several wavelengths, (λ). MSIM at these locations and wavelengths is therefore represented as (x, y, λ) (Brydegaard et al., 2009). In most optical diagnostics, the aim lies in extracting all the information possible from a sample, which is generally impossible. In spectroscopy, the aim is to account for all photons emitted and to be able to explain whether they are absorbed, scattered, or re-emitted as fluorescence. The potential of measuring scattering, reflection and transmission of samples have advanced the MSIM significantly over a conventional transmission microscope (Svanberg, 2009; Merdasa, 2010). Application MSIM identifies hidden diseases (Coffey, 2012).

The power of MSIM arises from its ability to image a scene rapidly in numerous spectral bands. The spectral signatures acquired in this fashion make it possible to discriminate among different types of materials (Nischan et al., 2003). The chemical and physical properties of samples can be produced from MSIM, since a material's chemical and physical properties are dependent on its distribution within the sample. On the basis of MSIM data, quantitative and qualitative analysis of the sample can be performed (Morris, 1993; Colarusso et al., 1998).

Multispectral imaging microscopy uses a digital charge-coupled device (CCD) camera coupled with coloured filters of different spectral bands,

ranging from just three components, as in a RGB conventional camera, up to hundreds of components, as in a hyperspectral system (Nieves et al., 2005). MSIM system employs more than three narrow band filters which result to greater spectral sensitivity compared to the conventional RGB imaging system which utilizes three broadband filters (Bautista & Yagi, 2011). The main application is spectral recovery, and therefore these techniques have been applied intensively in areas as diverse as artificial vision, industrial colorimetry, biomedical engineering, and medicine (Jalil, 2008). Of particular interest is their application in atmospheric optics and remote sensing, where it is difficult to obtain high spectral and high spatial resolution at low cost (Nieves et al., 2005).

In many cases, the availability of a larger number of spectral bands has created important competitive advantages with regards to techniques based on MSIM. In MSIM data, the detectable number of pure spectral signatures (end members) is often less than the effective number of end members present. MSIM devices, when combined with image processing techniques, can solve portability and cost problems and recover either spectral reflectance or the illumination spectrum at each pixel of a captured image with good spectral resolution (Clark, 1999).

Multispectral imaging microscopy systems are not designed to sample a large portion of the EM spectrum at a fine detail, and may miss important information contained in the non-sampled bands. Diagnostic absorption features that characterize materials often occur over a small portion of the spectrum (Clark, 1999).

60

Now it is understandable that the amount of information available in MSIM is almost endless, so it would be very costly and inefficient to try to collect all data throughout the electromagnetic spectrum. An analytical device is made with a definite number of spectral bands in the region of interest for experiments. The imaging device is capable to simultaneously collect spectral data from several regions in space discredited, leading to both the collection of spatial and spectral data from many points in a three-dimensional image.

Components involved in the acquisition process of a MSIM system are illustrated in the Figure 5. $I_R(\lambda)$ is the spectral radiance of the illuminant, $r(\lambda)$ is the spectral reflectance of the surface, $O(\lambda)$ is the spectral transmittance of the optical system, $_k(\lambda)$ is the spectral transmittance related to the kth filter and $a(\lambda)$ is the spectral sensitivity of the camera (Jalil, 2008). The camera output d_k, related to the channel k for a single pixel of the image, and is given by equation 36.
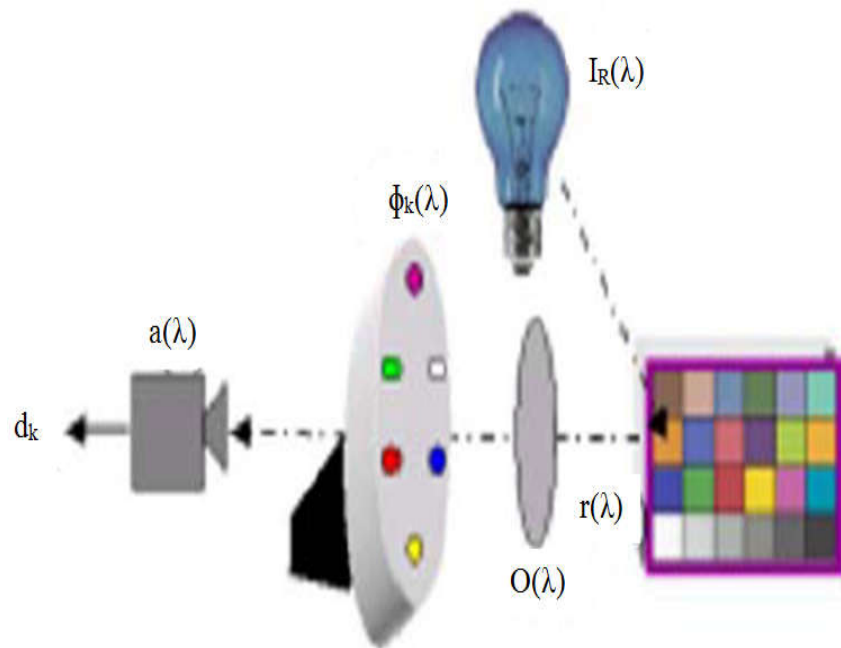
Figure 5: Synopsis of the spectral model of the acquisition process in a multispectral system (Jalil, 2008).

61

$$d_k = \int_{\lambda_{\min}}^{\lambda_{\max}} I_R(\lambda) r(\lambda) O(\lambda) a(\lambda) \Phi_k(\lambda) d\lambda \qquad (34)$$

The vector of the sampled spectral reflectance of the scene $r(\lambda)$ is also given as:

$$r(\lambda) = [r(\lambda_1), r(\lambda_2), ..., r(\lambda_n)]^{TP} \qquad (35)$$

where TP is the transpose operator. Assuming a linear optoelectronic transfer function, $I_R(\lambda)$, $a(\lambda)$, $O(\lambda)$ and $\Phi_k(\lambda)$ can be replace by the spectral sensitivity $S_k(\lambda)$ of the kth channel. Then, the equation 34 becomes:

$$d_k = \int_{\lambda_{\min}}^{\lambda_{\max}} r(\lambda) S_k(\lambda) d\lambda \qquad (36)$$

where S_k, the vector containing the spectral sensitivity of the acquisition system in relation to the kth channel is given as

$$S_k(\lambda) = [S_k(\lambda_1), S_k(\lambda_2), ..., S_k(\lambda_N)]^{TP} \qquad (37)$$

By sampling the spectra to N wavelengths, equation 36 can be written in matrix notations as shown in equation 38.

$$d_k = r(\lambda)^{TP} S_k(\lambda) \qquad (38)$$

From equation 38, the spectral response of the system is firstly characterized, including the camera and the illuminant, by finding the operator $S_k(\lambda)$. Then, using this operator from a spectral image, the spectral reflectance curve for each pixel of the imaged scene, is reconstructed (Jalil, 2008).

Applied Multivariate Analysis Techniques

Multivariate analysis (MVA) comprises set of techniques dedicated to the analysis of data sets with more than one variable. Several of these techniques were developed recently in part because they require the computational capabilities of modern computers. Also, because most of them are recent, these techniques are not always unified in their presentation, and the choice of the proper technique for a given problem is often difficult (Lewis-Beck et al., 2003).

Some of the applied multivariate analysis techniques are Clustering analysis, principal component analysis (PCA), correspondence analysis, multiple correspondence analysis, multidimensional scaling, additive tree, cluster analysis, multiple linear regression analysis, partial least square regression, principal component regression and ridge regression. The rest are reduced rank regression, multivariate analysis of variance, discriminant analysis, confirmatory factor analysis, multiple factor analysis and canonical correlation analysis. Among these MVA techniques, the most commonly used for classification of biological data are the CA and the PCA (Jain & Dubes, 1988).

Clustering Analysis

Clustering analysis or simply clustering is the process of organizing a set of data into groups in such a way that observations within a group are more similar to each other than they are to observations belonging to a different group. Clustering is also known as an unsupervised learning process that assumes that the data set represents features that would allow one to

63

distinguish one group from another. It is known as unsupervised learning process because it does not require prior knowledge of the number of groups in a data set.

Clustering is defined in terms of two functions, the distance function and the linkage function. The distance function computes the distance between points and the linkage function computes the distance between clusters. Clustering results often vary based on the choice of these functions. Let A and B be two clusters containing two ponts a_α and b_β respectively. Generally, the distance between the two points a_α and b_β is defined by

$$d_p(a_\alpha, b_\beta) = \left(\left| \sum_{k=1}^{K} a_{\alpha,k} - b_{\beta,k} \right|^p \right)^{1/p} = \left\| a_\alpha - b_\beta \right\|_p, p > 1 \qquad (39)$$

called the Euclidean distance. The Euclidean distance has an intuitive appeal as it is commonly used to evaluate the proximity of objects in two or three-dimensional space. The distance between the two clusters also is defined as:

$$\varphi(A, B) = \min \varphi(a_\alpha, b_\beta) \qquad (40)$$

known as a single-linkage criterion (Jain & Dubes, 1988; Jain et al., 1999). The clusters depend on the choice of a clustering distance. If two points satisfy the condition that $\varphi(A, B) \leq d$, then A and B are combined into a single cluster.

The linkage function clusters all groups in a data set hierarchically by their similarity. The visualization of the linkage structures are often plots referred to as dendrograms. Dendrograms are tree diagrams that show nested structure of partitions and how various groups in the data set are linked at each stage. Dendrogram can be represented horizontally or vertically.

64

Principal Component Anaysis

Principal component analysis (PCA) is a non-parametric method of extracting relevant information from a multidimensional data set, X, by reducing the complex multidimensional data set to a lower dimension such that the principal hidden or latent factors are revealed. The reduced-dimensional space help build more effective data analyses for classification, pattern recognition clustering and so on. PCA produces a new set of dimensions or axes against which the original multidimensional data set is represented, described or evaluated. This analysis approach enables one to discover and work with the principal latent components rather than the original data.

When two or more signals or dimensions are highly correlated or dependent, they are likely to represent highly related phenomena. Thus, the variances in the data are where the signals or dimensions can be best discriminated and key underlying phenomena observed. So, in PCA, correlated variables are combined and uncorrelated ones, particularly the observations that have high variance, are focused on. At the end of the analysis, smaller set of variables that explain most of the variance in the original data, in more compact and insightful form is sought for. The new variables or dimensions in PCA are linear combinations of the original ones and uncorrelated with one another, that is, orthogonal in the original dimension space. The new variables are captured as much of the original variance in a data set as possible and are called principal components, (PCs). The PCA as a projection method projects the experimental multidimensional

65

data set onto new axes, the principal components (PCs), and gives better representation of the data set without losing much information.

Principal component analysis is considered as a form of rotation of the existing axes to new positions in the space defined by original variables. The new dimensions or axes are orthogonal and stand for the directions with maximum variability. The multidimensional data set, X of m observations and n variables is centered X_c such that the elements of the matrix of dimension $m \times n$ are on the sample mean of zero. The X_c is then converted into covariant matrix S defined as

$$S = \frac{1}{m-1} X_c{}' X_c \tag{41}$$

where $X_c{}'$ denotes the matrix transpose of X_c. Each column in the captured data corresponds to one variable and one row corresponds to the values observed at one point at a time. Thus, the data points are vectors in a multidimensional space and the PCA of the data gives vectors of scores, with values that summarize all the variables entering the analysis. The square, symmetric, nonsingular covariant matrix S is further transformed into a diagonal matrix using the relation below,

$$M = \beta' S \beta , \tag{42}$$

where the columns of β contain the eigenvectors of S and M is a diagonal matrix with the eigenvalues along the diagonal. β is used to obtain new variables called Principal Components (PCs).

66

Optics of Haemoglobin

In diffuse optical spectroscopy, wavelengths of interest span the spectral range from the UV to the NIR. This is the region which is sensitive to the optical absorption and scattering of soft tissues. The shape and magnitude of absorption depends on the concentration of the dominant tissue absorbers as well as their extinction coefficient (an inherent measure of a constituent's ability to absorb light energy). In biological tissue, absorbers of interest include haemoglobin (Hb), beta-carotene, melanin and proteins in the UV-NIR spectrum.

Within the water window of transparency, the most dominant absorption of NIR light is by Hb in its various forms. Hb which is a chemical protein contained inside RBCs are regularly moving throughout human body. It is responsible for delivering oxygen from the lungs to the body tissues and returning waste gases, such as carbon dioxide, to the lungs to be exhaled. Changes in Hb contact exert a visible influence on oxygen binding (Nagai et al., 2008; Nabil, 2008). Hb constitutes approximately 40-45% of whole blood and consists of the protein globin bound to four haem groups. Each haem group contains an iron atom at the centre of a ring-like structure.

An iron atom in the ferrous (Fe^{2+}) form will bind physically to an oxygen molecule to become oxygenated, as opposed to oxidised which would involve a chemical bond. Thus, one Hb molecule with its four iron centres can carry a total of four molecules of oxygen, in which case it is said to be 100% saturated. Hb is one of the strongest absorbers of light in the human body and exhibits significant dispersion throughout the VIS region (Hammer et al, 1999; Park et al, 2009). With regard to the spectroscopic characteristics, Hb

absorption is centered at 400-450 nm (Soret band) and 660 nm (Horecker, 1942; Zijlstra, 1991; Svanberg, 1992; Faber et al., 2004; Denninghoff et al., 2007; Svanberg, 2009; Akuwudike et al., 2010). The Soret band is characteristic of hematoporphyrin proteins (Murray, 2003; Nelson & Cox, 2005; Akuwudike et al., 2010).

Hemoglobin shows a stronger absorption of light in the UV, VIS and NIR regions. This is because the relative good transparency of tissues in the VIS and NIR spectrum allows light signals to penetrate up to a few centimeters into tissues (Barun & Ivanov, 2009; Akuwudike et al., 2010; Merdasa, 2010). The light interaction with tissue can be quantified in terms of optical parameters such as absorption and scattering coefficients, which are found by making suitable measurements (frequency domain or time-resolved techniques), and applying a suitable model-based reconstruction method (Arridge & Schweiger, 1997).

Haemoglobin molecules comprise approximately 97% of the cell solids (Ross, 1967). The RBCs have a biconcave shape, with a main diameter of approximately 8 μm and a cross-sectional thickness of 1-2 μm. The cell is bound by a membrane approximately 8 nm in thickness. Fibrous proteins in the membrane allow the cells enough flexibility to deform their shape, in order to fit through capillaries of smaller diameters than themselves. Since there is a RI mismatch between the cell membrane and the surrounding medium, i.e. plasma in whole blood, the RBC will scatter light.

Red Blood Cells (RBCs) contain thin membrane and aqueous Hb solution. Therefore, the cells can deform in order to flow through capillaries in the human body. Morphological changes of the cells can inhibit the flexibility

68

of the cells in the blood stream, which can cause stroke. Hb essentially determines the refractive index of the RBCs and varying concentrations of the blood will therefore yield variations in refractive index from cell to cell (Merdasa, 2010).

Regarding interaction of Hb with light, the Kramers-Kronig dispersion relation relates the imaginary part of the RI (n_{Im}) to the molar absorption coefficient (ε_μ), according to equation 43.

$$n_{Im} = \ln(10)\frac{\lambda}{4\pi\varepsilon_\mu c} \tag{43}$$

where λ is wavelength of light source and c is concentration of Hb. Blood is one of the media through which human beings get their diseases including malaria.

In the oxygenated state, Hb is known as oxyhaemoglobin (HbO_2). The de-oxygenated form, with no oxygen molecules attached, is known as deoxyhaemoglobin (dHb). The absorption of tissue is related to the concentration of the main chromophores present in the tissue, such as HbO_2, dHb and water.

Absorption spectra of HbO_2 and dHb are somewhat different, hence the difference in colour between arterial and venous blood. The absorption curves for both HbO_2 and dHb have several strong bands in the VIS part of the EM spectrum. The molar extinction coefficient for both HbO_2 and dHb is very high from 405-450 nm (Altshuler, 2004). Therefore, incident radiation in this range will be very highly absorbed by blood, and the penetration of light through the papillary dermis will be very difficult because of the presence of a plexus of blood vessels.

The absorption spectra of HbO$_2$ and dHb, shown in Figure 6 (Cope, 1991), differ significantly, particularly in the red region of the VIS and the NIR. This difference in absorption explains the visible colour difference between venous and arterial blood. Arterial blood, which in adults is usually about 98% oxygen saturated, is bright red, whereas venous blood, which is approximately 75% saturated, appears dark red to purple in colour.
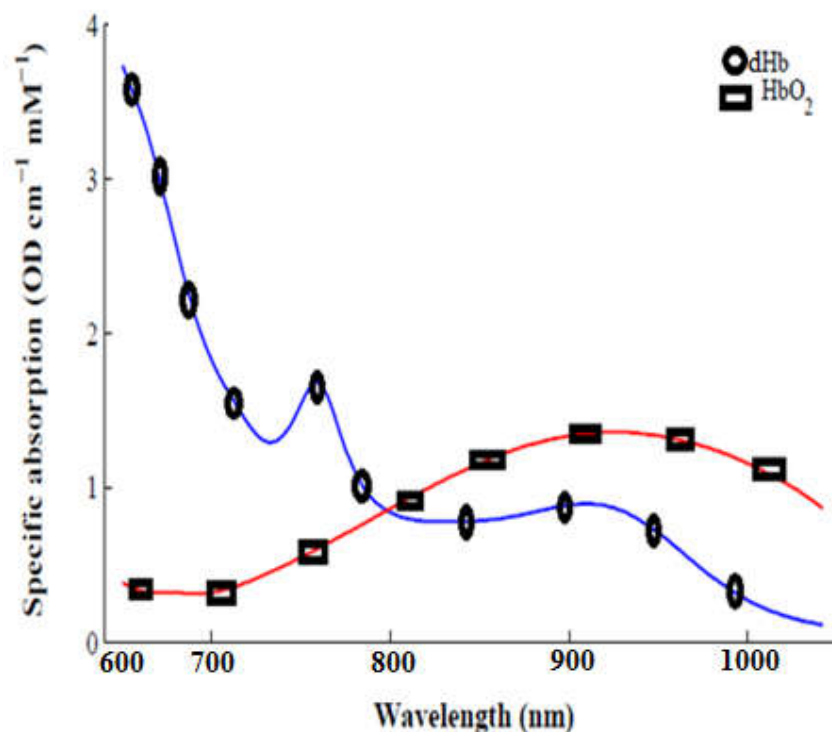
Figure 6: Absorption spectra of oxygenated haemoglobin (HbO$_2$) and deoxygenated haemoglobin (dHb) (Cope, 1991).

Although the NIR absorbances are reduced in amplitude relative to those in the VIS region, the spectra are still sufficiently different to distinguish between the two forms of the Hb. A typical value for Hb concentration in the adult brain has been calculated to be 84 μM (Cope, 1988). Foetal Hb (fHb) differs from adult Hb (aHb) in that it has a higher affinity for oxygen. This facilitates the uptake of oxygen by the foetus from the placenta, where the

70

diffusion distance is greater than in the lung, and ensures a constant supply of oxygen to the growing cells of the foetus. fHb is gradually replaced by aHb in the months after birth. Although the NIR spectra of fHb and aHb are slightly different, Wickramasinghe et al. (1993) determined no significant difference in the analysis of foetal cerebral oxygenation using either spectrum (Wickramasinghe et al., 1993). Other forms of Hb that absorb in the NIR are carboxy Hb (HbCO), met Hb (metHb) and sulf Hb (sHb). However, these derivatives are generally ignored in spectroscopic measurements, either because they have a low percentage concentration in blood or a low specific absorption, or both (Cope, 1991).

Scattering by dHb shows significant characteristics at wavelengths in the NIR region (MacRae et al., 1961). Lothian and Lewis found minimum scattering coefficients of Hb near maximum absorption bands. This effect appears to be caused by a combination of interference and anomalous dispersion related scattering (Lothian & Lewis, 1956). Scattering by dHb can be divided into two general types. These are large-particle effects, thus, interference and diffraction phenomena, which occur mostly at small angles and other effects such as specular reflection, refractive bending and small-particle scattering from parts of the cell.

Malaria

Malaria, caused by *Plasmodium* parasite, still remains the most devastating human disease that affects over half a billion people worldwide and is responsible for more than 2 million deaths per anum (Sachs & Melaney, 2002; Hay et al., 2004; Amexo et al., 2004; Paton et al., 2011; WHO, 2011; WHO, 2013). Malaria is mostly restricted to poor tropical areas of Latin America, Asia and Africa, causing huge toll on lives, in medical costs and in days of labour lost (Sachs & Melaney, 2002). About ninety percent of the mortalities caused by malaria occur in sub-Saharan Africa (Sachs & Melaney, 2002; Gollin & Zimmermann, 2007). Nine out of ten mortalities caused by malaria are among children below five (5) years in most developing countries (Amexo et al., 2004). Mortalities in these countries remain high because there is insufficient access to treatment. Early diagnosis and treatment will help reduce further complications of the disease and prevent deaths (Gallup & Sachs, 2001; Weatherall et al., 2002).

Malaria can infect both vertebrates and invertebrates using the blood as host. In humans, malaria is caused by infections from *Plasmodium falciparum* (*P.falciparum*), *Plasmodium malariae* (*P.malariae*), *Plasmodium ovale* (*P.ovale*) and *Plasmodium vivax* (*P.vivax*) (Nadjm & Behrens, 2012). Among these species, *P.falciparum* accounts for the majority of worldwide deaths (Sarkar et al., 2013). The size of the *P.falciparum* parasite is within the range of 1 μm to 15 μm. Larger gametocytes of *P.falciparum* only rarely exceed 10 μm in the longer axis. Therefore considerable magnification is required to see species in detail for differential diagnosis and the ideal range is somewhere between x500 and xl000 of total magnification (Payne, 1988).

72

Red blood cells (RBCs) infected by *P.falciparum* parasites (*i*-RBCs) undergo irreversible changes in structure and biophysical characteristics, which can lead to a drastic change in blood circulation. A key feature of *P.falciparum* is the ability of the *i*-RBCs to adhere to the linings of small blood vessels (Weatherall et al, 2002). *P.falciparum* infections are accompanied by profound changes in the mechanical properties of the *i*-RBCs of the host, contributing to reduce blood flow in the microcirculation and vasoocclusion (Mauritz et al., 2010).

The membrane shear modulus of the *i*-RBCs may increase up to ten-fold causing capillary occlusions (Shelby et al., 2003), thereby resulting in substantial increase in resistance to blood flow. Such effects may be intensified due to the enhanced cytoadherence of the *i*-RBCs to the vascular endothelium (Ho & White, 1999; Ho et al., 2000; Dondorp et al., 2004). This adherence of the *i*-RBCs is believed to be the main cause of bleeding complications in cerebral malaria due to blockages of small vessels in the brain (Fedosov et al., 2010).

Generally, *P.falciparum* life cycle consists of an asexual phase in the vertebrate host (schizogony) and a sexual phase in the mosquito vector (sporogony). The former takes place inside the human body and the latter inside the mosquito. The two processes are concurrent. Mosquitoes ingest *P.falciparum* gametocytes in a blood meal from an infected vertebrate host, and the gametocytes then develop into infectious form (sporozoites) within the salivary glands of the mosquito. Sporogony in the mosquito takes approximately 10 - 20 days, and thereafter the mosquito remains infective for 1 - 2 months (Nogueira & da Rosario, 2010). Sporozoites (the protozoan cells

73

that develop in the mosquito's salivary gland and used to infect new hosts) are the form of existence of the parasite inside the mosquito.

This life cycle of the *P.falciparum* parasite involves three phases of development: exo-erythrocytic stages in the tissues, usually the liver, erythrocytic schizogony (i.e. protozoan asexual reproduction) in the erythrocytes and the sexual process, which begins with the development of gametocytes in the host and continuing with the development in the mosquito. Figure 7 summarizes the life cycle of the *P.falciparum* parasite. When humans are bitten by an infected mosquito, the sporozoites enter the blood stream, where they remain for about half an hour and then disappear. Many are ruined by the body's immune system, but some enter the cells in the liver, which appears to be a place of comfort for the asexual reproduction of the parasite. Here they multiply rapidly by a process referred to as exo-erythrocytic schizogony. Inside the liver cells, one sporozoite divides into about 30 000 to 40 000 merozoites (about 1μm in diameter). When a liver cell can no longer hold dividing cells, it bursts and the merozoites re-enter the blood stream targeting the RBCs. When the released merozoites enter RBCs, the erythrocytic cycle begins. This process is referred to as erythrocytic schizogony.
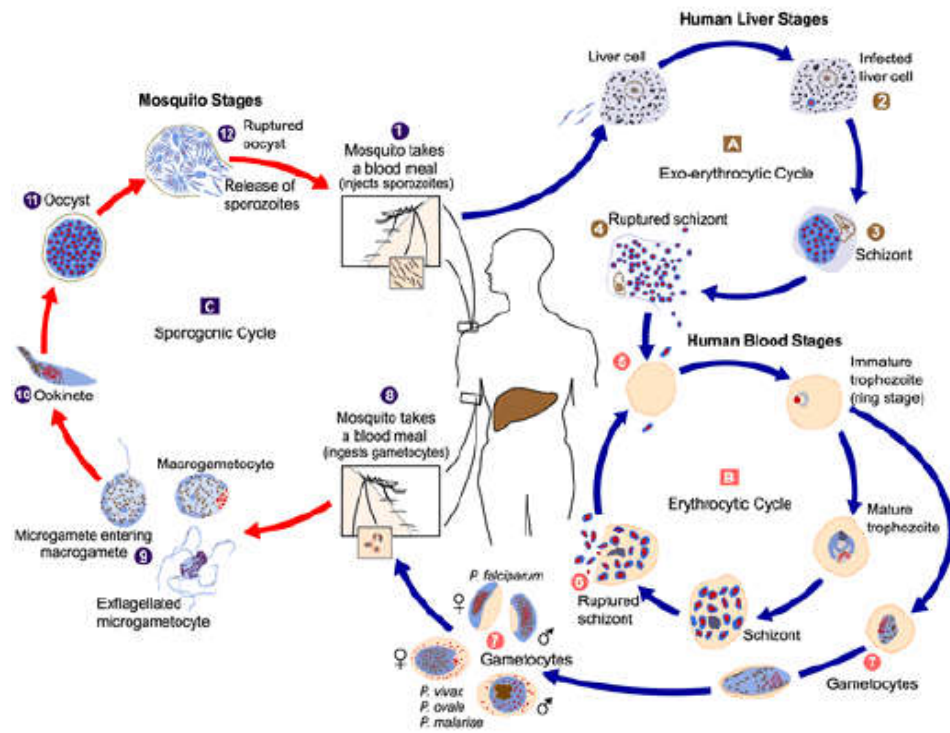
Figure 7: The malaria life cycle of the *Plasmodium falciparum* parasite in the *Anopheles* female mosquito as well as in a human (Centre for Disease Control (CDC), 2010).

Within RBCs, the parasite is first seen microscopically as an immature, minute speck of chromatin trophozoites termed as ring-shaped and grows to the mature stage. Hb degradation occurs predominantly during the trophozoite stage of the erythrocytic life cycle of the *P. falciparum* parasite (Rosenthal et al., 1988; Moore et al., 2006). As the nucleus begins to divide, the parasite is known as a schizont. The surface of *P.falciparum* trophozoite and schizont stages *i*-RBCs is covered with knob-like excrescences that are the contact points with host cells (Weatherall, 2002).

Dividing nucleus tends to take up peripheral positions and a small portion of cytoplasm gathers around each nucleus. The *i*-RBCs rupture and release a number of merozoites which attack new corpuscles and the cycle of erythrocytic schizogony is repeated. The infections about this time enter the

75

phase in which parasites can be detected in blood smears. The human host starts experiencing symptoms for the first time with acute fever and chills. These symptoms repeat every 2-3 days, as this is the time it takes for the erythrocytic shizogony to complete.

Clinical observations and experimental evidence indicate that, during schizogony, the *P.falciparum* and its host RBCs are exposed to enhanced oxidative stress, mainly due to parasitic Hb digestion and the host as immune response (Lüersen, 2000). Although the RBCs, as well as the parasites, are supplied with antioxidative systems (Hunt & Stocker, 1990; Ginsburg & Atamna, 1994), it was shown that the balance of pro and anti-oxidants in the parasite-host unit is very fragile and susceptible to additional exogenous oxidative stress (Clark & Hunt, 1983; Wozencraft, 1986; Vennerstrom & Eaton, 1988).

After a couple of cycles, some merozoites develop into gender specific gametocytes, which cannot be reproduced sexually in the human host. Consequently, the gametocytes travel in the blood stream until another female *Anopheles* mosquito bites the human. These gametocytes then enter the blood stream of the mosquito where sexual reproduction occurs. After a couple of reproductive steps inside the mosquito, new sporozoites are again collected in the salivary glands of the mosquito, ready to enter a new human host, and the cycle is complete.

In *P.falciparum* infections, progression through the parasite development stages in hosts (ring → mature trophozoite → schizont) leads to a considerable stiffening of *i*-RBCs compared to *u*-RBCs (Fedosov, 2010). Furthermore, in the schizont stage, the RBCs shape becomes near-spherical

76

whereas in the preceding stages RBCs maintain their biconcavity. An important difference between *P.falciparum* and other human malaria parasites is the way the *P.falciparum* modifies the surface of the RBCs for adherence of both asexual parasites and gametocytes to the endothelium and asexual parasites within placenta. As a result, only ring forms of *P.falciparum* are found within the circulating blood (Weatherall, 2002). *P.falciparum* invades and develops within host RBCs during 48-hour asexual cycle (Moore et al., 2006). During this period, parasites undergo progression from single-nucleated rings to multi-nucleated schizonts by consuming nutrients generated by degrading Hb within a digestive vacuole (DV). The progenies formed known as merozoites then break open the membrane and cytoskeleton of the *i*-RBCs to establish a new cycle of infection.

The parasite detoxifies heme by converting it into a dark brownish colour product called hemozoin, also known as malaria pigment. The hemozoin is formed from detoxified and crystallized heme together with iron derived from partially metabolized Hb (Loyevsky et al., 2001). Diagnosis of malarial infection is carried out through the examination of the hemozoin in the smeared blood slide with a white light illuminated microscope. Digestion of Hb produces amino acids (Sherwan, 1977), which fills the entire RBC. As a result it bursts, and throws hemozoin, amino acid and Hb into the extracellular media.

In particular, development stages and presence of hemozoin pigment-containing asexual parasites is recognized when accounting for *P. falciparum* infections. This information may indicate the possibility of a more severe clinical situation, particularly cerebral involvement, owing to the release into

the peripheral blood circulation of developing schizont stages of the parasites confiscated in the capillaries. Under these circumstances, modification of the method of drug administration from the oral route to the intravenous route may need to be considered (Moody, 2002).

As the parasites mature and differentiate within a growth-permissive parasitophorous vacuole (PV), the *i*-RBCs undergo extensive morphological alterations (Nash et al., 1989; Chandramohanadas et al., 2011). This indeed affects the oxygen transporting capability (Suresh, 2006; Park et al., 2008). Towards the end of parasite's intra-erythrocytic life cycle, the initially biconcave *i*-RBCs become more spherical in shape and less deformable. Nanoscale knobs formed on their external surfaces facilitate significantly increased cytoadherence to the endothelium of the vasculature to ensure diminished clearance in spleen (Kilejian, 1979).

Plasmodium falciparum diagnosis and treatment are of great interest due to the high death rate caused by the *P.falciparum* parasite, especially in developing countries. In *P.falciparum* infected patients, a prompt and accurate diagnosis is the key to effective disease management (Sachs & Melaney, 2002; Hay et al., 2004; Amexo et al., 2004; Paton et al., 2011). A major decision factor in the *P.falciparum* diagnosis is evaluation of the degree of infections manually termed as parasite densities (PDs). This manual counting of the parasites from thick or thin Giemsa-stained blood smears slides is done by a trained laboratory technician (Pammenter, 1988; Payne, 1988; Lopez-Antunano, 1990; Oaks et al., 1991; WHO, 1991; Makler et al., 1998; Bloland, 2001; Coleman et al., 2002; Mitiku et al., 2003; Bates et al., 2004; Ross et al., 2006; Sio, et al., 2006; Tek et al., 2009; Paton et al., 2011; Savkare & Narote,

2011). The ability of the trianed laboratory technician to detect the *P.falciparum* parasites depends on the number of fields examined under the microscope (Thomson et al., 2000; Ross et al., 2006; Sio et al., 2006; Tek et al., 2009; Paton et al., 2011).

Precision of clinical assessment differs with the level of endemicity, malaria season, and age group. No single clinical algorithm is a universal predictor (Chandramohan et al., 2002; Mwangi et al., 2006; Dicko et al., 2008). Studies of fever cases in populations with different *P.falciparum*-attributable proportions from some countries in Asia and Africa have shown a wide range of percentages (40-80%) of *P.falciparum* infections over-diagnosis and its associated potential for economic loss (Mwangi et al., 2006; Dicko et al., 2008). Only in children in high-transmission areas can clinical diagnosis determine the treatment decision (WHO, 2000; Chandramohan et al., 2002).

A trained laboratory technician will examine and count the parasites from blood smears under a microscope, as shown in Figure 8. If the parasites are present, the diagnosis is confirmed. A "thick" smear makes it possible for the laboratory technician to examine a large amount of blood. Then, the species of parasite can be identified by looking at a corresponding "thin" smear. This is important for deciding on the best treatment (WHO, 2005). Mixed infections are possible. For example, a person can be infected with *P. vivax* as well as the more dangerous *P.falciparum* (U.S. Department of Health and Human Services, 2007).

Using light microscopy with a 100x oil-immersion objective, a well stained thick or thin blood smear slides remain the standard technique for detecting the *P.falciparum* parasites. It can detect the PDs as low as 5-10

parasites per micro liter when used by the trained technicians or 100 parasites per micro liter under field conditions.

Figure 8: Laboratory technician using light microscopy for *P.falciparum* diagnosis (Kyowa Optical, 2007).

In thick blood smear slides, the total number of parasites per 200 white blood cells (WBCs) are counted and multiplied by 40 to give the number of parasites/µl (after assuming that there are always 8000 WBC/µl blood. A second method involves making a thick smear with a known, small volume of blood (0.3 µl) drying the smear, staining it with Giemsa's stain and then counting all the parasites on the smear The total number of parasites counted is then multiplied by 3.33 to obtain the number of parasites/µl (Warhurst & Williams, 1996). A similar technique again uses a defined amount of whole blood to make a thick blood smear and then the parasites present in 100 high-power fields (HPF) are counted. One parasite/100 HPF is assumed to be equivalent to 50 parasites/µl. A thick smear is generally considered negative if

80

no parasites are seen after 600 seconds of searching (Warhurst & Williams, 1996).

Parasite levels may also be counted by examination of a thin blood smear slides. This is usually accomplished by counting the number of parasites/1000 RBCs; or, again, by counting the number of parasites per 200 WBCs and then multiplying by the factor (Warhurst & Williams, 1996; Makler et al., 1998).

In the unusual event that the *P.falciparum* parasites cannot be seen immediately in a blood smear, but the patient's condition and prior activities strongly suggest *P.falciparum* infections, a doctor may decide to start treatment before being sure about the patient infections. Any detection of *P.falciparum* infections is considered a medical emergency and delays in starting treatment are the leading cause of death (U.S. Department of Health and Human Services, 2007).

The parasites counting are highly valuable for technicians, as it is an important determinant of treatment schedules for *P.falciparum* infections. For example, if the number of parasites exceeds 10% in *P.falciparum*, exchange transfusion may be indicated. *P.falciparum*, unlike the other human malaria species, has the capacity for nearly unlimited replication in the human host and very high number of parasites (>50% of i-RBCs) are possible in *P.falciparum* infections (Warhurst & Williams, 1996).

The manual counting process more often than not involves threshold-based counting techniques (Dowling & Shute, 1966; Trape, 1985; Kremsner et al., 1988; WHO, 2010; Planche et al., 2001; Garcia et al., 2004; Le Port et al., 2011), which may vary from one method to another. A statistical approach in

81

estimating the *P.falciparum* parasites focusing on variable threshold values has been studied (Hammani et al., 2013). A comparative analysis study in *P.falciparum* parasites estimation among children below 5 years shows significant underestimation of the parasites burden and a statistical agreement parasite density (Adu-Gyasi et al., 2012).

The ability to study both *i*-RBCs and *u*-RBCs in an environment more closely resembling their native environment would be very beneficial, not only for the diagnosis of *P.falciparum* infections but for the study of any biological sample. It will allow for future studies to observe other biological cells alive in a homeostatic environment and, by keeping the cell/parasite alive, allow for the same cell to be studied over the life cycle of either the cell or its infecting parasite. This may lead to a clearer understanding of the Hb degradation process and provide data that will be useful in the development of anti-malarial therapies.

CHAPTER THREE

INSTRUMENTATION, EXPERIMENTAL METHODS AND

PROCEDURE

This chapter presents instrumentation, processes for blood sample collection and preparations, as well as experimental methods and procedure for data acquisition. So, the first part of this chapter looks at instrumentation for assembling a multi-functional imaging microscope; the second part presents processes for blood sample collection and preparations; experimental methods and procedure for data acquisition involving fluorescence excitation spectral technique, spectrophotometry application for determining absorption bands and optical density of the blood samples, in addition to spectral and fluorescence imaging techniques for capturing images from unstained blood smear slides are presented in the final part of this chapter.

Multi-Functional Imaging Microscope Instrumentation

Components

A multi-functional imaging microscope (MFIM) was assembled for microscopic imaging using diode lasers as illumination light sources. This type of microscope was chosen because of its flexibility, capability and adjustability for fluorescence imaging apart from the usual transmission imaging and reflection imaging.

The MFIM is made up of mechanical, optical and optoelectronic components. The mechanical components are breadboard (Thorlabs Inc.,

83

MB4) and motorized translation stages (Thorlabs Inc., MTS25/M-Z8). The optical components are made up of the Reflx objective (Edmund Optics[©], 2000, x15 magnification and 0.28 NA), beam splitter (BS) (Edmund Optics[©], BS016), optical diffuser (Edmund Optics[©], 2000), achromatic doublet lenses (ADLs) (Thorlabs Inc., AC254-060-A, AC254-030-A), neutral density filters (Thorlabs Inc., NDM2) and optical fibre: 1 mm 0.39 NA 50 mm bend radius ultra violet (UV)-visible (VIS) (UV-VIS) multimode (Ocean Optics Inc., M35L01). The optoelectronic components consist of Guppy F-503B imager (Allied Vision Technology, MT9P031), data acquisition device (DAQ) USB-6009 (National Instruments[©], 2010), diode lasers (O-Like) and cube motor controllers (Thorlabs Inc., TDC001).

Assembling

Figure 9 shows a schematic diagram of the MFIM. The figure shows two illumination laser sources in: reflection mode (RM) and transmission mode (TM).

A: doublet lens (25 mm)
B: doublet lens (12.5 mm)
C: Neutral density filters
D: Optical fibre
E: Reflx objective
F: Beamsplitter
G: Imager
H: Motor controllers
I: Laptop computer
RM: Reflection mode
TM: Transmission mode
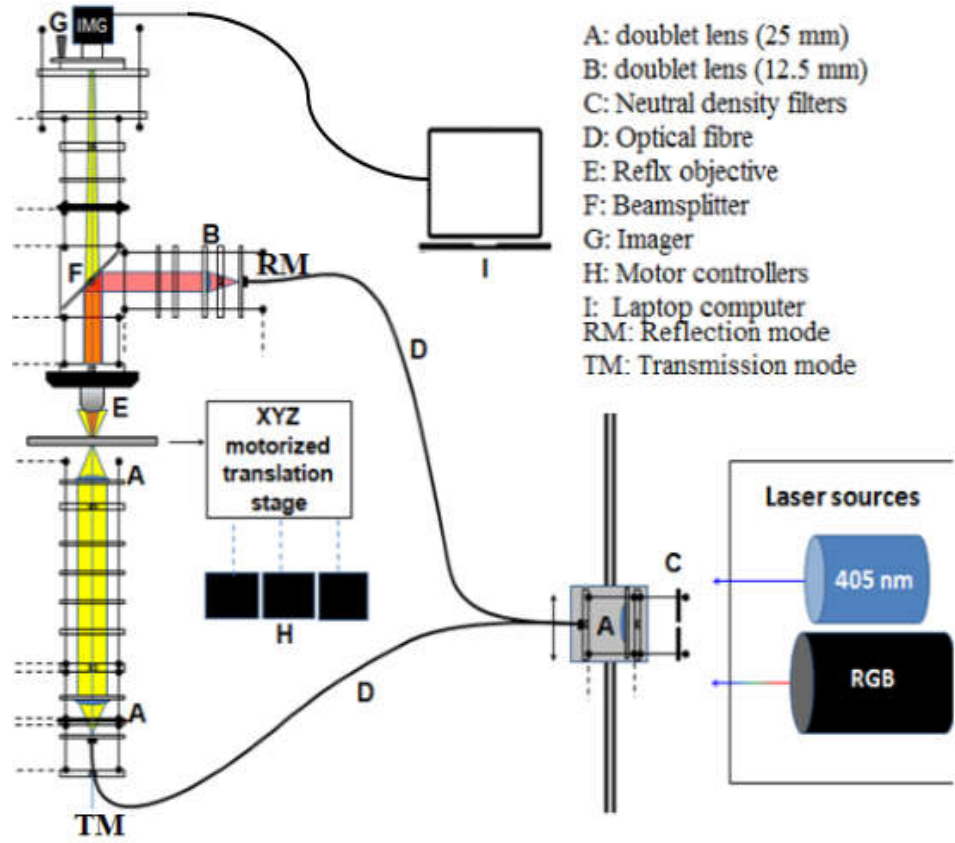
Figure 9: A schematic diagram of the multi-functional imaging microscope (MFIM) showing two illumination laser sources in: reflection mode (RM) and transmission mode (TM).

Two (2) diode lasers were used as illumination light sources. One of the lasers, 405 nm diode laser, operates on 12 V DC input voltage, 400 mA current, 500 mW output power and TTL 0-20 kHz, 5 V output frequency, voltage respectively. The other diode laser, a red (R), green (G) and blue (B) (RGB) colours laser illuminates at 650 nm (R), 532 nm (G) and 450 nm (B). This laser operates on 12 V DC and less than 1 A input voltage and current respectively. At the output, it provides 400 mA output current, TTL 0-20 kHz output frequency and 5 V output voltage. The 2 diode lasers were mounted into a breadboard and a wheel, containing the ND filters with varied optical

85

densities (ODs) was also placed into the breadboard in line with the lasing path.

The breadboard is 4 x 6 x 0.5 inches aluminum breadboard. This breadboard is a nonmagnetic base plate which provided a convenient and cost-effective platform for optical assembling, conducting the experiments, and mounting of small sub-systems. It contains minimally reflective anodized coating and is through-drilled with a standard 25 mm metric hole pattern offset 12.5 mm, from the edges of the board. The holes are threaded completely through the breadboard, allowing the components to be mounted easily and precisely.

The ND filters in a wheel with ODs 0 (100 % transmission), 0.2 (75 % transmission), 0.3 (50 % transmission), 0.6 (25 % transmission), 1.0 (10 % transmission) and 2.0 (1 % transmission), were used to attenuate the power of the laser. This circular, 30 cage plate-mounted, with continuously variable ND filters provide linear, adjustable attenuation within the coated region via rotation. The ND filters are composed of sheets of quartz coated with a metal. They are UV fused silica glass substrate and a metallic inconel coating through a full 270°, ensuring a flat spectral response from the UV to the mid-infrared.

Five ADLs were mounted into lens holders and used as collimating lenses. The five ADLs were in two categories of different focal lengths and diameters. The first category, four ADLs, has 60 mm focal length and 25 mm diameter whilst the second category, one ADL, has 30 mm focal length and 12.5 mm diameter. One each (two in all) of the ADLs with 60 mm focal length and 25 mm diameter was used to collimate the laser beams from the 405 nm

86

and the RGB lasers into two optical fibres for coupling. Another one each (two in all) 60 mm focal length and 25 mm diameter ADL was also used to collimate the laser beams onto the sample plane in TM. In RM, one ADL with 30 mm focal length and 12.5 mm diameter was used to collimate the laser beams onto the sample plane.

At the lasing points in TM and RM, there are two optical diffusers placed at common point of the optical axes of the fibre pots. The function of the diffusers was to aid in homogeneous illumination and to reduce speckle effect. The reason for using the diffuser was to achieve Lambertian distribution of light from the lasers. Another 25 mm lens was mounted at the fibre end to collimate the laser onto the SS.

Motorized XYZ translators with controllers were mounted and linked to a computer. The XYZ translators have 25 mm travel range, 2.4 mm/s maximum velocity, 0.05 μm minimum achievable incremental movement, 1.6 μm bidirectional repeatability and less than 6 μm backlash. These translation stages provide electronically controlled linear travel along a well-defined axis. The moving platform contains holes for alignment pins that ensure orthogonality when the stage is stacked with other stages or connected to accessories. Horizontal loads of 12 kg and vertical loads of 4.5 kg are supported by the 67:1 planetary gear head. A built-in Hall Effect encoder provides a resolution of 29 nm.

The translation mechanism, based upon a dual set of linear rails with continuously recirculating ball bearings, provides smooth, low-friction movement. Built-in limit switches prevent travel outside of the intended range, regardless of the control interface being used. The Reflx objective was

87

mounted onto the XYZ translators. The imager was also mounted along the optical axis of the sample plane. The cube motor controllers provided control for a single axis with a computer via a universal serial bus (USB) cable. It is bundled with software, which supplies out-of-the-box stage control from the computer and enables support for common programming interfaces. The beam splitter (BS) was mounted in between the SS and the imager. The signals from the imager and the switching-on of the diode lasers were controlled through the computer and the DAQ via MATrix LABoratory (Matlab) algorithm (R2014a Matlab 8.3.0.532, Mathworks Inc.). Plate 1 shows a photograph of the MFIM set- up.
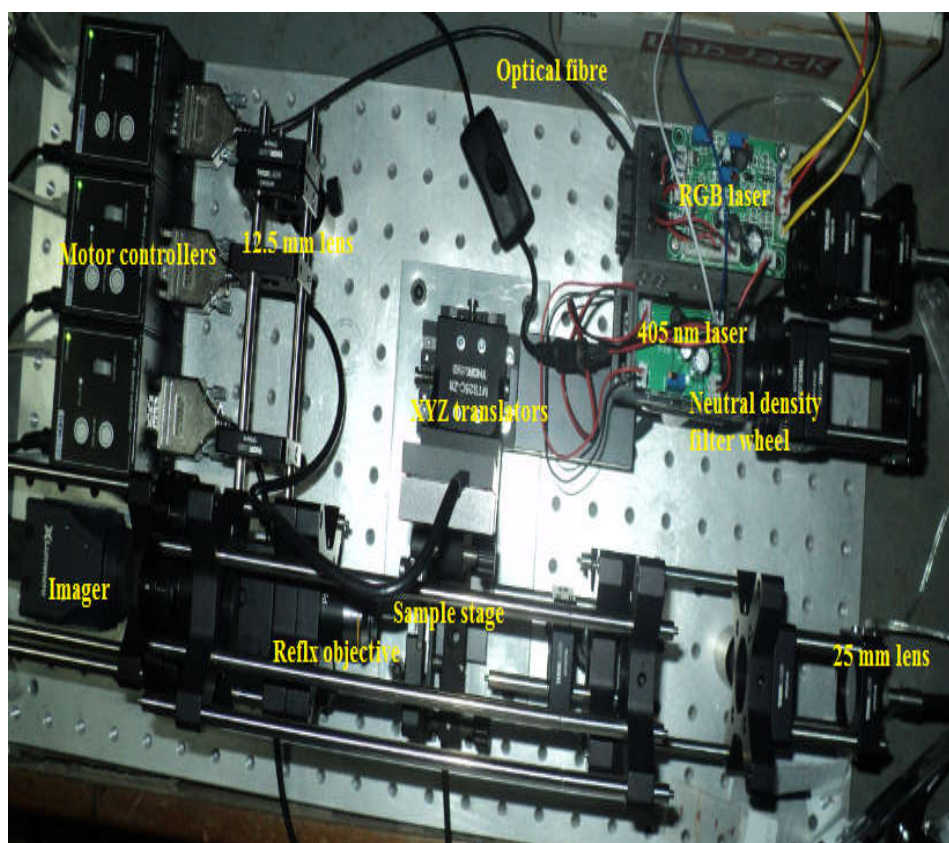
Plate 1: A photograph of the multi-functional imaging microscope (MFIM).

Blood Sample Collection and Preparation

Ethical Approval and Volunteers Informed Consent

Blood samples and volunteer's data collection procedures were approved by Ghana Health Service Ethical Review Committee (GHS-ERC-09/05/14). A copy of this approval is shown in Appendix I. Approval was also sought from the administrators of selected health facilities before sample collection. The purpose of the study, procedures involved and possible risks associated with this study were explained to the prospective volunteers in comprehensible language after which they were given the chance to ask questions. After ensuring that inclusion criteria are met, written informed consent of the volunteers, or parents, or guardians or representatives were sought before blood samples were collected from them. To ensure anonymity of the study subjects, the samples were labeled using initials of the names of a specific health facility where blood collection was being done as well as order of arrival of the volunteers.

The volunteers eligible for blood sample collection included patients who were 6 months old or older, weighed more than 5 kg and suffering from uncomplicated malaria. Those excluded were volunteers who were unconscious, hemophilic, experiencing palpitation at the time of sample collection, have had blood transfusion within the previous 48 hours and suffering from complicated malaria. Palpitation in young children was determined by the same experienced phlebotomist. The blood samples collected from the volunteers were handled solely by an experienced phlebotomist. The study posed no risk to volunteers except for the transient pain that were felt during blood collection. Sterile techniques, disposable and

89

single-use materials were used at all times to avoid any infection. The study will not bring any direct benefits to the volunteers. However, volunteers may benefit indirectly from the results of the study, after it has been shared with the Ghana Health Service.

Study Sites

Blood samples were collected from the Central Region of Ghana. The Central region occupies an area of 9826 km^2 with estimated population of two million one hundred and seven thousand two hundred and nine (2,107,209) and intercensal growth rate of 2.7% (National Population Census, 2010). The region is bordered by Ashanti, Eastern, Greater Accra, Western region and the Atlantic Ocean. The region is one of the most densely populated regions in Ghana with a population density of 214 people per square kilometre (National Population Census, 2010). The region has two ecological zones; forest zone and coastal savannah zone. For the purpose of this study, four hospitals in four study sites in the forest and the coastal savannah zones were selected. Each zone was made up of two study sites.

The hospitals comprising the study sites in the forest zone were Twifo-Praso District Hospital in Twifo-Praso and St. Francis Xavier Hospital in Assin Foso. That of the coastal savannah zone was made up Cape Coast Teaching Hospital and University of Cape Coast Hospital, all in Cape Coast.

The coastal savannah zones are characterized by undulating plains with isolated hills and occasional cliffs with sandy beaches and mursh areas. The vegetation around the places can be classified as savannah with grassland and few trees. The forest zone lies between 250 m to 300 m above sea level. It is

90

characterized by dense forest vegetation with palm and cocoa plantations.

Study Size/ Study Population Estimation

Three hundred and sixty (360) volunteers, comprising ninety (90) volunteers from the four study sites were involved in this study. The sample size was estimated using the method as described by (Fischer et al., 1998; Chavchich, et al., 2010; Eastman et al., 2011). The sample size determination procedure is presented in Appendix II. The samples were taken from both males and females. The ages range from 1-90 years with the mean age of 16 years.

Five millilitres (5 ml) of blood samples was collected by the phlebotomist from the 360 volunteers who were tested positive for malaria parasites, infected blood (*i*-blood). The volunteers were pleaded to and were told to return after completing antimalaria treatment regimen. In order to ensure that the volunteers return and also to compensate for the blood lost in them, they were given two (2) tins of milk each and also their transportation fare was paid. With these motivations, all the 360 volunteers returned. On their return and having tested negative, uninfected blood (*u*-blood), another 5 ml of blood sample was collected from each of the volunteers. Thus, a total of seven hundred and twenty (720) blood samples consisting of 360 *i*-blood and 360 *u*-blood samples were collected from the volunteers. The blood samples were collected in test tubes containing ethylenediamine tetraacetic acid (EDTA) as an anticoagulant and transported in an ice chest filled with ice packs.

91

Haemoglobin (Hb) content and hematocrit value in each *i*-blood and *u*-blood samples for the male and female volunteers were respectively 16 g/dl with 45 % hematocrit, and 14 g/dl with 40 % hematocrit. These were determined by an experienced haematologist at the laboratory of Department of Biomedical and Forensic Sciences, School of Biological Sciences, University of Cape Coast.

The *i*-blood samples were grouped by a pathologist into two main groups: level of infection (parasite density) and intraerythrocytic life cycle stages (ring, trophozoite and schizont). The level of infection was based on four categories (+, ++, +++, ++++) by counting the number of parasites per high power field (HPF). That is, 1-10 parasites per HPF (+), 11-100 parasites per HPF (++), 1-10 parasites per each HPF (+++) and >10 parasites per each HPF (++++).

Thin blood smear slides, consisting of three (3) stained and five (5) unstained, were prepared from each *i*-blood sample for imaging. Another set: two (2) each of stained and unstained blood smear slides were prepared from the *u*-blood samples. In all, four thousand three hundred and twenty (4320) thin blood smear slides were prepared from all the blood samples from the 360 volunteers. This comprises of one thousand and eighty (1080) stained and one thousand eight hundred (1800) unstained for *i*-blood samples; seven hundred and twenty (720) each of stained and unstained for *u*-blood samples. The stained sets slides were prepared by fixing in ethanol and stained with Giemsa.

The stained sets were used as training slides and unstained set as test slides. These slides were prepared by an expert laboratory technician. In preparing the slides, two drops (0.1 ml) of the blood samples were placed on

92

sterile microscope slide and carefully spreading it with another slide at an angle 45°. To avoid contamination in each blood, different slides were used for spreading. The remaining blood samples were used for fluorescence excitation spectra data acquisitions and blood absorption bands with their corresponding optical density determinations.

Experimental Methods and Procedure

Fluorescence Excitation Spectral Acquisitions

Fluorescence spectra of the *u*-blood and the *i*-blood samples were recorded using a diode laser source with 30 μW power, and excitation wavelength of 405 nm (O-Like). Figure 10 shows a schematic diagram of the set-up used for fluorescence spectra data acquisitions.

A: 405 nm excitation laser source
B: Neutral density filter
C: System unit providing power to laser
D: Quartz cuvette
E: Blood sample
F: Sample holder support
G: Excitation
H: Microscope objective
I: 405 nm long pass filter
J: Fibre port
K: Optical fibre
L: Laptop computer
M: USB 4000 spectrometer
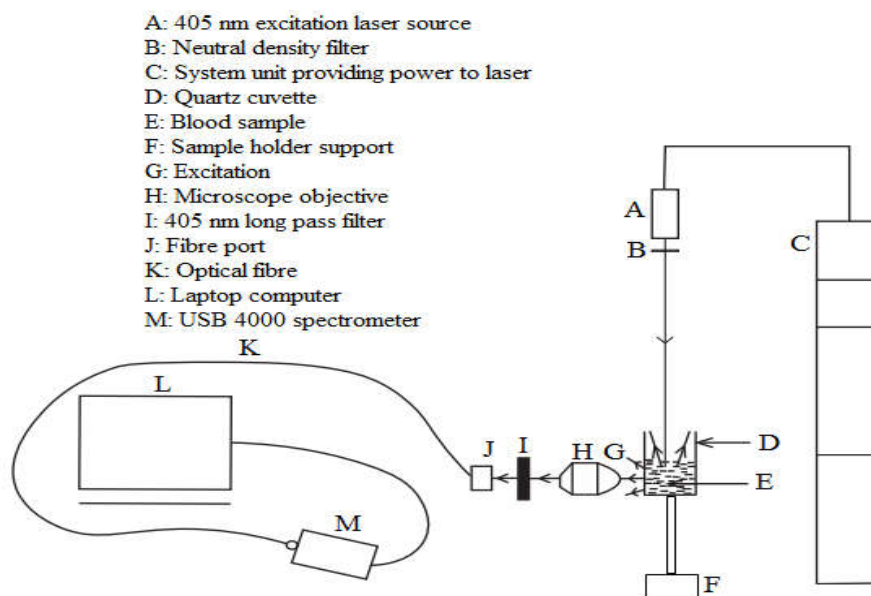
Figure 10: Schematic diagram of experimental set-up for acquiring fluorescence spectra data from blood samples.

Two millilitres (2 ml) of the *u*-blood sample of a volunteer was put into a 3 ml quartz cuvette (Hellma, 104F-QS). The 405 nm laser light was switched on and the output power was attenuated using a neutral density (ND) filter (Thorlabs Inc., NE10A) with 10 % transmission. The transmitted light illuminated the *u*-blood sample and the scattered light was collected into a microscope objective (Melles Griot) through a perpendicular configuration with the excitation light source. The microscope objective has x10 magnification and 0.25 numerical aperture (NA). The excitation wavelength contained in the collected light was cut off via a 405 nm long-pass filter (LPF) (Edmunds Optics, GG-420). This allowed only fluorescence light to transmit through the LPF. The LPF was used to compensate for the less than ideal behaviour of light detection and also to achieve maximum sensitivity of spectral response. The fluorescence scattered light was fibre-coupled via the optical fibre to a UV-VIS USB 4000 spectrometer (Ocean Optics Inc.) connected to a Toshiba Laptop (3.0 GHz 8.0 GB, AMD A10-4600M) installed with *SpectraSuit* software (Ocean Optics Inc.) for data acquisition. Plate 2 shows a photograph of the set-up used for fluorescence spectra data acquisition.

Plate 2: A photograph showing the components of the set-up for acquiring fluorescence spectra data.

One thousand four hundred and twenty (1420) spectra data were acquired. These fluorescence spectra data were recorded at room temperature in an enclosed laboratory within 120 seconds. To ensure that partial oxygen (pO_2) was maintained throughout the spectra data acquisitions, the blood samples preparations and the spectra data acquisitions were done under the same conditions. Photo bleaching was avoided by repeating the experiment three times for an optimal duration of 120 seconds and observing no inter-replicate spectral differences. 2 ml of the i-blood sample of the same volunteer was put into the 3 ml quartz cuvette and the fluorescence excitation spectral

95

procedure was repeated for acquiring 1420 spectra data for this *i*-blood sample. Similar procedure was followed for acquiring spectra data for each *u*-blood and *i*-blood samples of all the remaining volunteers.

Blood Absorption Bands and Optical Density Determinations

Twelve microlitres (12 μl) each, of the remaining *u*-blood and *i*-blood was used for blood absorption bands and optical densities (ODs) determinations with the aid of a Shimadzu UVmini-1240 UV-VIS spectrophotometer (Shimadzu Corporation, Kyoto, Japan). 2.5 ml of a Drabkin's solution was measured with a milli-pipette and transferred into the 3 ml quartz cuvette. The Drabkin's solution was used for quantitative determination of Hb concentration in the whole blood samples. This solution was prepared from a mixture of distilled water, sodium bicarbonate, potassium ferricyanide, and potassium cyanide.

The UV-VIS spectrophotometer was switched on and blank correction was done with the 2.5 ml Drabkin's solution and reference ODs data were acquired by placing the cuvette into the sample chamber and scanning through the spectrophotometer spectral band by spectral band in the intervals of 5 nm within the spectral bands range of 300-800 nm. This was because the UV-VIS spectrophotometer was limited to point-by-point data acquisitions. After that, the Drabkin's solution was disposed off and the quartz cuvette was well washed with distilled water twice and dried.

Twelve mircolitres of *u*-blood sample of a volunteer was measured with a micro-pipette and poured into a test tube. In the test tube, the *u*-blood was diluted with 2.5 ml of Drabkin's solution and shaken continuously. The

96

diluted *u*-blood sample was then transferred quickly into the quartz cuvette and inserted into the sample chamber. Blood absorption bands and their corresponding ODs data were acquired for the *u*-blood sample by scanning through the spectrophotometer spectral band by spectral band at the same 5 nm intervals within the same spectral range. The same procedure was repeated for the *i*-blood sample of the same volunteer, and the remaining *u*-blood and *i*-blood samples of all the other volunteers. Left over samples were stored in a refrigerator at 4 ^{o}C. The storage will continue for a period of two years after the research, within which the samples may be used for further studies upon approval by the Ghana Health Service Ethical Review Committee. After the above period, the left over blood samples will be autoclaved at 121 ^{o}C for 15 minutes and then it will be disposed of by burning in an incinerator.

Spectral Image Acquisitions

Spectral images of the training and test sets slides were acquired in reflection, scattering and transmission modes, using multispectral light emitting diode imaging (MSLEDI) microscope. The MSLEDI microscope, a detailed description presented elsewhere (Opoku-Ansah, 2012), is housed at the Laser and Fibre Optics Centre (LAFOC), Department of Physics, School of Physical Sciences, College of Agriculture and Natural Sciences, University of Cape Coast, Cape Coast, Ghana. This MSLEDI microscope utilizes nine (9) LEDs in each mode, emitting a total of thirteen (13) spectral bands ranging from UV to near infrared (NIR). The spectral bands are 375 nm, 400 nm, 435 nm, 470 nm, 525 nm and 590 nm. The rest are 625 nm, 660 nm, 700 nm, 750 nm, 810 nm, 850 nm and 940 nm.

The MSLEDI microscope consists of mechanical, optical and optoelectronic components. The mechanical components are LED holders and a brass tube. The optical components are fibre ring, the Reflx objective, the BS, the optical diffuser and LEDs. Finally, the components making up of the optoelectronic part are the imager, the DAQ, current driver, multiplexer, LED battery and stripboard. There is also a laptop computer for controlling the signals from the camera and the DAQ. Plate 3 shows a photograph of the set-up of the MSLEDI microscope showing the components and the geometry of the LED light sources.
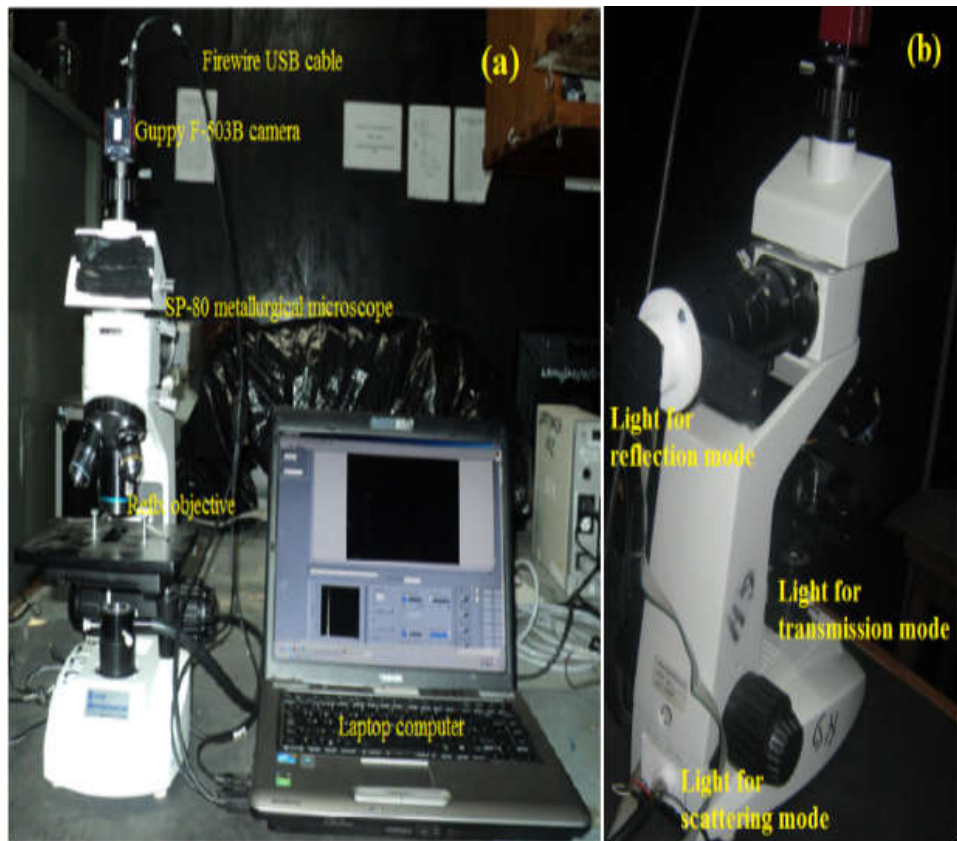
Plate 3: A photograph of the set-up of multispectral light emitting diode (LED) imaging (MSLEDI) microscope. (a) Various components and (b) LED light sources showing reflection, scattering and transmission modes (Opoku-Ansah, 2012).

In acquiring the multispectral images, the power supply to the MSLEDI microscope was checked with a multimeter to ensure that there was 9 V being supplied to the microscope and then plugged into the power source. Universal serial buses (USBs) from the imager and the DAQ were plugged into their respective USB ports on the computer. The power supply and the computer were then switched on, and a developed *Labview* program, launched. In the program, the LED *current icon* was set to maximum and '0' was selected from the *video mode* icon. One of the training set slides prepared

99

from *i*-blood sample of a volunteer was placed on the sample stage (SS). This slide contains uninfected red blood cells (*u*-RBCs) and *P.falciparum* RBCs (*i*-RBCs). After placing the slide on the SS, reflection mode was selected from the *geometry icon*.

In reflection mode, light from 590 nm LED source was selected from the LED icon for focusing. The required gain and exposure time were set from the *gain* and *exposure time* icons. The fine and coarse adjustment knobs were used interchangeably in order to focus the image. After the image has been focused, image name was given from the *image base name* icon. The other LED sources were selected one after the other, adding one at a time by selecting *add line* icon. The *master delay time* was set at 10 000 μs. This was because the acquisition time of the camera required was 10 ms and the *Labview* program operates in micro-seconds.

For reflection imaging, light from the LED sources was incidence on the BS from which half the light reflected towards the slide on the SS and the other half transmitted. The reflected light then moves through the Reflx objective, illuminated on the slide on the SS and backscattered. The backscattered light was collected again through the Reflx towards the BS. At the incidence of the BS, half of the backscattered light containing the image signal reflected towards the light source whilst the other half transmitted through the BS. This transmitted light was brought onto focus by a convex lens towards the imager for an image to be acquired. Image name was saved into a folder by selecting *write to file* icon. Images at the 13 spectral bands were acquired via the computer and saved into *tagged image file format* (TIFF) by selecting the *start run mode* icon, a window pops up and current

folder selected. Each image has a pixel size of 2.2 × 2.2 μm. The *geometry icon* was then changed to scattering mode.

The LED sources were again selected one after the other, adding one at a time by selecting *add line* icon. Light from the LED sources in scattering mode was scattered by the optical diffuser and brought onto focus by a convex lens. The focused light illuminated the slide on SS and transmitted through it. The transmitted light was collected and focused by the Reflx objective towards the imager for image signals to be detected. Images at the 13 spectral bands were also captured by the imager via the computer. The procedure for acquiring images from the slide in transmission mode was followed as described elsewhere (Opoku-Ansah, 2012).

In all the three (3) modes, thirty nine (39) images were captured for this training test slide. The same process was followed for capturing images of the training set slide prepared from the *u*-blood sample of the same volunteer. The described procedures, in all the three modes, were repeated for acquiring images from the rest of the training set and the entire test set slides of the blood samples of all the volunteers. For each of the training set slides and test set slides, four hundred and sixty eight (468) images were acquired, comprising of three hundred and twelve (312) of *i*-blood and one hundred and fifty six (156) *u*-blood samples. In all, one hundred and sixty eight thousand, four hundred and eighty (168480) images were acquired from the *i*-blood and *u*-blood samples of all the volunteers.

System Testing: Fluorescence Image Acquisition

Fluorescence images of the training set and test set slides containing *u*-RBCs and *i*-RBCs were acquired using the assembled multi-functional imaging microscope (MFIM) in RM. A training set slide was placed on the sample holder and the power supply to the lasers was switched on. The computer was then switched on through which the 405 nm was turned on using a developed Matlab code. The wheel containing the ND filters was rotated and 2.0 OD was selected to ensure that 1 % of the light was being coupled into the fibre to prevent photobleaching.

The light collimated by the 25 mm lens and coupled through the fibre was evenly distributed by the optical diffuser and then collimated again by the 12.5 mm lens. The light then hits the BS through which 50 % of the light reflected and was collected through the Reflx objective. The other 50 % of the light is transmitted through the BS. The collected light illuminated the sample and backscattered. The backscattered light was again collected through the Reflx objective and hits the BS. 50 % of the collected light reflected back to the source plane. The other 50 % with the excitation source transmitted through the BS and was cut off with 405 nm LPF for the fluorescence image signal to be detected by the imager. Image showing the *u*-RBCs and the *i*-RBCs was then viewed via the computer. After ensuring that fine focusing was achieved by adjusting the XYZ translators interchangeably using the motor controllers, fluorescence images were captured by the imager controlled through the developed Matlab code via the computer. The image was then saved into a folder. The same procedure was repeated for the remaining training set slides and the entire test set slides.

To characterize the *u*-RBCs and the *i*-RBCs, the fluorescence spectra data, the ODs data, the images obtained from the microscopes, thus, MSLEDI and MFIM, were imported into Matlab platform and other application softwares from the folders in which they were saved for further Analysis. Analyses such as spectral, statistical and geometrical characteristics, as well as multivariate analysis were done with the aid of Matlab. Attributes based on eccentricity or aspect ratio (major axis over minor axis) and integrated optical density (IOD) (average intensity over density) were retrieved from the *u*-RBCs and the *i*-RBCs using *Image Pro Plus 5.0* software (Media Cybernetics, USA), version 3.1 for windows 3.0. The *Image Pro* is dynamically linked to Microsoft's Excel to aid easy graphical representation of data. This was done using the dynamic data exchange (DDE) provided in the file menu of the data window.

103

CHAPTER FOUR

RESULTS, ANALYSIS AND DISCUSSIONS

Results, analysis and discussions on the applied experimental techniques are presented in this chapter. The information is divided into five parts. The first part reports on the categories of volunteers used in this research, the second part analyzes and discusses the results on fluorescence excitation on samples and the third part represents results, analysis and discussions on optical density determinations from spectrophotometry technique. The fourth part presents results, analysis and discussions on spectral images acquired using the multispectral light emitting diode (LED) imaging microscope (MSLEDI) and the final part analyzes and discusses the results on the fluorescence images captured from the multi-functional imaging microscope (MFIM).

Volunteers Information

Table 1 provides range of ages and corresponding categories of the number of volunteers used in this research work. The table provides information about two categories of volunteers totaling 360. They are males and females.

104

Table 1

Description of the range of ages and corresponding categories of the number of volunteers.

Age (years)	No. of male volunteers	No. of female volunteers	Sum
0-10	36	48	84
11-20	20	28	48
21-30	18	27	45
31-40	17	20	37
41-50	20	19	39
51-60	18	17	35
61-70	16	17	33
71-80	15	17	32
81-90	2	5	7
			Total = 360

It can be observed from Table 1 that, out of the 360 volunteers who were susceptible to *Plasmodium falciparum* (*P.falciparum*) infections, the males contributed 45 % and the females accounted for the remaining 55 %. Table 1 also shows that *P.falciparum* infections vulnerability in the volunteers was high in the youngest age group (1-10 years), 22.2 % and 24.2 % and low in the oldest age group (81-90 years), 1.2 % and 2.6 %, for males and females respectively. This confirms Amexo et al. (2004) report on malaria vulnerability group.

Fluorescence Spectral Processing

The 1420 fluorescence spectra data for each of the uninfected blood (*u*-blood) and the *P.falciparum* infected blood (*i*-blood) samples for all the volunteers was imported into Matlab platform via a developed Matlab code. In the Matlab platform, mean spectra of each 1420 fluorescence spectra data of the *u*-blood and the *i*-blood samples for all the volunteers was determined for further analysis. The mean spectra determination for the *i*-blood ((+), (++), (+++) and (++++)) samples was based on the levels of infection, that is, parasite densities (PDs). The determined mean fluorescence spectra for the PDs was plotted and in the plot, peak wavelengths were located for each spectra representing the different PDs. A layout of the Matlab code for mean spectra determinations and peak wavelengths locations of the 1420 fluorescence data for each *u*-blood and *i*-blood samples is shown in Figure 11.

```
load fluorescence data (X)
            |
            v
   find mean spectra (X̄)
            |
            v
        plot X̄
            |
            v
find peak wavelength of X̄
```
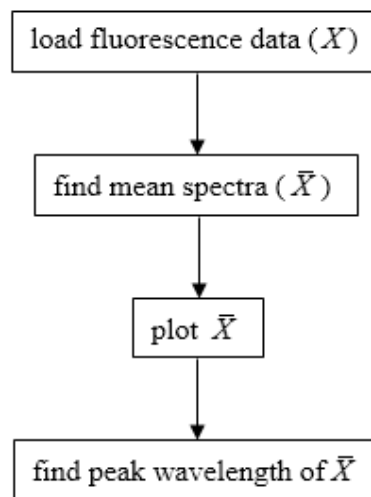
Figure 11: A layout of Matlab code for mean spectra determination and peak wavelengths location of fluorescence data of uninfected (*u*-blood) and *Plasmodium falciparum* infected (*i*-blood) samples.

106

Figures 12-15(a and b) show normalized mean fluorescence spectra and a zoom of the peak wavelength of each *u*-blood and *i*-blood samples with different parasite densities (PDs). The displayed fluorescence spectra representing the *u*-blood and the *i*-blood samples reveal changes in the fluorescence intensity and spectral shape. Sample *t*-Test, with 2048 degrees of freedom and 0.05 significant levels, done on the mean spectra showed variations in the peak wavelengths. A standard error of mean intensity was used to determine the range of values in which the true population means was likely to fall. The standard errors were calculated as *u*-blood 0.061, *i*-blood (+) 0.039, *i*-blood (++) 0.044, *i*-blood (+++) 0.033 and *i*-blood (++++) 0.041.

Figures 12-15(a and b) shows fluorescence spectra signature of whole blood and according to the work done by Gao et al., the fluorescence spectra signature of whole blood is within the range of 500-700 nm (Gao et al., 2004). It can be observed from Figure 12-15(a and b) that, fluorescence intensities are high in *u*-blood samples, with more haemoglobin (Hb) than in *i*-blood samples, within which Hb decreases with increasing PDs. This is as a result of the parasite feeding for nutrient in the *i*-blood samples. The observed high fluorescence intensities in the *u*-blood samples shows that within the *u*-blood samples, hematocrit (percentage of RBCs in the blood volume) values and Hb content are high and this stimulated the increased fluorescence intensities. The low intensities observed in the *i*-blood samples demonstrate the effect of low hematocrit values, low Hb content and/or fluorescence quenching due to environmental changes resulting from the presence of *P. falciparum* parasites in the *i*-blood. Also, the decreasing intensities of the *i*-blood samples as the

107

Figure 12: Normalized mean fluorescence spectra of uninfected blood (*u*-blood) and *Plasmodium falciparum* infected blood (*i*-blood) samples with (+) parasite density at excitation laser source wavelength ($\lambda = 405$ nm); (a) original mean spectra and (b) zoomed spectra of (a).

Figure 13: Normalized mean fluorescence spectra of uninfected blood (*u*-blood) and *Plasmodium falciparum* infected blood (*i*-blood) samples with (++) parasite density at excitation laser source wavelength ($\lambda = 405$ nm); (a) original mean spectra and (b) zoomed spectra of (a).
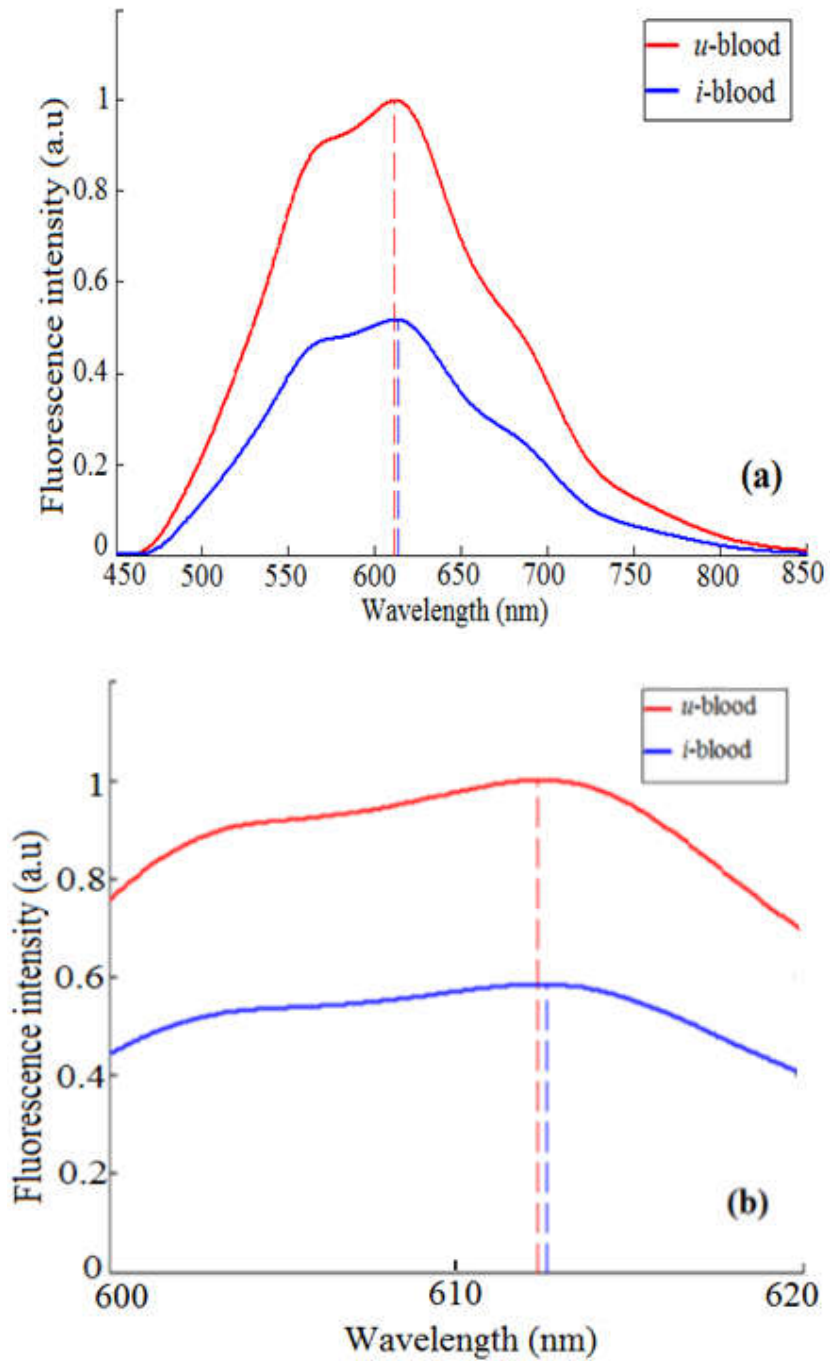
Figure 14: Normalized mean fluorescence spectra of uninfected blood
(*u*-blood) and *Plasmodium falciparum* infected blood (*i*-blood)
samples with (+++) parasite density at excitation laser source
wavelength ($\lambda = 405$ nm); (a) original mean spectra and (b)
zoomed spectra of (a).

110
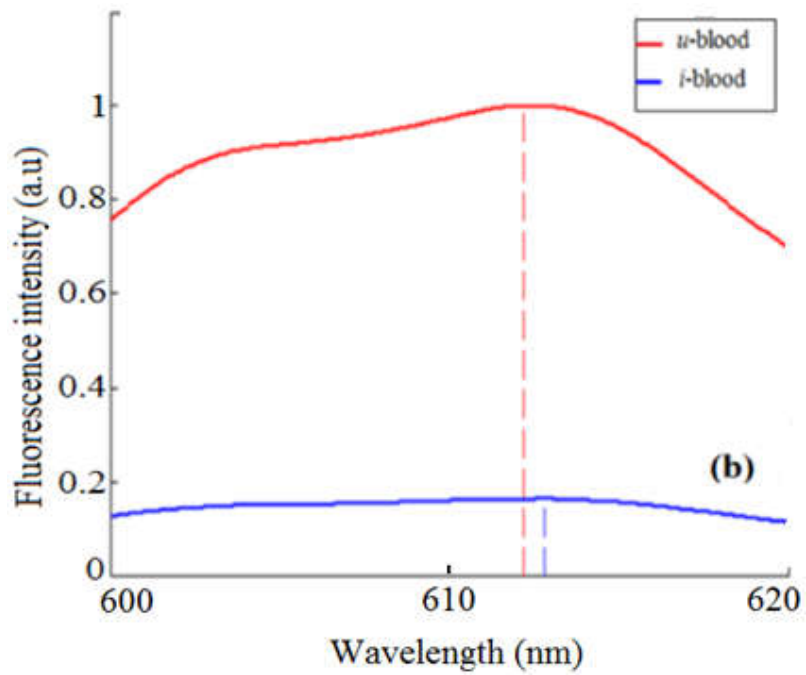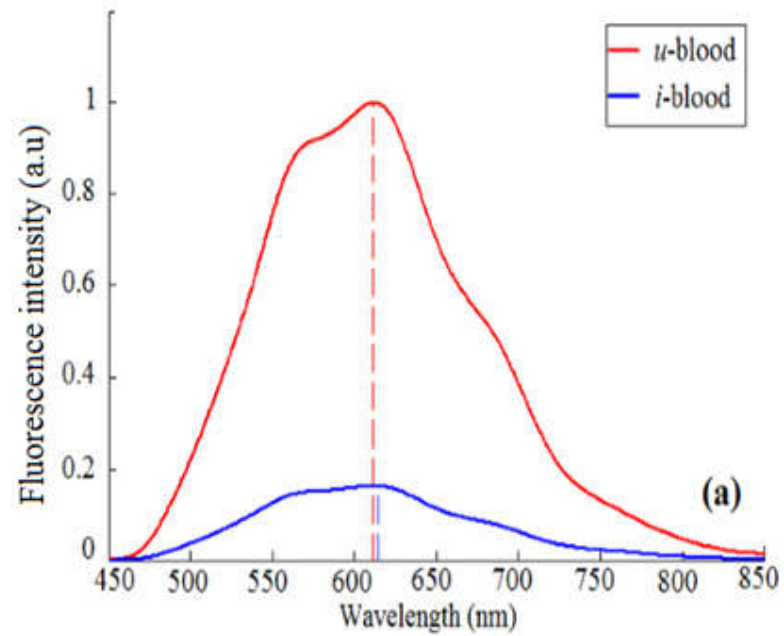
Figure 15: Normalized mean fluorescence spectra of uninfected blood
(*u*-blood) and *Plasmodium falciparum* infected blood (*i*-blood)
samples with (++++) parasite density at excitation laser source
wavelength ($\lambda = 405$ nm); (a) original mean spectra and (b)
zoomed spectra of (a).

PDs increase show that fluorescence quenching increases as the PDs increase in the *i*-blood.

It can also be seen from Figures 12-15(b) that when the *i*-blood samples with different PDs was excited by the same light source, peak wavelengths of fluorescence spectra appears red-shifted with increasing PDs. This red-shifted phenomenon of fluorescence spectra peak wavelengths with increasing PDs in the *i*-blood samples could be due to difference in blood absorption by the fluorophores in the *i*-blood samples. Energy transfer between inhomogeneous fluorophores in the *i*-blood samples with different PDs triggered the blood absorption by ground state molecules in the *i*-blood samples. Increment of PDs in the *i*-blood samples increases self-absorption phenomenon. The higher the PDs in the *i*-blood samples, the weaker the absorbed energy and the fluorescence peaks are shifted to longer wavelength. Again, the red-shifts of the spectra as the PDs increases reveal the excited electrons transfer energy to the PDs. And, the more the PDs, the higher the energy transfer, and further the red-shift. These observations indicate that there is a possibility of estimating PDs in the *i*-blood samples using the fluorescence spectra peaks.

As a way of examining the disparities in the fluorescence intensities, the mean spectra of the *u*-blood and the *i*-blood samples were plotted together and the results are presented in Figure 16. This figure shows that the mean fluorescence spectrum of the *u*-blood samples is high in intensity and broader in width than the *i*-blood samples.
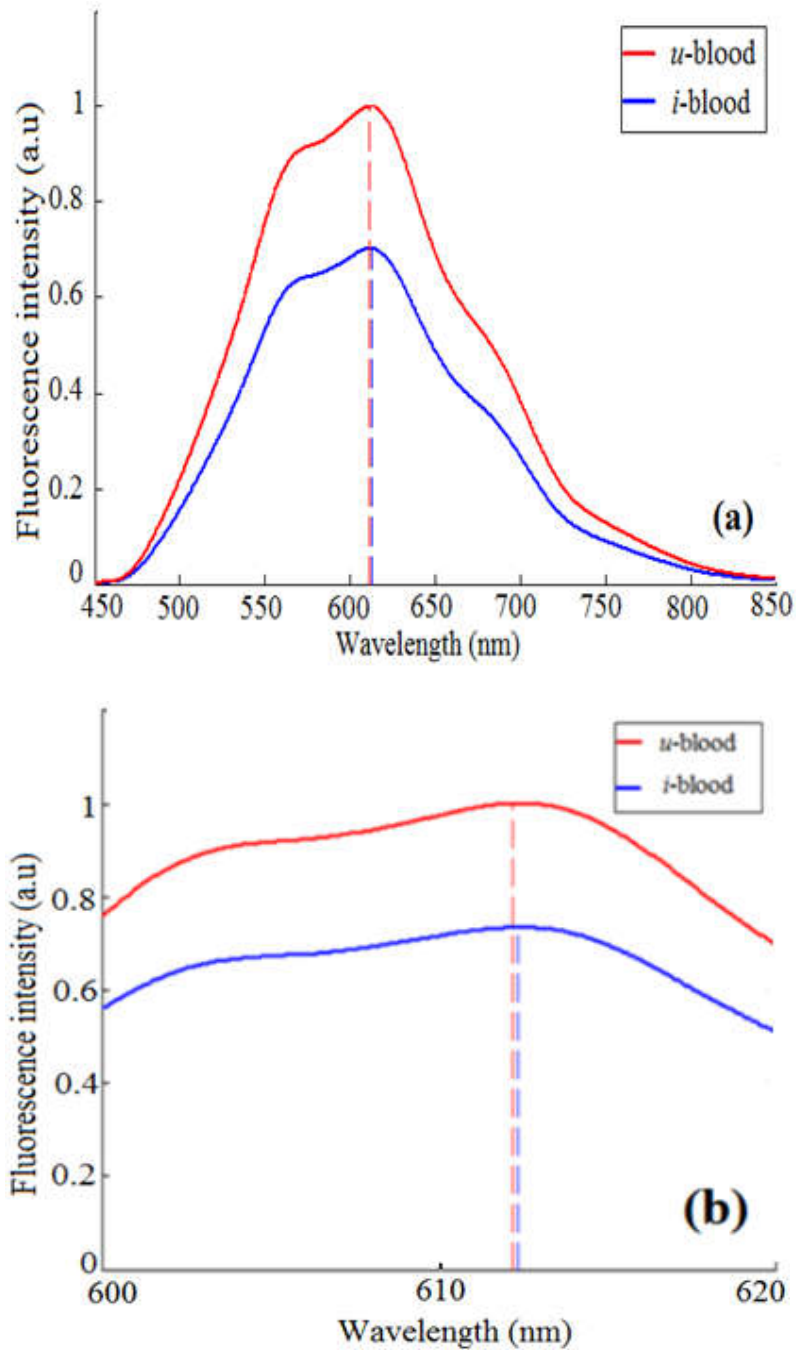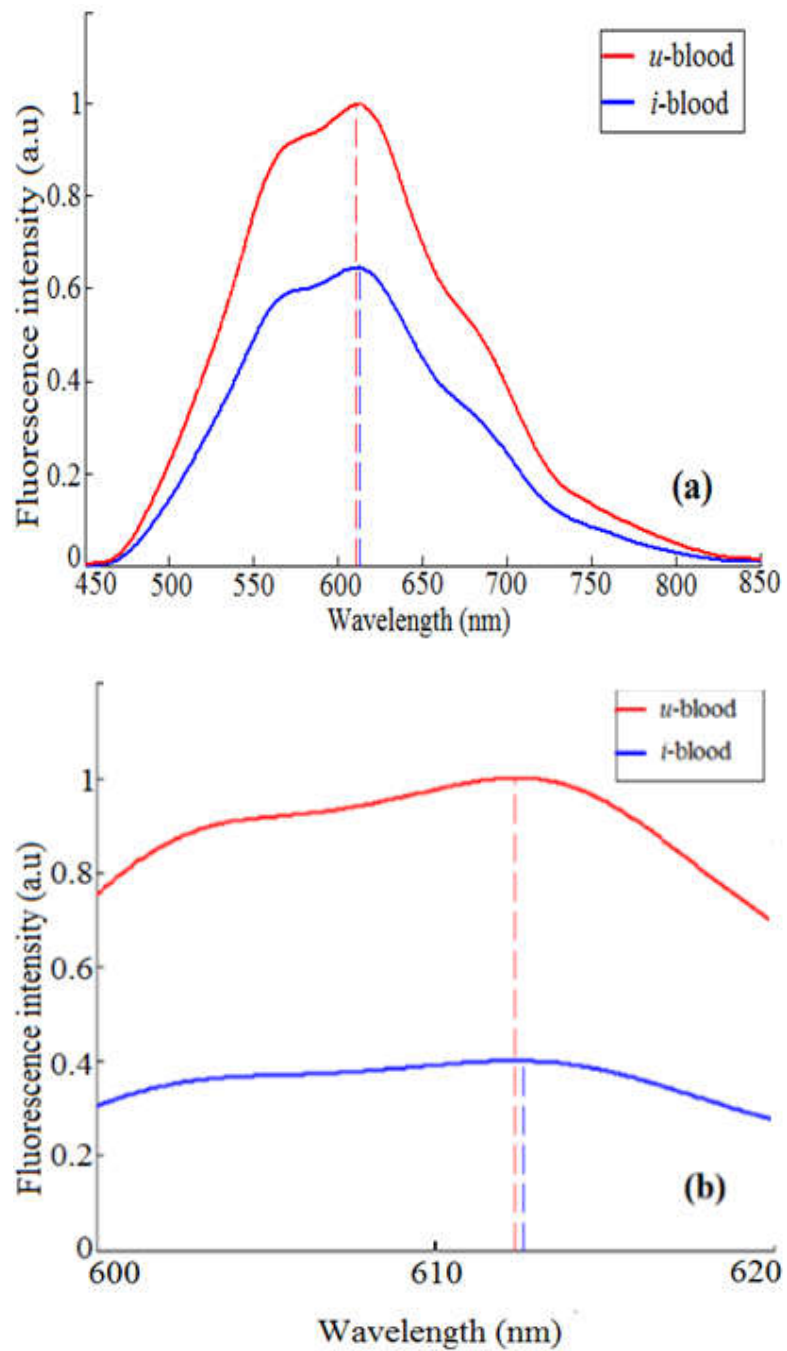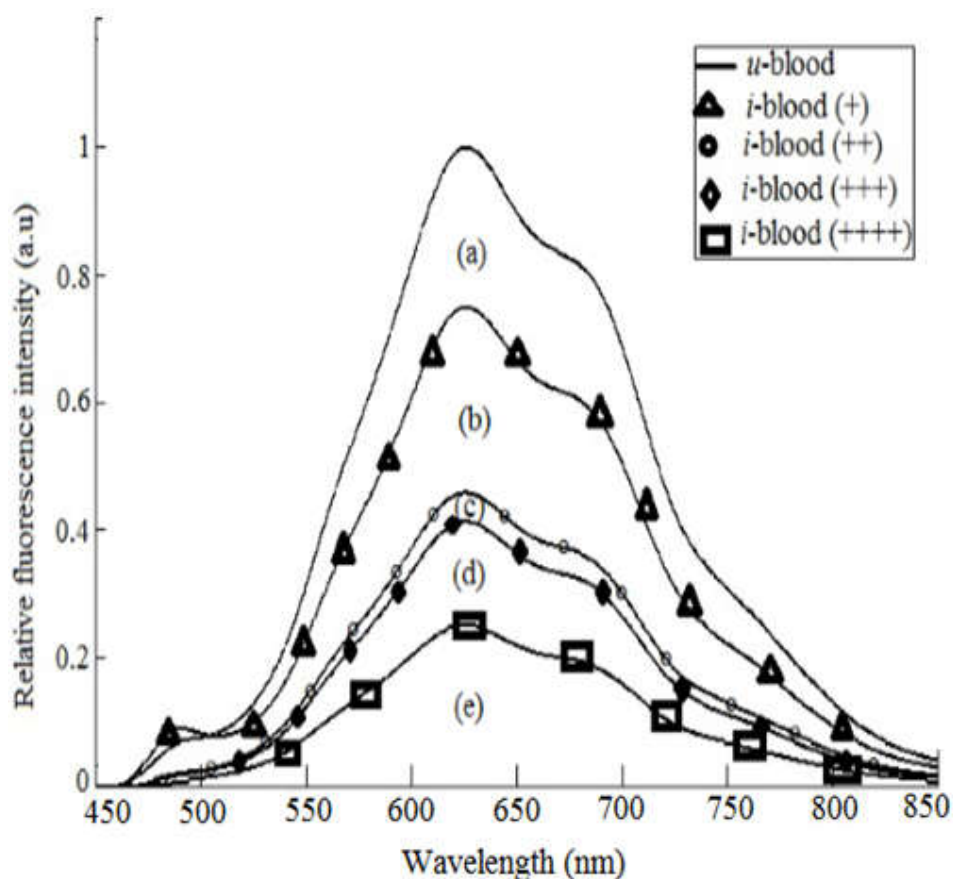
Figure 16: Normalized mean fluorescence spectra of uninfected blood (*u*-blood) sample (a), and *Plasmodium falciparum* infected blood (*i*-blood) samples with parasite densities (PDs): (b) (+), (c) (++), (d) (+++) and (e) (++++) at $\lambda = 405$ nm excitation.

Within the *i*-blood samples, as the PDs increases the fluorescence spectrum decreases in intensity and in width. Each spectrum peaks around 612±1 nm and shows a pronounced shoulder around 685±2 nm. This reduction in fluorescence intensities in the *i*-blood samples may be attributed to the presence of malaria byproduct (hemozoin) in the blood, acting as a fluorescence quencher. It may, also, be attributed to the reduction in the Hb concentration, as a result of partial digestion of the Hb content by the parasite residing in the infected red blood cells (*i*-RBCs). Besides, these observations could also be attributed to variations in the energy distribution between

113

fluorophores resulting to fluorescence quenching in the *i*-blood samples. Increasing concentrations of the hemozoin or a reduction in Hb concentration with increasing PDs may have accounted for the decreasing intensities of the *i*-blood spectra.

In order to bring out the latent shoulder peaks within the fluorescence spectra, PeakFit software (4.11 version, Jandel Scientific, Germany) was used to analyze the fluorescence spectra of the *u*-blood samples and the *i*-blood samples. The PeakFit software, as applied by Anderson et al. (2004), combines Loess smoothing function, Marquardt-Levenberg and Lorentzian spectral functions for analyzing the fluorescence spectra. It determines the accurate total minimum value of the sum of the squared deviations. The value of the relationship coefficient and the pattern of residue determines the quality of the fit. The Lorentzian spectra function aided with the choosing of a reasonable corresponding fit of the spectra. This enabled the determination of a high-quality *t*-test, standard errors for peak amplitude, peak centre and Full Width at Half Maximum (FWHM) for further analysis.

The characteristics of the Lorentzian bands obtained from the curve fit analysis of the fluorescence spectra for the *u*-blood samples and the *i*-blood samples with different PDs are shown in Figures 17 and 18 respectively. The decision for the Lorentzian band was based on precise fit of the measured spectra with high-quality values. In Figure 18, it can be observed that the ordinate scales are different across the 4 sets (a-d). This was done as a visual aid to make the underlying peaks more conspicuous.

114
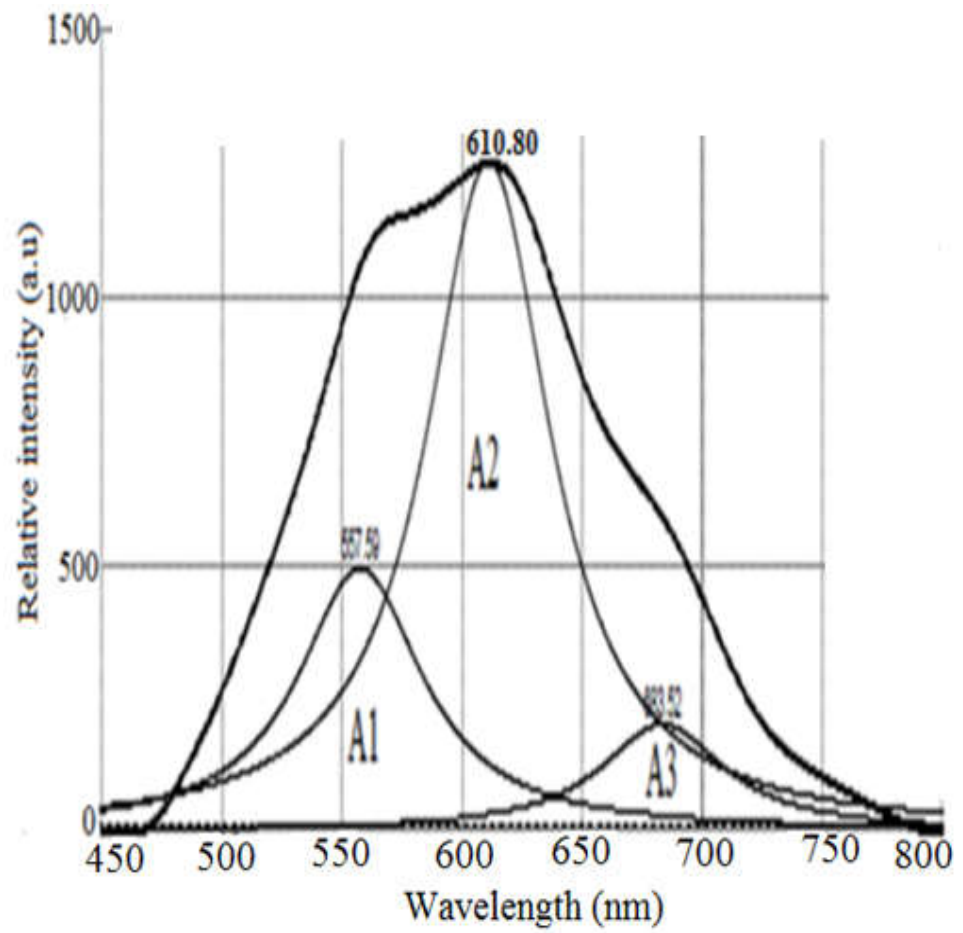
Figure 17: Fluorescence intensity distribution of uninfected blood (*u*-blood) sample fitted with Lorentzian function.

115
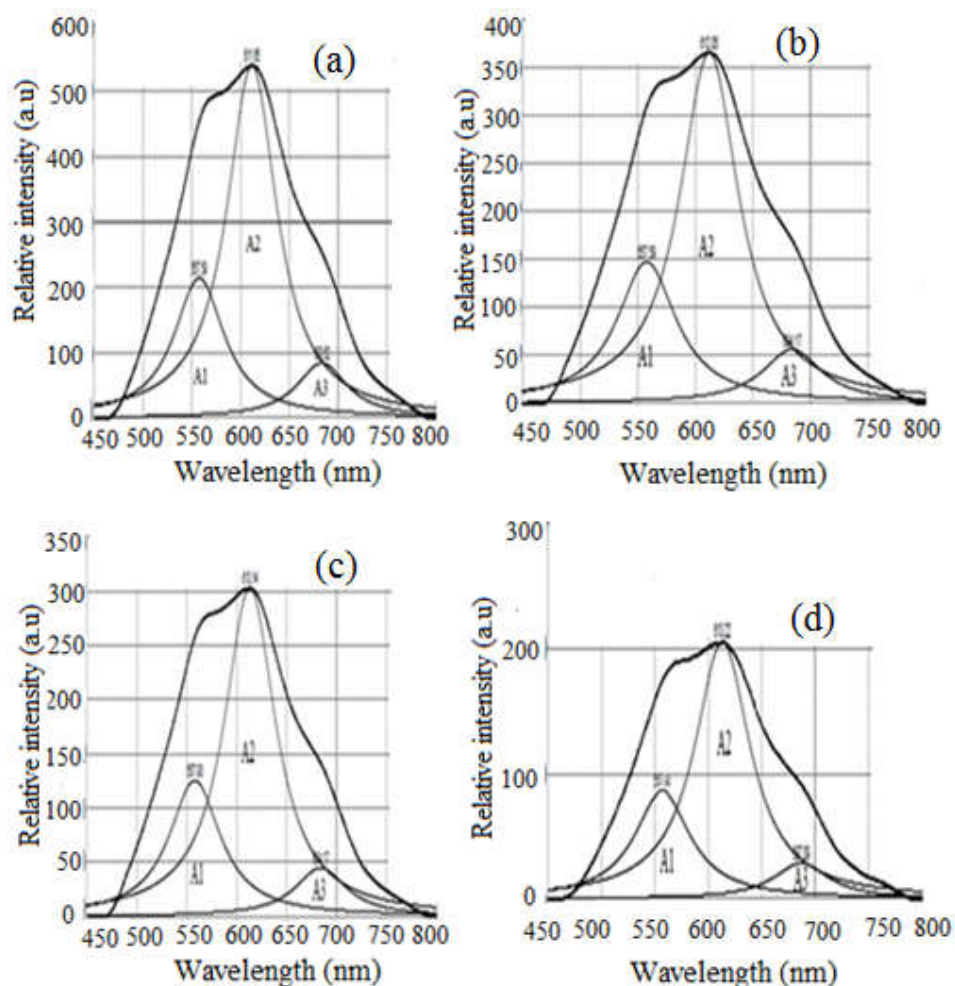
Figure 18: Fluorescence intensity distribution of *Plasmodium falciparum* infected blood (*i*-blood) sample with different parasite densities (PDs): (a) (+), (b) (++), (c) (+++) and (d) (++++) fitted with Lorentzian function.

Figures 17 and 18 show broader spectra bands for the *u*-blood samples (Figure 17) as compared to the *i*-blood samples (Figure 18 (a-d)). This can be attributed to the interaction between neighbouring molecules and the large number of vibration levels in the *u*-blood samples, compared with endogenous fluorophores in the *i*-blood samples undergoing transformation. Besides, it can be observed from the Figures 17 and 18 that the relative fluorescence intensity values were high in the *u*-blood samples than the *i*-blood samples. Even in the

116

i-blood samples, the relative peak fluorescence intensity values decreased with increasing PDs. This observation could be attributed to Hb degradation in the *i*-blood samples that is externally initiated and perpetrated by the parasite which breeds and multiplies inside the RBCs of *P.falciparum* infected patients. This provides enabling environment for fluorescence quenching. Most of the symptoms and complications of *P.falciparum* infections may be attributed to the rapid and abnormal lyses of the RBCs (Masilamani et al., 2014), and this spectra diagnosis provides an evidence for this point of view. Figures 17 and 18 show that the *i*-blood samples could be distinguished with variations in the fluorescence spectra intensities from the *u*-blood samples. This is because the plasma of the *i*-blood samples was flooded with fluorescence decay of intensities.

Three constituent bands, A1, A2 and A3 were extracted from the spectra of the *u*-blood and the *i*-blood samples. The A1 and A2 bands, reported elsewhere (Opoku-Ansah et al., 2014), originated from the fluorescence spectra of Hb whilst A3 band originated from the fluorophores of the collapsed feeble bonds (Gao et al., 2004). The reduction in the relative fluorescence intensities at the A2 bands as the PDs increase may be attributed to the reduction in the concentration of Hb (Moore et al., 2006). Increase in PDs decreased the relative fluorescence intensities at the A3 bands. This observation may be attributed to self-absorption phenomenon and structural rigidity of the fluorophores. The *P.falciparum* parasites growing in the *i*-blood secrete enzymes to digest the proteins in the *i*-RBCs. The *i*-RBCs membrane becomes enlarged and inelastic (Goldberg et al., 1990; Moore et al., 2006). Deformability therefore reduces in the *i*-RBCs. The higher the PDs in the

117

i-blood samples, the weaker the absorbed energy and the fluorescence spectra peaks were shifted to longer wavelength (Boulnois et al., 1986).

In order to estimate how precise the peak wavelengths and their corresponding intensities relates in the A1, A2 and A3 bands for the *u*-blood and *i*-blood samples, a graphical representation of the peak wavelengths with error bars was done and the results are presented in Figure 19. The figure shows variations in the independent peak wavelengths and their corresponding fluorescence intensities representing the A1, A2 and A3 bands for the *u*-blood and the *i*-blood samples.

Figure 19 shows the *u*-blood and the *i*-blood samples as two (2) groups as indicated by the error bars. Group 1 depicts *u*-blood samples whilst group 2 represents the *i*-blood samples with different PDs. From Figure 19, we can clearly see that the characteristic absorption of Hb (580-650 nm) is predominantly significant in group 1. What is more apparent in the figure is the increased absorption over the spectral range as we move towards group 1 from group 2. These observations may be as a result of partial scattering characteristics of RBCs, which heavily depend on the shape and orientation of the RBCs as well as the angle of the incident light.

118

Figure 19: Variations in peak wavelengths of uninfected blood (*u*-blood) (red colour), and *Plasmodium falciparum* infected blood (*i*-blood) samples with different parasite densities (PDs): (+, green colour), (++, blue colour), (+++, black colour) and (++++, cyan colour).

The changing of spectral characteristics is most apparent in group 2, where there is a decrease in intensity with increasing PDs for the peak wavelengths above 600 nm. According to Yulia et al. (2010) and Wilson et al. (2011), hemozoin displays a particular absorption band within 630-700 nm. It does make sense that the hemozoin contained in the *i*-blood samples (group 2) gives the strongest contrast because not only the parasite, but also the hemozoin that it expels, has structure providing contrast with regard to the fluorescence spectral characteristics of the *u*-blood samples (group 1), containing only Hb .

For meaningful results in most LIF applications, the fluorescence intensities ought to be compared due to the relative nature of the spectra. In

119

view of that, fluorescence peak intensity ratio (PIR) was empirically determined from the fluorescence spectral bands A2 and A3 using equation 44.

$$PIR = \frac{I_2 - \beta I_3}{I_3} \qquad (44)$$

where β is a constant, I_2 and I_3 are the peak intensities of A2 and A3 respectively. From the relation, it can be observed that the PIR value is affected by the fluorescence intensity in the A3 band. The peak fit analysis of the fluorescence spectra from the *u*-blood and the *i*-blood samples had accompanied uncertainties. Using these uncertainties, error margins for the PIR was calculated for the *u*-blood and the *i*-blood samples. Table 2 shows the variations in peak wavelengths of the *u*-blood and the *i*-blood samples for the different PDs under the Lorentzian curves and the PIR values.

Table 2

Peak wavelengths of uninfected blood and Plasmodium falciparum infected blood samples with different parasite densities under the Lorentzian curve.

Blood samples		Peak wavelength (nm)			Peak intensity ratio
		A1	A2	A3	(PIR)
u-blood		557.51±0.04	610.80±0.03	683.52±0.05	0.2343±0.07
i-blood	+	557.59±0.15	611.65±0.05	683.52±0.04	0.4343±0.04
	++	557.59±0.09	612.05±0.08	684.17±0.09	0.5563±0.05
	+++	557.93±0.07	613.14±0.05	684.17±0.18	0.7823±0.08
	++++	557.94±0.04	613.22±0.10	687.09±0.17	1.2095±0.13

From Table 2, it can be observed that the A1 band show almost the same peak wavelengths for the *u*-blood and the *i*-blood samples, even though there are slight differences. Besides, Table 2 also shows that as the PDs

120

increased, the peak wavelengths of A2 and A3 bands shifted, but the corresponding differences are not even. These observations show that in the A1 band, the *u*-blood samples and the *i*-blood samples show similar fluorescence peak spectra characteristics. The shift in the peak wavelengths with increasing PDs in the A2 and the A3 bands may be due to variations in the environment of fluorophores in the *i*-blood samples and possibly a reduction in energy due to Hb breakdown. Table 2 shows that the PIR value for the *i*-blood samples ranges from 0.4 to 1.2, which is above that of the *u*-blood samples (less than 0.3). Figure 20 depicts the graphical variations in PIR values in Table 2 representing the *u*-blood samples and the *i*-blood samples with different PDs.
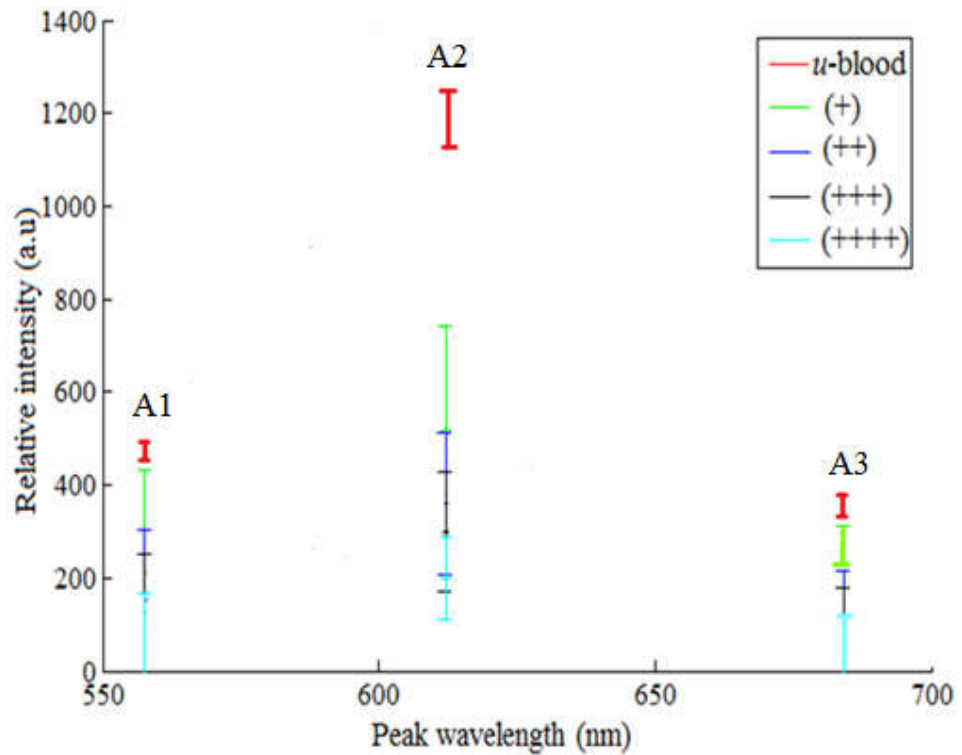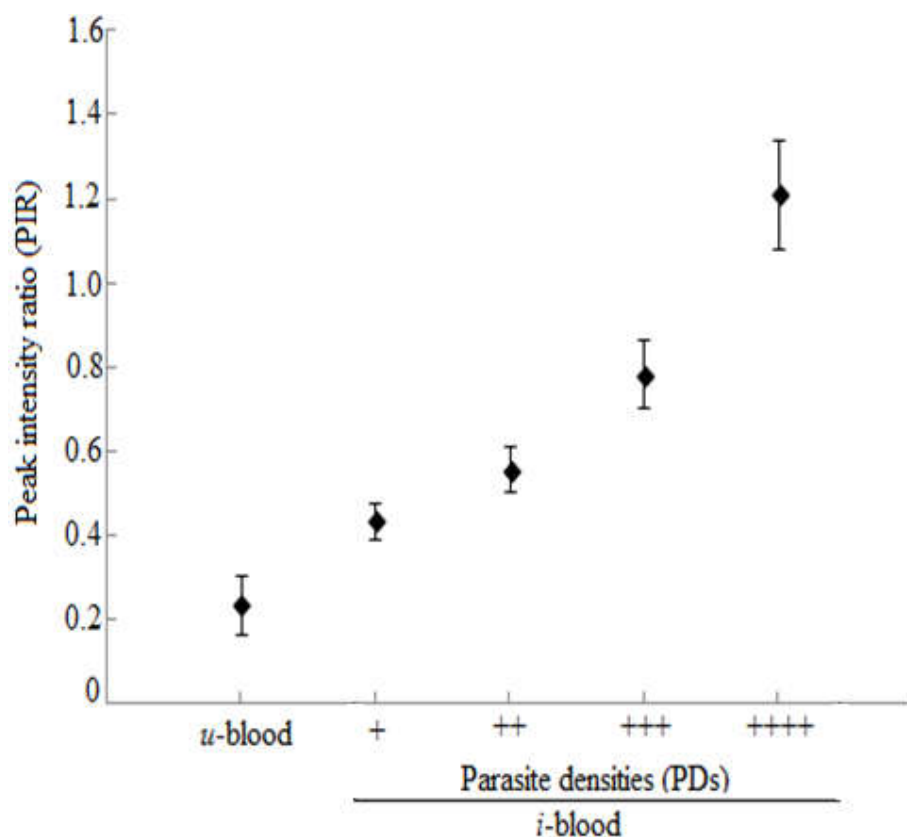

Figure 20: Variations in peak intensity ratio of uninfected blood (*u*-blood) samples and *Plasmodium falciparum* infected blood (*i*-blood) samples with different parasite densities (PDs).

121

From Figure 20, it can be observed that the *u*-blood samples compared to the *i*-blood samples with different PDs show a low PIR value. This in a sense suggests that the fluorescence spectra peak intensity in the A3 band is high in the *u*-blood than the *i*-blood samples. It can also be observed from Figure 20 that the PIR values increased with increasing PDs. These observations may be attributed to sequential reduced absorption of the incident light by the *i*-blood samples. Therefore, increasing PDs in the *i*-blood samples decreased the fluorescence spectra peak intensity in the A3 band. Thus, within the range of fluorescence spectra of Hb, fluorescence spectra peak intensity showing a Lorentzian curve under A2 band increases whilst that of Lorentzian curve under A3 decreases (Figure 18). These observations suggest that Hb degradation in *i*-blood samples results in high PIR for the spectra region representing A2 band than in A3 band.

Energy transfer between endogenous fluorophores in the *i*-blood samples with different PDs triggered the blood absorption by ground state molecules, resulting in fluorescence quenching in *i*-blood (Liu & Peng, 2000).When the *i*-blood samples with different PDs were excited by the same light source, the peak wavelengths of the fluorescence spectra were red-shifted. This red-shifted phenomenon (with increasing PDs) in *i*-blood samples could be due to the biochemical, morphological and/or environmental changes of the fluorophores as a result of hemozoin in *i*-blood samples. The results suggest that fluorescence spectra PIR might be used to predict the level of *P.falciparum* infections in *i*-blood samples for prompt diagnosis and treatment.

122

Optical Density Determinations of Blood

Optical densities (ODs) of Soret band (S-band) (405 nm), beta band (β-band) (541 nm) and alpha band (α-band) (577 nm) for the *u*-blood and *i*-blood samples were imported into Microsoft Excel platform. In this platform, the reference ODs representing these bands were subtracted from each *u*-blood and *i*-blood samples ODs recorded at the bands. The *u*-blood samples are composed of Hb and their spectra are dominated by the spectral fingerprint of the Hb which is strongly characterized by the S-band, the β-band and the α-band (Hanson & Ballantyne, 2010).

The ODs at the S-band for the *u*-blood samples relative to the OD of the *i*-blood samples, and the ratio of the ODs at the β-band to the α-band were respectively calculated using equation 45 (an empirical relation) and equation 46 as described by Antonini and Brunori (Antonini & Brunori, 1971). Table 3 provides the variations in the mean, the relative and the ratio of the ODs for the *u*-blood and the *i*-blood samples measured at Soret- band, β-band and α-band.

$$OD_{R(S-band)} = OD_{(u-blood)} - OD_{(i-blood)} \qquad (45)$$

$$OD_{(\beta/\alpha)} = \frac{OD_{\beta-band}}{OD_{\alpha-band}} \qquad (46)$$

123

Table 3

Optical densities of uninfected blood and Plasmodium falciparum infected blood with different parasite densities (PDs) at Soret- band, β-band and α-band.

Blood samples		Mean optical densities (ODs) (a.u)				
		S-band	β-band	α-band	$OD_{R(S\text{-}band)}$	$OD_{(\beta/\alpha)}$
u-blood		1.07±0.06	0.09±0.04	0.10±0.04	1.06±0.01	0.90±0.01
i-blood	+	1.04±0.01	0.05±0.05	0.08±0.02	0.03±0.01	0.79±0.01
	++	0.99±0.06	0.06±0.06	0.07±0.05	0.07±0.03	0.68±0.01
	+++	0.71±0.05	0.08±0.08	0.15±0.10	0.35±0.01	0.60±0.01
	++++	0.64±0.04	0.07±0.03	0.17±0.08	0.42±0.01	0.40±0.02

There are variations in the observed ODs (Table 3) for the *i*-blood samples in relation to the *u*-blood samples at the Soret-band, the β-band and the α-band. The ratio of the β-band to α-band ODs for the *u*-blood samples reduced by about 2.3 % as compared to the literature value of 0.9200 (Antonini & Brunori, 1971). The Soret-band showed a high OD for the *u*-blood samples and reduced with increasing PDs in the *i*-blood samples. These observations suggest that the presence of the parasite in the *i*-blood samples triggered Hb degradation with increasing PDs, hence, weak Hb absorption at the Soret-band.

At the β-band, high OD was observed for the the *u*-blood samples and varied in the *i*-blood samples. The OD was slightly high in PDs of (+) and reduced in (++), (+++) and (++++). These inspections indicate that, at the β-band, there was high Hb absorption for the *i*-blood samples representing PDs of (+) and weak Hb absorption for the samples with PDs (++), (+++) and

124

(++++), as a result of the growth of the parasite. And that, at the β-band, PDs estimation does not correlate either directly or inversely with Hb absorption.

Similarly, at the α-band, the OD was high for *u*-blood samples with variations in that of *i*-blood samples. The ODs reduced when the PDs were increased from (+) to (++). It however increased with increasing PDs from (+++) to (++++). These observations show that Hb absorption, at the α-band, is high for *u*-blood samples and *i*-blood samples with PDs of (+++) and (++++), and low for *i*-blood samples with PDs of (+) and (++). And that, at the α-band, Hb absorption is inversely correlated with the parasites' degree of infections from (+) to (++), and directly correlated with the parasites' degree of infections from (+++) to (++++).

Figures 21 and 22 respectively show ODs at the S-band for the *u*-blood samples relative to the ODs of the *i*-blood samples, and the ratio of the ODs at the β-band to the α-band. Changes in ODs were observed in the case of the *i*-blood samples. The figures show the trend for intraerythrocytic stage development of *P.falciparum* parasites in *i*-blood samples which starts with rapid multiplication and transformation in the parasites' physical structure and chemical composition occur during this development. These included changes in the size and shape of the protozoa cells, internal morphology, and amounts of nucleotides and hemozoin (Bannister et al., 2000).
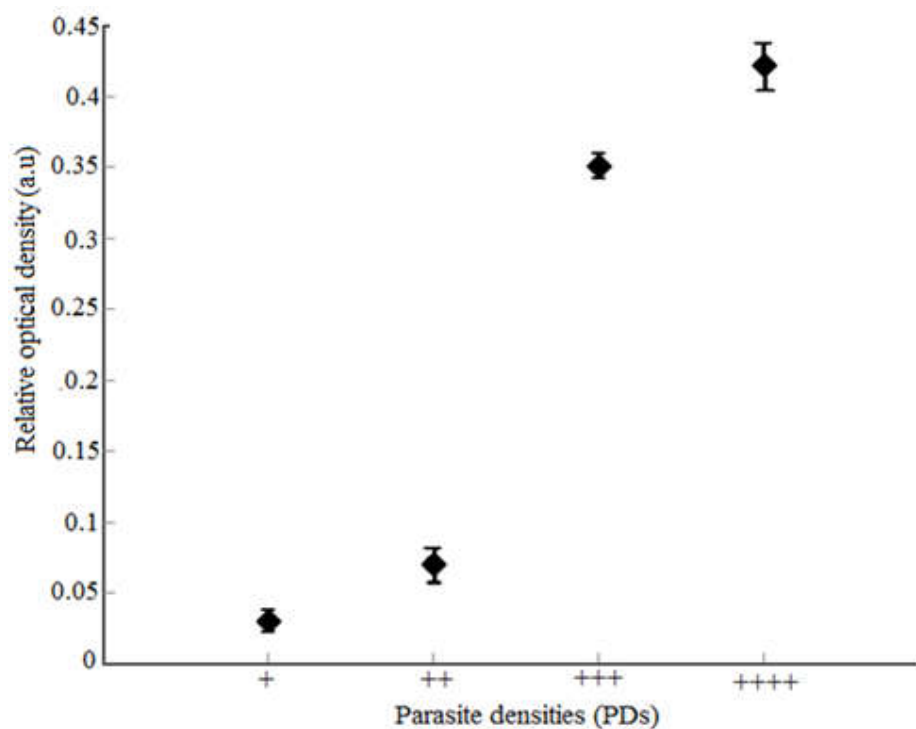
Figure 21: Relative optical densities (ODs) of *Plasmodium falciparum* infected blood (*i*-blood) samples with different parasite densities (PDs) at the Soret-band.

Figures 21 and 22 show graphical variations in the relative ODs and ratio of ODs. It can be observed from Figure 21 that the relative ODs increased with increasing PDs. The highest relative OD was observed at PD (++++), reduced through PD (+++) and PD (++), with PD (+) having the lowest. These observations suggest that within the range of Hb absorption at the Soret-band, the difference in ODs between the *u*-blood samples and the *i*-blood samples with different PDs increases indicating the growth of the parasite. There is a sudden jump in the relative OD values from PD (++) to PD (+++). This might be due to the structural and biochemical alterations in the *i*-blood samples as the parasite grows. This observation also suggests that it may seem complex to identify the parasites in the initial stages of development (+),

126

and that parasites' identification becomes more noticeable during the latter stages of development (++++).
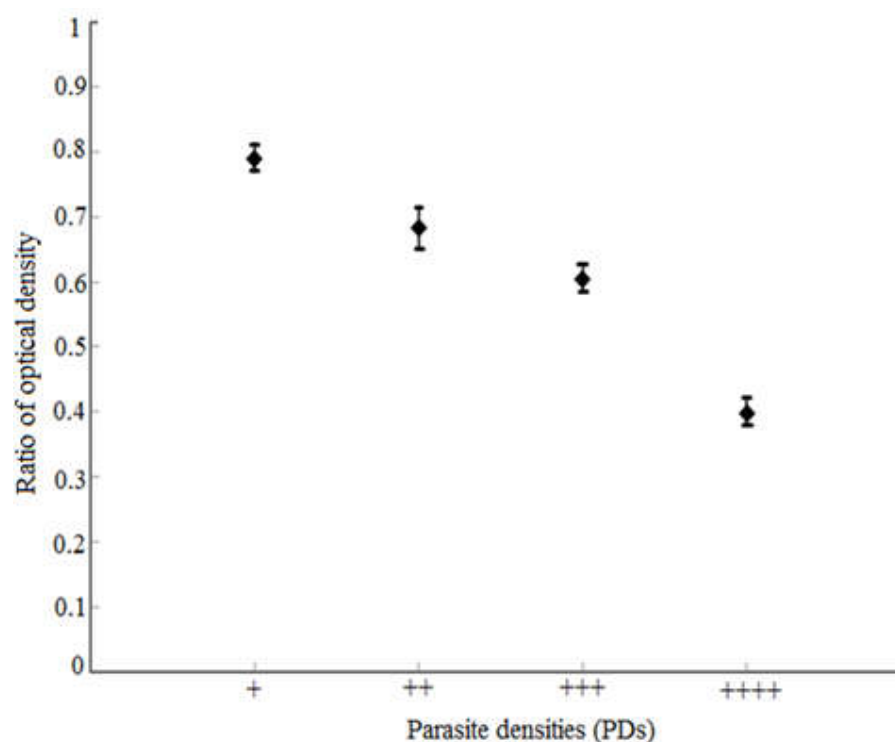
Figure 22: Ratio of β-band (541 nm) to α-band (577 nm) representing optical densities (ODs) of *Plasmodium falciparum* infected blood (*i*-blood) samples with different parasite densities (PDs).

In Figure 22, it can be observed that the ratio of the β-band ODs to the α-band ODs ($OD_{(\beta/\alpha)}$) values decreased with increasing PDs in the *i*-blood samples. The highest $OD_{(\beta/\alpha)}$ value was observed at PD (+), followed by (++), then (+++) with (++++) having the least. These observations suggest that Hb degradation in the *i*-blood samples results in low $OD_{(\beta/\alpha)}$ values. Besides, reduction in Hb absorption at α-band influenced the Hb degradation in the *i*-blood samples. Decreased $OD_{(\beta/\alpha)}$ values with increasing PDs can be attributed to successive increase in stiffness of membranes inside infected

127

RBCs (*i*-RBCs) which are in the *i*-blood samples. This confirms the work of Paulitschke & Nash, (1993) and Glenister et al. (2002).

Spectral Images

Three grayscale images, obtained from the multispectral light emitting diode imaging microscope (MSLEDI) in reflection, scattering and transmission modes respectively, are as shown in Figure 23 (a-c). The figure shows images containing uninfected red blood cells (*u*-RBCs) and *P.falciparum* infected red blood cells (*i*-RBCs) interspersed in a non-uniform background. The images have 2592 x 1944 pixels dimension but different grayscales. These images were captured using 590 nm excitation light source from a test (unstained) slide. This spectral band was used for standardization due to its sensitivity to the imager.

It can be observed that Figure 23(a), which is an image in reflection mode, appears dark. This goes to suggest that low reflected intensities of light were imaged through the *u*-RBCs and the *i*-RBCs. The scattering mode image (Figure 23(b)) depicts dimmer or less scattered light intensities in the *u*-RBCs and the *i*-RBCs. Figure 23(c), that is, transmission mode, shows the brightest image obtained. This indicates that more light intensities from the excitation light source were transmitted through the *u*-RBCs and the *i*-RBCs to the imager. Therefore, based on the theory that A+R+S+T= 1, that is equation 25, it can be see that T is very high for 590 nm than R, S and A.

128
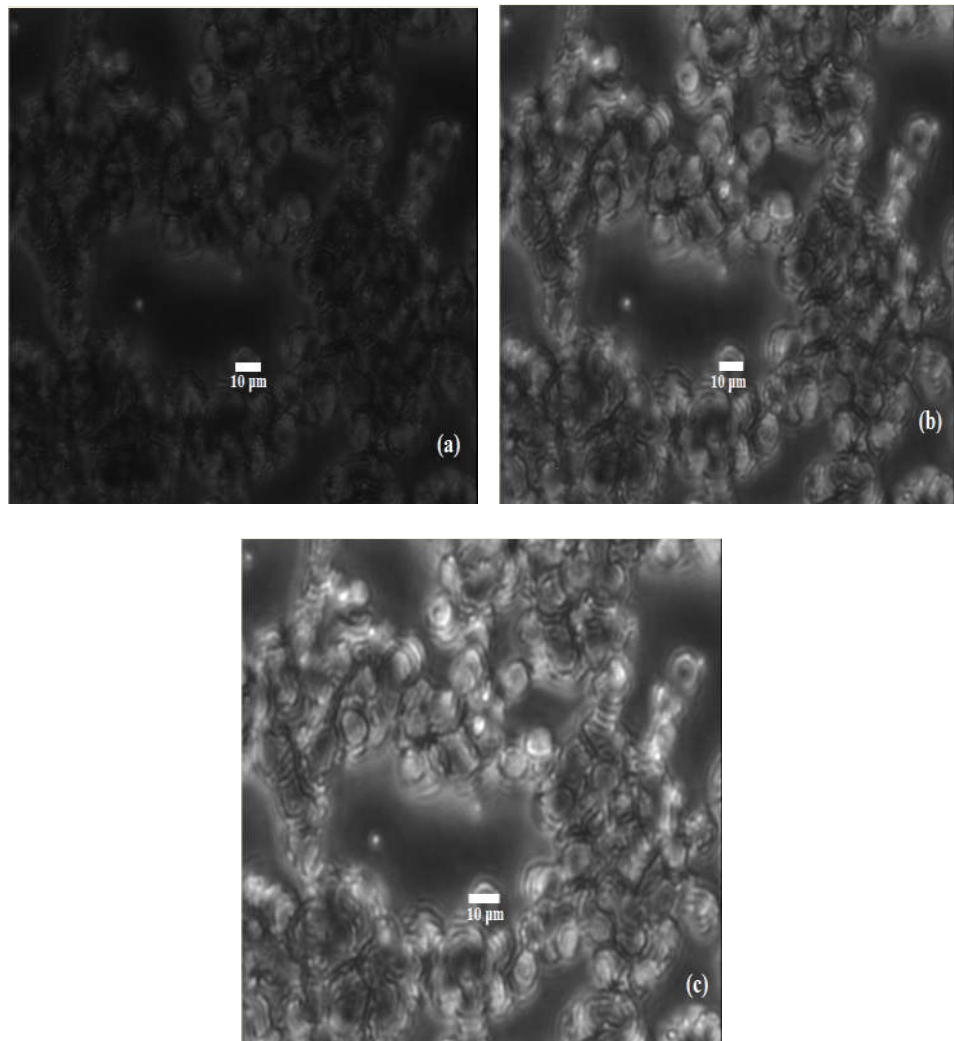
Figure 23: Three grayscale images acquired from an unstained blood smear slide using multispectral light emitting diode imaging microscope (MSLEDI) in (a) reflection, (b) scattering and (c) transmission modes. The images were captured using excitation LED source of 590 nm.

129

Colour Representation of Spectral Images

Colour representation of images in an uncompressed form typically consist of red (R), green (G) and blue (B) (RGB) colour planes, where the data in each image plane has undergone a nonlinear correction to make the image appropriate for viewing (Sharma & Trussell, 1997). The spectral images from the test slides, representing the 13 spectral bands, in reflection, scattering and transmission modes, were imported into Matlab platform for analysis. Colour images were formed for each mode via Matlab by combining images acquired at 660 nm (red), 590 nm (green) and 435 nm (blue) (Figure 24), following a procedure presented by Merdasa et al. (Merdasa et al., 2013).

Figure 24 (a-c) shows images from the same region of the blood smear slide under the MSLEDI in all the three modes. Therefore the images appear as though they were observed under light microscope. Since all the image acquisitions were done in all the three modes without moving the sample, each image pixel can be examined in all the three modes. Nonetheless, the effective pixel-size of the imager (2.2 μm per pixel) was far below the diffraction limit set by the MSLEDI. These suggests that a pixel was affected by a number of near-lying pixels and could therefore not be considered individually. Assessing the *u*-RBCs and the *i*-RBCs as a whole, one can contend that pixels extracted from different parts of the images could play crucial roles in differentiating the *u*-RBCs from the *i*-RBCs. Hence pixel extraction could be applied for malaria parasites' detection. Figure 24 shows spectral disparities in the colour images containing the *u*-RBCs and the *i*-RBCs in all the three geometries.
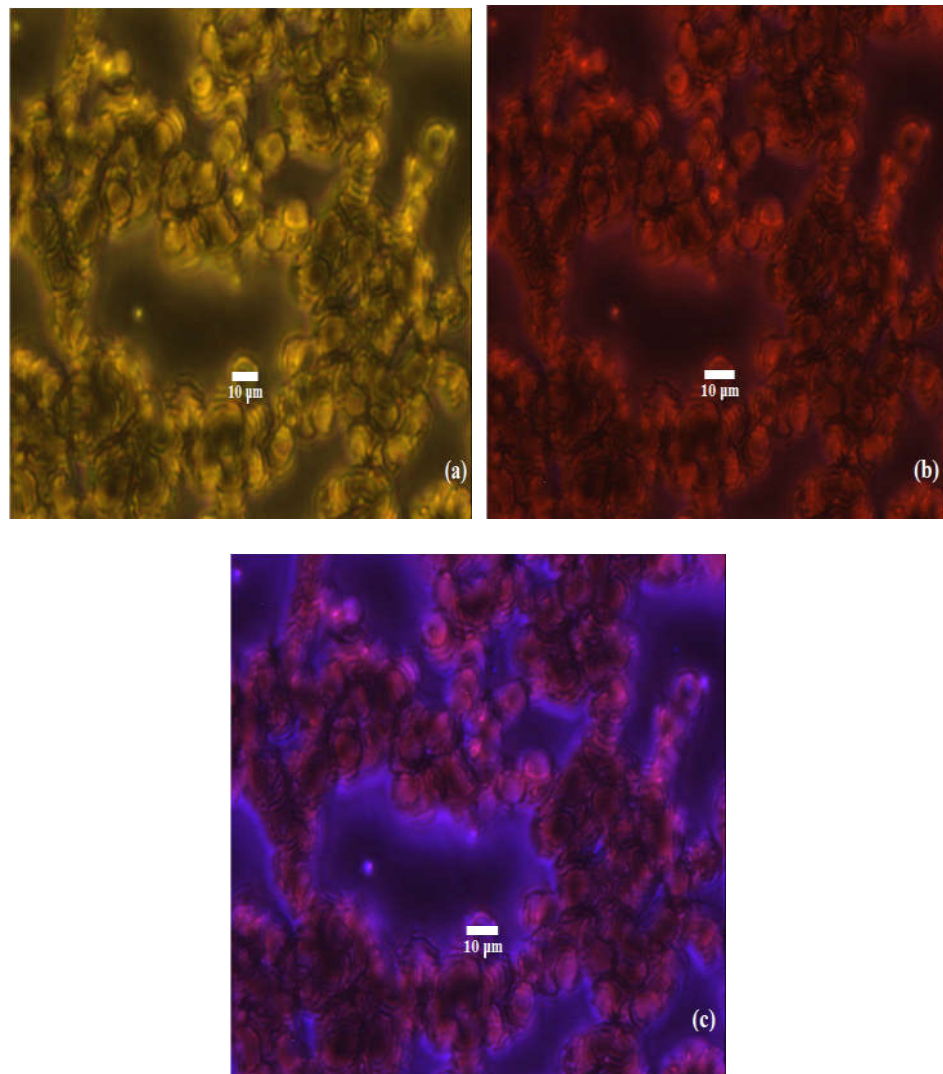
Figure 24: Colour representation of the three grayscale images acquired from three modes: (a) reflection, (b) scattering and (c) transmission, with the aid of a multispectral light emitting diode imaging microscope (MSLEDI). The images in each mode consist of combined images of 660 nm (red), 590 nm (green) and 435 nm (blue) from an unstained blood smear slide.

In 24(a) (reflection mode), most of the RBCs have shades of white in the edges and appear dark in the centre suggesting reflection of *i*-RBCs. Some RBCs also appear white in the centre indicating reflection of *u*-RBCs. In 24(b) (scattering mode), it can be observed that the *u*-RBCs which do not have internal structure appear more scattered whilst the *i*-RBCs appearing to have

131

internal structure seem to have unfilled centres with less scattering (Guering et al., 2002). These observations can be attributed to the life-cycle development of the *P.falciparum* parasite growing within the *i*-RBCs. In 24(c) (transmission mode), the red colour of the *u*-RBCs can be seen, but there is a clear distinction between the *u*-RBCs and the *i*-RBCs. The *i*-RBCs appear slightly brownish with dark spots at the centre indicating low absorption and high transmission of light whilst the *u*-RBCs appear redder with low transmission and high absorption of light.

Feature Extraction of Malarial Byproduct (Hemozoin) Optical Properties from Uninfected and Infected Red Blood Cells

Uninfected RBCs (*u*-RBCs) are cylindrically symmetric and are brought into line parallel to microscope slides containing blood smears. Thus, the optical properties of *u*-RBCs can be investigated in relation to the radius for any deformities. The hemozoin shows bright white or cyan colour in *i*-RBCs (Wilson et al., 2011). This malaria pigment can be identified in *i*-RBCs with the aid of a multispectral imaging microscope (Frey & Warda, 2008; Cosentino, 2013). The colour image of each test slide was compared with their corresponding grayscale image since they were all captured from the same microscopic field.

In order to identify the *i*-RBCs from the *u*-RBCs in the colour images, the *i*-RBCs depicting the hemozoin colour were matched to the same *i*-RBCs in the grayscale images. Intensities of the *u*-RBCs and the *i*-RBCs in the grayscale images for the 13 spectral bands were extracted and converted into radii. This was achieved by multiplying each pixel by the effective pixel size

132

of the imager. Figures 25-27 show a projection of reflected, scattered and transmitted intensities of *u*-RBCs and *i*-RBCs onto a surface. Figures 25-27 show spectral variations in the pixel intensities extracted from the *u*-RBCs and the *i*-RBCs in all the three modes. The existence of the hemozoin or the decrease of Hb concentration appears in all the three acquisition modes suggesting the prevalence of infection (PDs). As suggested by Hanson and Ballantyne, (Hanson & Ballantyne, 2010), the *u*-RBCs which are essentially composed of Hb, and their spectra dominated by the spectral fingerprint of Hb, showed strong characteristics of the S-band, the β-band and the α-band in all three modes, but significantly, in transmission mode. The presence of the hemozoin, show up in all three acquisition modes, therefore giving a strong indication when an infection is prevalent. Hemozoin displays a particular absorption band at 630 and 660 nm (Yulia et al., 2010; Wilson et al., 2011).

133
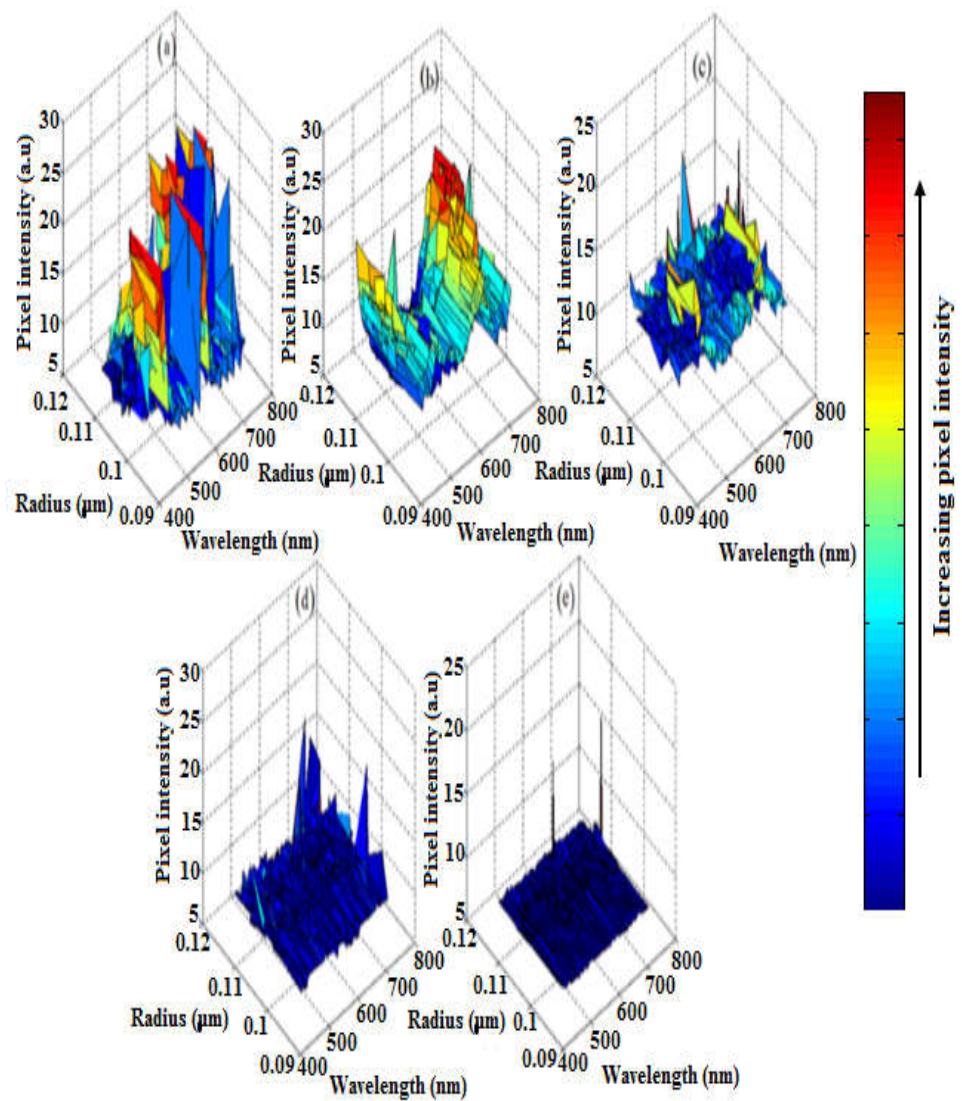
Figure 25: Projection of reflection intensities onto a surface; (a) uninfected RBCs (*u*-RBCs) and *Plasmodium falciparum* infected RBCs (*i*-RBCs) of parasite densities (PDs) (b) (+), (c) (++), (d) (+++) and (e) (++++).

Figure 25 shows increase in reflection of the red colour (RBCs colour) and green colour in *u*-RBCs and reduction in red and green colours in the *i*-RBCs with increasing hemozoin (increasing PDs). However, increasing hemozoin in *i*-RBCs results to an increase in reflection of blue colour. Reflection of red colour is seen typically in 25(a) and 25(b) suggesting the *u*-RBCs whilst reflection of blue colour shows up in 25(c-e) indicating the

134

i-RBCs. These observations suggest that increase in Hb reflects more light within the red spectral bands. And that, the presence of hemozoin in *i*-RBCs depicts reduction in reflection.
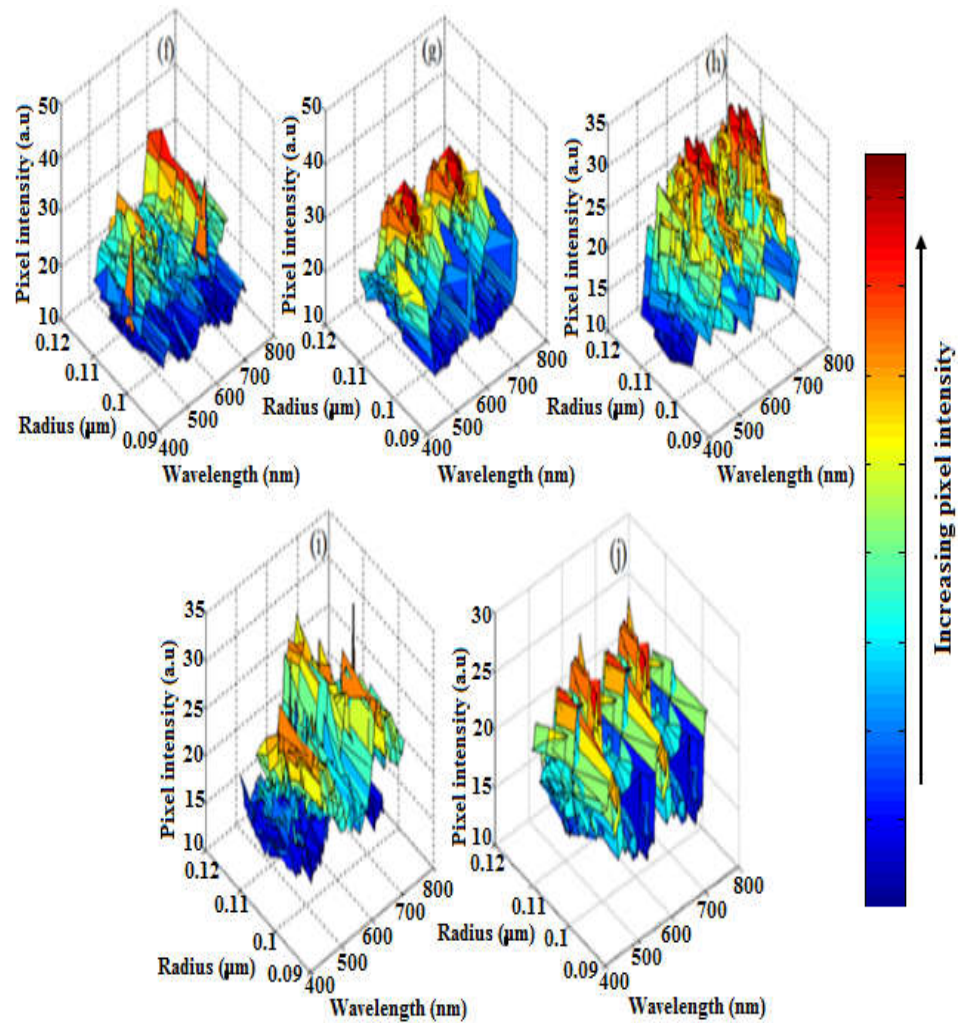
Figure 26: Projection of scattering intensities onto a surface; (f) uninfected RBCs (*u*-RBCs) and *Plasmodium falciparum* infected RBCs (*i*-RBCs) of parasite densities (PDs) (g) (+), (h) (++), (i) (+++) and (j) (++++).

Figure 26 shows scattering of the red colour at the edges of the *u*-RBCs 26(f) and at the centre of the *i*-RBCs 26(g-j). The *u*-RBCs lacked internal structures and therefore did not scatter the red colour at the centre. The presence of hemozoin in the *i*-RBCs show high scattering of blue and

135

green colours with increasing PDs. These observations suggest that at the

blood absorption bands (S-band, β-band and α-band), the *u*-RBCs and the

i-RBCs show strong and weak scattering properties respectively. And that, at

these absorption bands hemozoin depicts mostly blue colour.
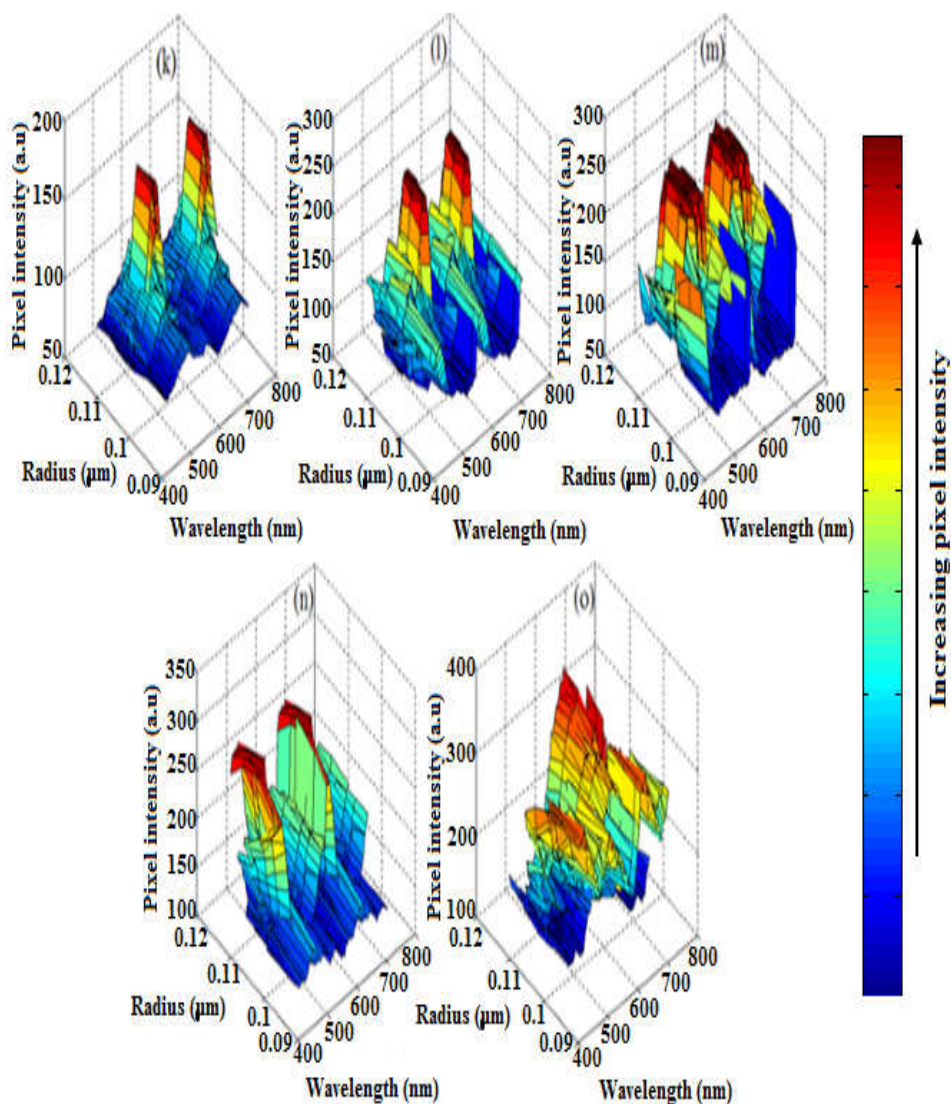
Figure 27: Projection of transmission intensies onto a surface; (k) uninfected
RBCs (*u*-RBCs) and *Plasmodium falciparum* infected RBCs (*i*-RBCs) of parasite densities (PDs) (l) (+), (m) (++), (n) (+++) and (o) (++++).

Figure 27 shows the transmission of red colour at the centre of both the *u*-RBCs 27(k) and the *i*-RBCs 27(l-o). Besides, the *i*-RBCs show high transmitted light intensity than *u*-RBCs. The Soret-band, β-band and α-band show sharp peak spectra in *u*-RBCs and the peaks representing these bands exhibit broader width with increasing PDs in *i*-RBCs. The hemozoin absorption band at 630-660 nm is depicted as blue colour in most of the *i*-RBCs. These observations indicate that *i*-RBCs have low absorption/or high transmission of light than *u*-RBCs which contain high Hb. And that, due to the presence of hemozoin in the *i*-RBCs, there is less absorption of red light in the hemozoin absorption band.

The applied technique in the above analysis was based on the pixel intensities representing *u*-RBCs and *i*-RBCs properties rather than specific *P.falciparum* pointers. For this reason, reflection, scattering and transmission spectra were studied in terms of average characteristics of the light intensities of the *u*-RBCs and the *i*-RBCs for the three modes. Spectral disparities between *u*-RBCs and *i*-RBCs were particularly observed by a decrease in reflection and scattering intensities, as well as increase in transmission intensities of *i*-RBCs compared with *u*-RBCs. And that, for analysis of *u*-RBCs and *i*-RBCs in spectral images, light transmission is the best optical approach. The central valley of *u*-RBCs (due to their biconcave shape) exhibited increase in scattering, reflection and absorption indicating the levels of infection. The increased transmission, and/or decrease in either scattering or reflection in the *i*-RBCs can be paralleled with the increasing PDs.

Geometrical and Optical Characteristics of Uninfected Red Blood Cells

(*u*-RBCs) *and Infected Red Blood Cells* **(*i*-RBCs)**

Infected RBCs (*i*-RBCs) appear stained when compared to *u*-RBCs which are slightly stained or unstained at all. Thus, the *i*-RBCs depict as dark spots in images. Also, as a result of the *u*-RBCs maintaining their biconcave shape in contrast to the *i*-RBCs, the *i*-RBCs show as dark spots in the centre and the edges. In view of this, images of the test set slides captured at the 13 spectral bands in transmission mode were imported into *Image Pro Plus 5.0* software (Media Cybernetics, USA), version 3.1 for windows 3.0 platform for further analysis. The *Image Pro* is dynamically linked to Microsoft's Excel to aid easy graphical representation. This is done using the dynamic data exchange (DDE) provided in the file menu of the data window.

In the *Image Pro Plus 5.0* platform, an image of a training set slide, prepared from a *u*-blood sample and captured at 590 nm, was imported. Touching and overlapping *u*-RBCs were removed. Attributes based on eccentricity or aspect ratio (AR) and integrated optical density (IOD) data were retrieved and saved into a folder for the non-touching *u*-RBCs in the image of the training set slide. After that, an image of test set slide with similar preparation acquired at the 590 nm was also imported in *Image Pro Plus* platform. Again, touching and overlapping *u*-RBCs were removed and the AR and the IOD data were retrieved and saved into the folder. Similar processes were followed for the AR and IOD data retrieval from the images at the remaining 12 spectral bands for the training and the test set slides. The AR and IOD data of the training and test set slides from the *u*-blood samples for the 13 spectral bands were grouped. The same procedure was repeated to

138

retrieve the AR and the IOD data from the *u*-RBCs and *i*-RBCs in the images acquired from all the training and test set slides prepared from the *i*-blood samples and captured at the 13 spectral bands. The AR and IOD data of the training and test set slides from the *i*-blood samples for the 13 spectral bands were also put together. In this data, all AR and IOD data for *u*-RBCs were removed. The AR and IOD data from *i*-RBCs in test slides that show similar AR and IOD data for the training test slides were maintained.

Histograms representing the number of *u*-RBCs and *i*-RBCs counted from the attributes were plotted with the aid of *Origin Pro 9.1* software. Figures 28 and 29 show plots of the histograms fitted with a Gaussian curve representing the distribution of AR and IOD for the *u*-RBCs and the *i*-RBCs with different PDs. Figure 28 shows a plots of the ratio of AR in the abscissa against counted *u*-RBCs and *i*-RBCs in the ordinate. Similarly, Figure 29 depicts plots of IOD in the abscissa with counted *u*-RBCs and *i*-RBCs in the ordinate. The Gaussian curve to the histograms exhibits normal distribution of image intensities of *u*-RBCs and *i*-RBCs representing the AR and the IOD data.
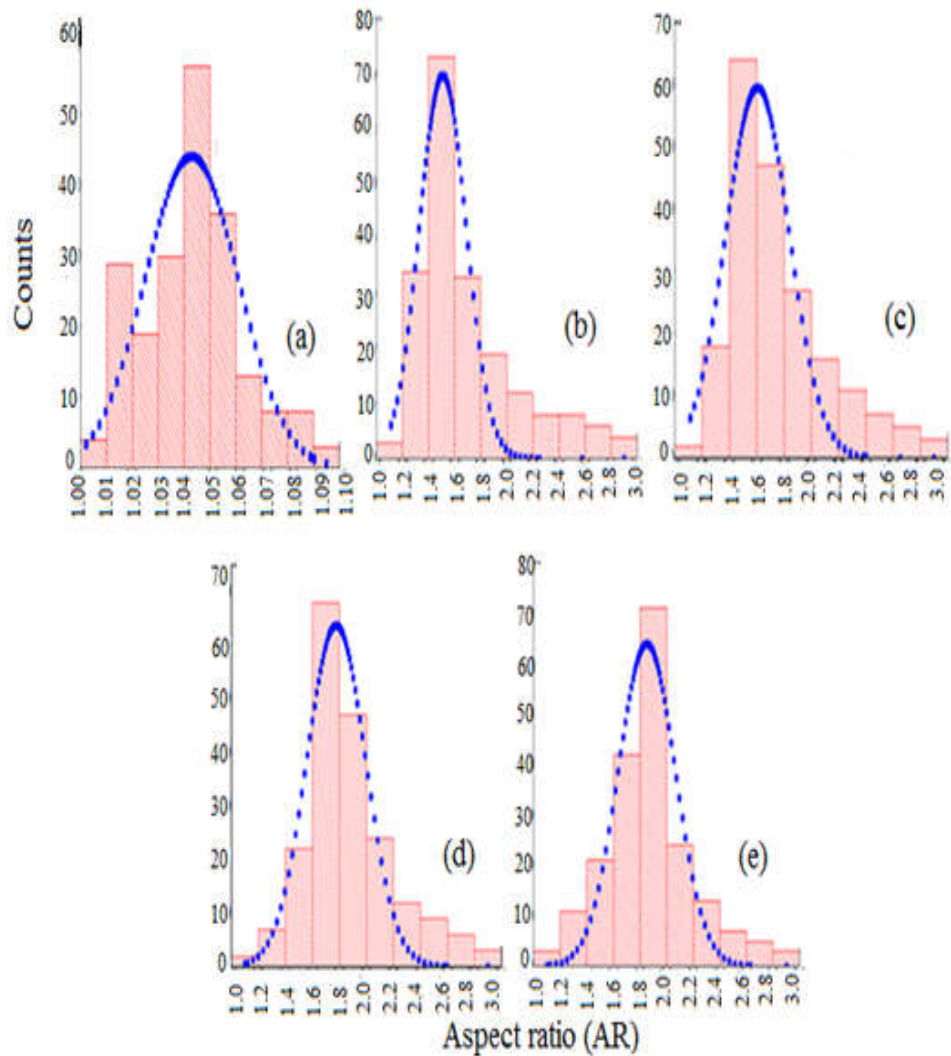
Figure 28: Histograms representing the distribution of aspect ratio for (a) uninfected blood cells and *Plasmodium falciparum* infected blood cells of parasite density (b) (+), (c) (++), (d) (+++) and (e) (++++) under a Gaussian fit curve.

From Figure 28(a), it can be observed that the histogram representing the *u*-RBCs with AR data has a sharp peak and a long tail in the Gaussian curve. This observation shows that the intensities of the *u*-RBCs tend to be very close to AR values. From Figure 28(a), it can also be observed that the AR values for *u*-RBCs ranges between 1.00 and 1.10. Again, Figure 28(a) shows that majority of the *u*-RBCs were counted between 1.04 and 1.05.

140

These observations show that the *u*-RBCs maintained their biconcave shape with the major axis directly proportional to the minor axis. This makes the *u*-RBCs more deformable during microcirculation. From Figure 28(b-e), it can be observed that increased AR (from 1.2 to 3.0) corresponds to increasing PDs in *i*-RBCs. The histograms representing the *i*-RBCs with the AR data show sharp peak in the Gaussian fitting and long tail for (+) and (++) PDs but round and thin tail for (+++) and (++++). This indicates that the *i*-RBCs look more transparent with more PDs. Majority of the *i*-RBCs were counted between 1.4 and 1.6 for + PD, the same values were repeated for ++ PD, 1.6 and 1.8 for +++ PD, and 1.8 and 2.0 for ++++ PD, indicating a shift to high AR values with increasing PDs. These observations can be attributed to the growth of the parasite in *i*-RBCs which makes *i*-RBCs more rigid and less deformable. And that, the *i*-RBCs deviate from the biconcave shape and gradually assume a spherical shape with AR values between 1.4 and 2.0.
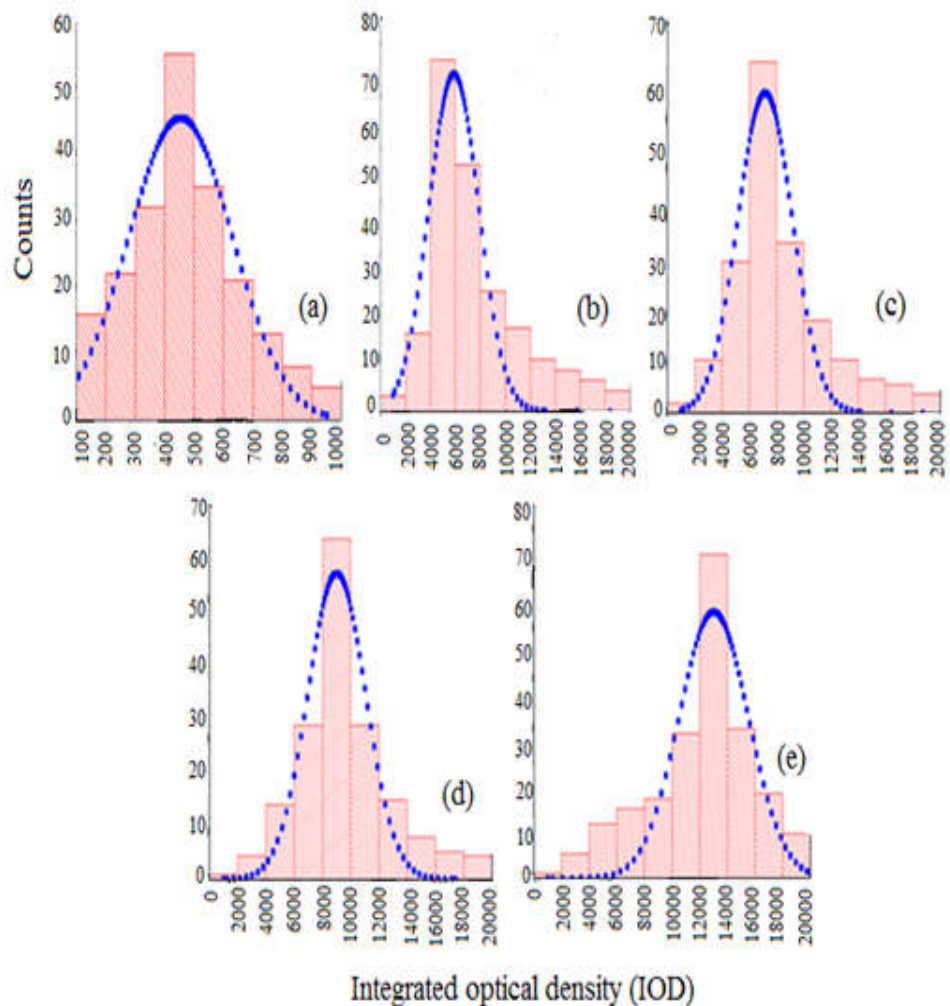
Figure 29: Histograms representing the distribution of integrated optical density (IOD for (a) uninfected blood cells and *Plasmodium falciparum* infected blood cells of parasite density (b) (+), (c) (++), (d) (+++) and (e) (++++) under a Gaussian fit curve.

Figure 29(a-e) show similar Gaussian curve characteristics as described earlier. From Figure 29(a), it can be seen that the *u*-RBCs show IOD values below 1000 with majority of the *u*-RBCs counted between 400 and 500. This observation depicts that the density of the *u*-RBCs are high hence a reduction in the IOD values. This property of the *u*-RBCs makes them more flexible during microcirculation. Figure 29(b-e) show significant disparities in the *i*-RBCs. Figure 29(b-e) show majority of the *i*-RBCs having IOD values

142

from 4000 to 6000 for + PD, 6000 to 8000 for ++ PD, 8000 to 10000 for +++ PD and 12000 and 14000 for ++++ PD. Increased IOD values correspond to increasing PDs. These observations show that the density of the *i*-RBCs reduces with increasing PDs, therefore, high IOD values are observed at high PDs.

Specifically, the shift in the AR and IOD values observed for the *i*-RBCs with increasing PDs are in agreement with cytoadherence experiments where parasite adhesion assays were carried out under static conditions using purified receptors, which is the simplest form of these assays. *Image Pro Plus* software was used and the *i*-RBCs showed < 3 and < 1000 for AR and IOD values respectively (Paton et al., 2011). Even though the observed IOD values in this work are above the ones observed in the work done by the above-mentioned researchers, differences in the IOD values may offer potential optical indicators for PDs estimation due to the increase in membrane bending rigidity of *i*-RBCs. These properties of the *i*-RBCs could further impair the ability of *i*-RBCs to comply with deformations in the flow, and consequently prevent their close packing in the flow core. Increase in stiffness of the *i*-RBCs as a result of increasing PDs could block small blood capillaries which tend to increase body temperature as one of the symptoms of malaria.

In addition, the property of the *i*-RBCs with increasing PDs to adhere to each other and to show themselves as vascular endothelium cells may strongly impair blood flow in capillaries and small arterioles resulting in a substantial increase of flow resistance. The rigidity of the *i*-RBCs as a result of the presence of the parasite may constrain the cell membrane, which may affect the bending of the *i*-RBCs. The presence of the parasite in the *i*-RBCs

143

may also affect changes in the adhesiveness of *i*-RBCs. This may result in an inconsistent adhesive behaviour of the *i*-RBCs compared to a more steady adhesive dynamics of the *u*-RBCs. Figure 30 shows a variation in the mean (μ) distribution of the AR data and IOD data for the *u*-RBCs and *i*-RBCs of the different PDs.
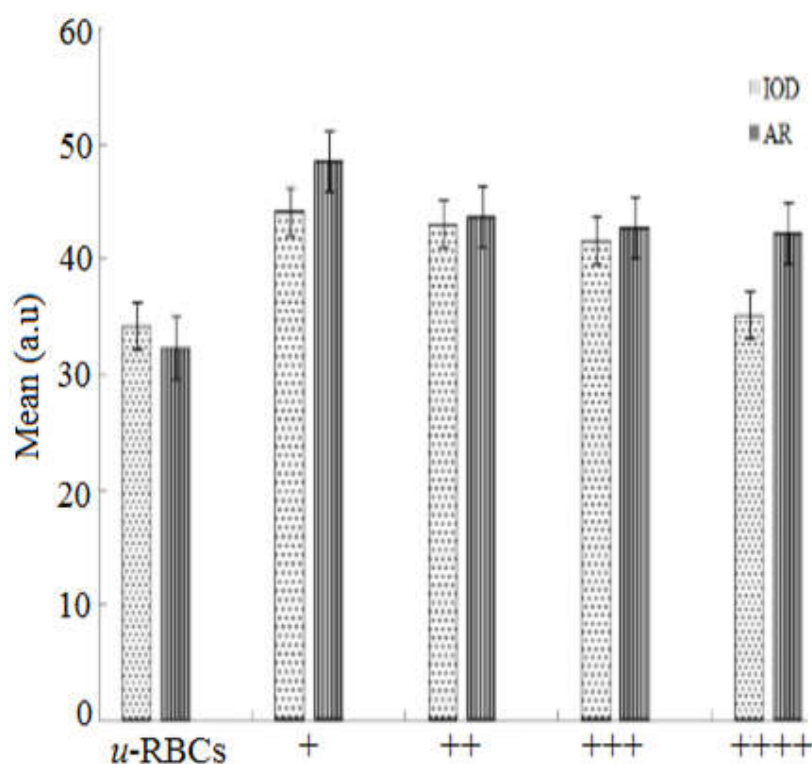
Figure 30: Variation in mean distribution of aspect ratio (AR) and integrated optical density (IOD for uninfected blood cells and *Plasmodium falciparum* infected blood cells of parasite densities +, ++, +++ and ++++.

From Figure 30, it can be seen that the *u*-RBCs show low μ value less than 40 for both AR and IOD. This suggests that the average pixel intensity levels were low due to high Hb absorption in *u*-RBCs. High μ value was recorded in *i*-RBCs with PD of (+) for both AR and IOD values and the μ values decreased with increasing PDs in the *i*-RBCs. These inspections suggest that as the parasites enter *i*-RBCs, the *i*-RBCs become less dense and

144

more enlarged assuming a spherical shape. Thus, deformability decreases whilst transmissivity increases in the *i*-RBCs resulting in high AR and IOD in the *i*-RBCs with increasing PDs.

*Identification of Spectral Bands as-Markers for Intraerythrocytic Life Cycle Stages of Infected Red Blood Cells (**i**-RBCs)*

Figure 31(a-c) shows three grayscale images of the blood smear slides captured from the MSLEDIM with 590 nm excitation LED source. The figure depicts images with dark background interspersed with spots representing the *u*-RBCs and the *i*-RBCs. The *i*-RBCs are in their intraerythrocytic stages: ring, trophozoite and schizont. These images also have the same 2592 x 1944 pixels dimension with different grayscales in an uneven background. The different grayscales are as a result of selective absorption of the *u*-RBCs and the *i*-RBCs at the 590 nm excitations. Figure 31(b) and (c) show some ruptured RBCs indicating the *i*-RBCs. This observation is as a results of the growth of the parasite which ruptures the *i*-RBCs as it matures from the trophozoite stage to the schizont stage.
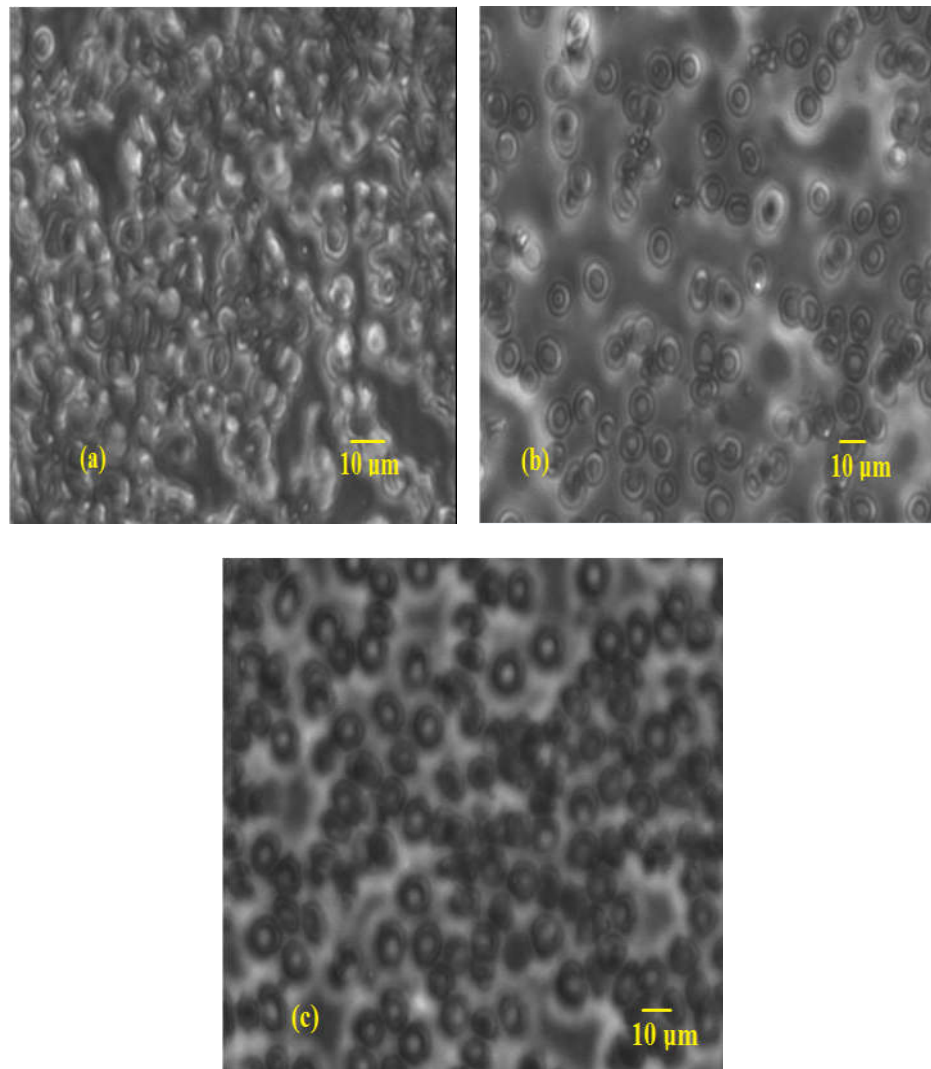
Figure 31: Three grayscale images captured from multispectral light emitting diode imaging microscope containing uninfected red blood cells (*u*-RBCs) and *Plasmodium falciparum* infected red blood cells (*i*-RBCs) on thin blood smear slides in the intraerythrocytic stages: (a) ring (b) trophozoite and (c) schizont. The spots in the images represent the *u*-RBCs and the *i*-RBCs.

The spectral images containing the unstained *u*-RBCs and the *i*-RBCs in the ring, trophozoite and schozont stages, were analyzed following a similar work described elsewhere (Opoku-Ansah, 2012). In that work, cultured parasites (in an *ex vivo* environment) on blood smear slides stained with Giemsa dye were used. The images, with unstained *u*-RBCs and *i*-RBCs were

146

imported into Matlab platform for further analysis. In the Matlab platform, colour representation of the images for hemozoin detection and matching of the colour images to grayscale images to identify the i-RBCs were done as described earlier.

Maximum pixel intensity values were extracted from the u-RBCs and the i-RBCs contained in the grayscale images for all the test slides captured at the 13 spectral bands in transmission mode. In each image, and at all the spectral bands, maximum pixel intensity values were extracted from two (2) each of the u-RBCs and the i-RBCs. Average pixel intensity values were found for all the maximum pixel intensity values at each spectral band. Figures 32-37 show plots of pixel intensity values of the u-RBCs and the

i-RBCs extracted from grayscale images of test slides with the ring stage, the trophozoite stage and the schizont stage against the 13 spectral bands of the excitation LED sources. Figures 32-34 show plots in the work described in (Opoku-Ansah, 2012), where maximum pixel intensity values were plotted against the 13 spectral bands. Figures 35-37 show the average pixel intensity values representing the 13 spectral bands for all the test slides. The figures show comparisons of pixel intensity values extracted from the u-RBCs and the i-RBCs in cultured blood smear slides stained with Giemsa dye to that of unstained blood smear slides prepared from the blood samples of the volunteers.

Figures 32-37 show that the pixel intensity values of both u-RBCs and i-RBCs are high in the unstained blood smear slides prepared from the volunteers (Figures 35-37), hereafter, referred to as unstained slides, compared to those of the cultured stained slides (Figures 32-34), henceforth, referred to

147

as stained slides. The ratio of maximum light intensity transmitted through the *u*-RBCs and the *i*-RBCs for the unstained slides to the stained slides was 4:1. These observations may be as a result of the Giemsa dye acting as an additional absorber of the incident light, transmitting low intensities through the *u*-RBCs and the *i*-RBCs to the imager.
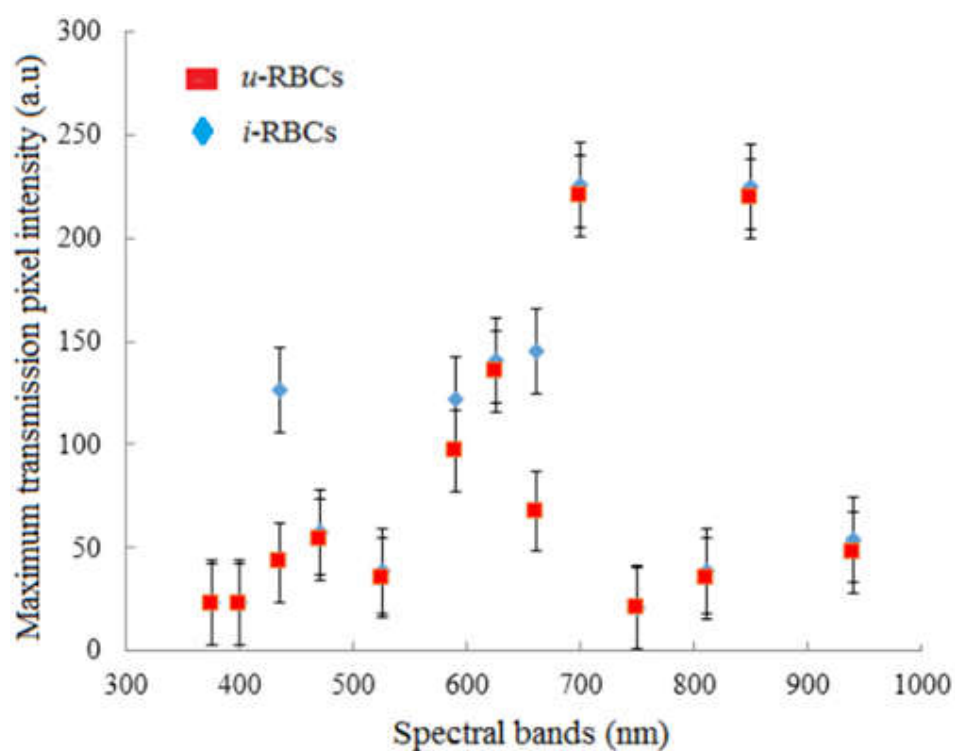
Figure 32: Maximum transmission grayscale pixel intensity values extracted from images of cultured blood smear slides stained with Giemsa dye. The images contain uninfected (*u*-RBCs) and *Plasmodium falciparum* infected RBCs (*i*-RBCs) in their ring stage.

148
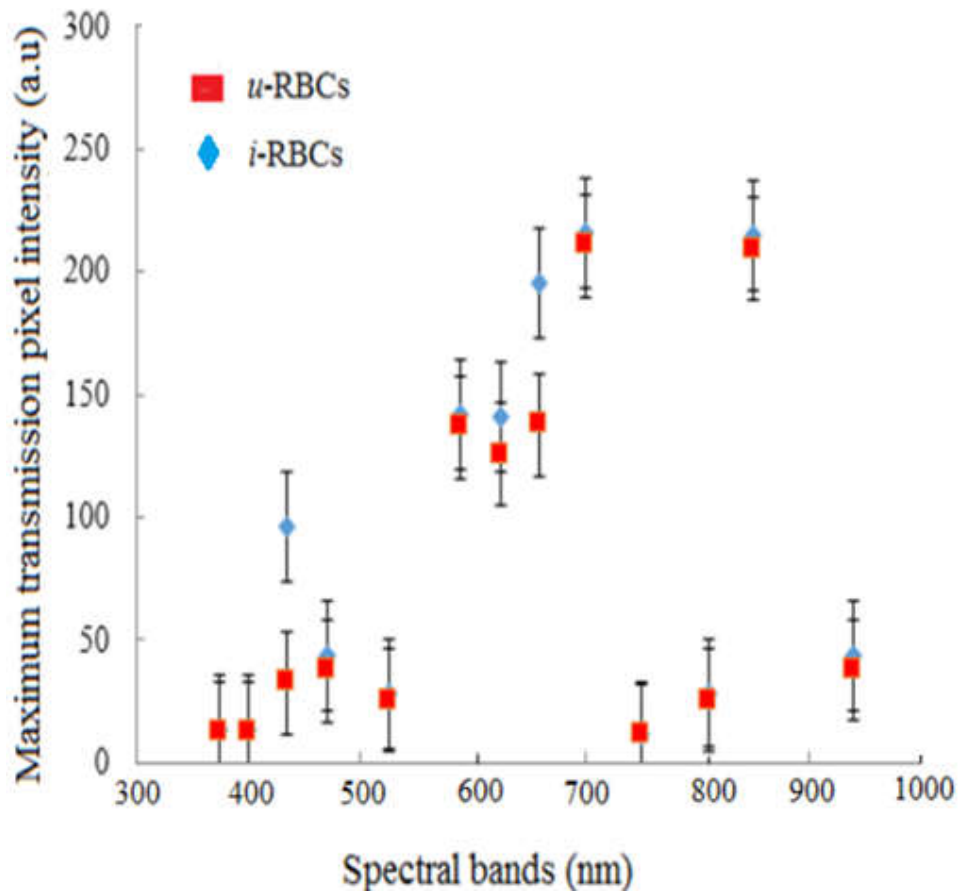
Figure 33: Maximum transmission grayscale pixel intensity values extracted from images of cultured blood smear slides stained with Giemsa dye. The images contain uninfected (*u*-RBCs) and *Plasmodium falciparum* infected RBCs (*i*-RBCs) in their trophozoite stage.

149
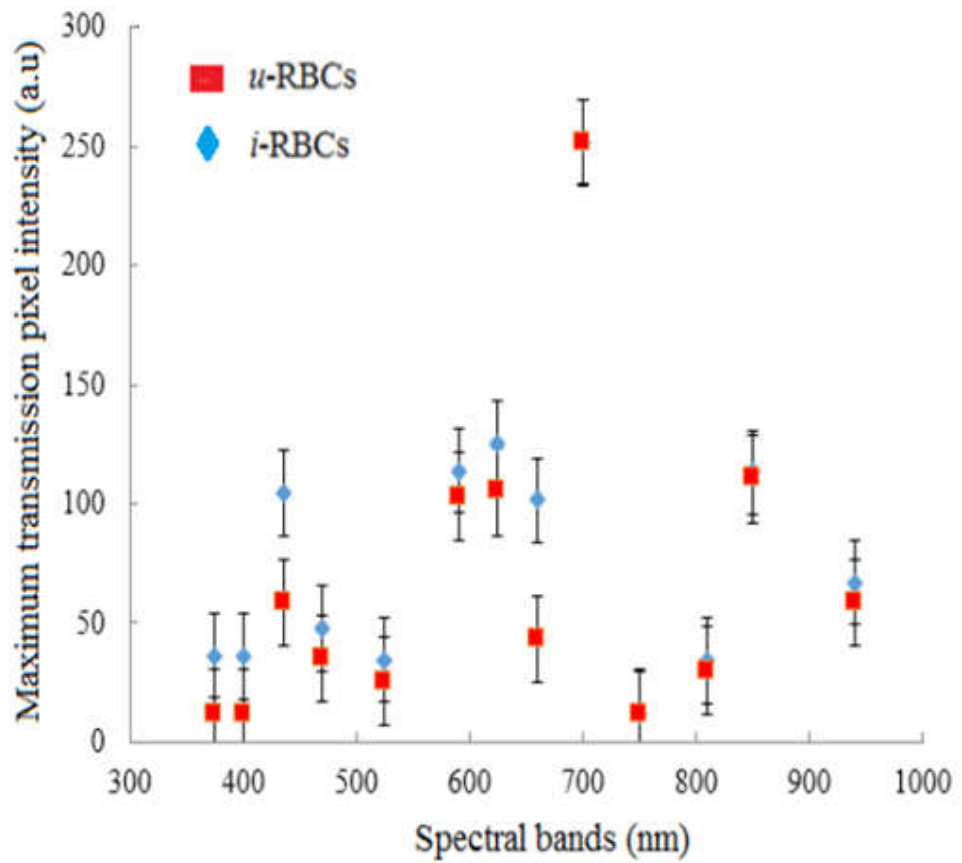
Figure 34: Maximum transmission grayscale pixel intensity values extracted from images of cultured blood smear slides stained with Giemsa dye. The images contain uninfected (*u*-RBCs) and *Plasmodium falciparum* infected RBCs (*i*-RBCs) in their schizont stage.

150
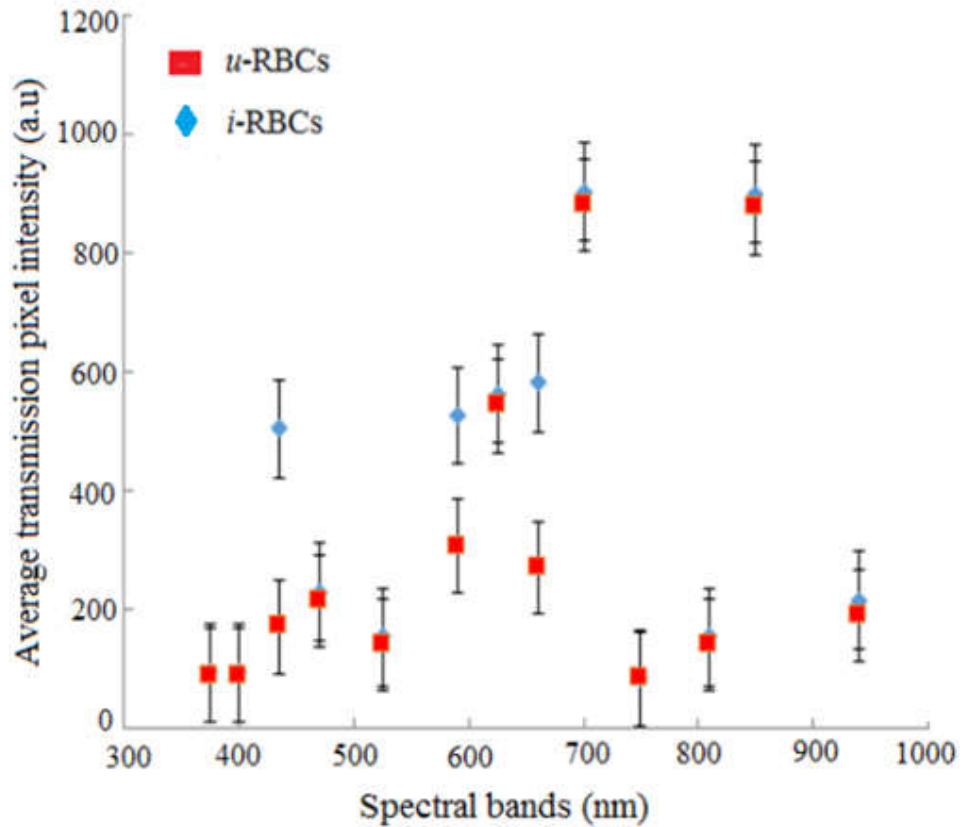
Figure 35: Average transmission grayscale pixel intensity values extracted from images of unstained blood smear slides prepared from the blood samples of the volunteers. The images contain uninfected (*u*-RBCs) and *Plasmodium falciparum* infected RBCs (*i*-RBCs) in their ring stage.

From Figure 35 (ring stage), it can be observed that the pixel intensity values for *i*-RBCs and *u*-RBCs are similar for some of the spectral bands as indicated by the error bars, and they are 375 nm, 400 nm, 470 nm, 525 nm and 700 nm. The rest are, 750 nm, 810 nm, 850 nm and 940 nm. These observations suggest that the light intensity transmitted through the *i*-RBCs and the *u*-RBCs at these spectral bands were similar. Low pixel intensity values were recorded at 375 nm, 400 nm, 525 nm and 750 nm for both *u*-RBCs and *i*-RBCs. Pixel intensity value below 100 a.u was used as the criterion. This suggests that there was high absorption at these spectral bands

151

(375 nm, 400nm, 525 nm and 750 nm) by Hb in both *u*-RBCs and *i*-RBCs. This resulted in low transmission of light intensity through the *u*-RBCs and the *i*-RBCs to the imager. There were small differences in the pixel intensity values between the *i*-RBCs and the *u*-RBCs at 470 nm, 525 nm, 700 nm, 810 nm, 850 nm and 940 nm. This can also be attributed to similar light intensity transmitted through the *i*-RBCs and the *u*-RBCs to the imager at these spectral bands.

Besides, in Figure 35, it can be observed that 435 nm, 590 nm and 660 nm spectral bands, show substantial differences in transmitted light intensity between the *i*-RBCs and the *u*-RBCs. Intensity difference of 100 a.u was used as the criterion. Similar observations occurred in the stained slides where 435 nm and 660 nm spectral bands showed significant intensity differences with 590 nm exhibiting slight differences. These observations in the unstained slides suggest that there was high Hb absorption in the *u*-RBCs at 435 nm, 590 nm and 660 nm. And that, these spectral bands are common spectral bands depicting intensity differences in the ring stage. Thus, the 435 nm, 590 nm and 660 nm spectral bands are seen as potential markers for identifying *u*-RBCs and *i*-RBCs in the ring stage.

152
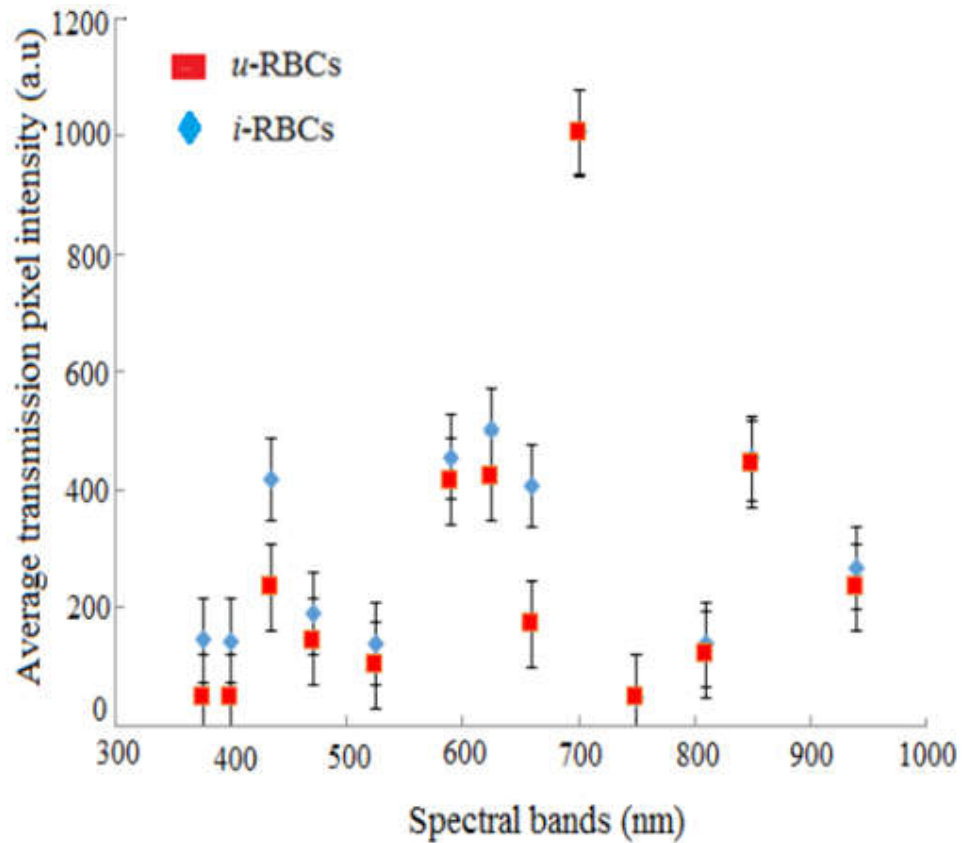
Figure 36: Average transmission grayscale pixel intensity values extracted from images of unstained blood smear slides prepared from the blood samples of the volunteers. The images contain uninfected (*u*-RBCs) and *Plasmodium falciparum* infected RBCs (*i*-RBCs) in their trophozoite stage.

Likewise, from Figure 36 (trophozoite stage), the pixel intensity values for *i*-RBCs and *u*-RBCs are similar for 700 nm, 750 nm and 850 nm spectral bands. This suggests that comparable light intensity was transmitted through the *i*-RBCs and the *u*-RBCs at these spectral bands. Low pixel intensities were recorded at 375 nm, 400 nm, 525 nm, 750 nm and 810 nm for both *u*-RBCs and *i*-RBCs. The same pixel intensity criterion of 100 a.u was used. This observation shows that there was high absorption at the 375 nm, 400 nm, 470 nm, 750 nm and 810 nm spectral bands by the Hb in the *u*-RBCs and the *i*-RBCs. Therefore, low light intensity of light was transmitted through the

153

u-RBCs and the *i*-RBCs to the imager. There were small differences in the pixel intensity values between the *i*-RBCs and the *u*-RBCs at 375 nm, 400 nm, 525 nm and 940 nm. This can also be attributed to similar light intensity transmitted to the *i*-RBCs and the *u*-RBCs at these spectral bands.

In addition, in Figure 36, it can be observed that 435 nm, 625 nm and 660 nm spectral bands, show noteworthy differences in transmitted light intensities between the *i*-RBCs and the *u*-RBCs. Again, pixel intensity difference of 100 a.u was used as a measure. In the stained slides, 435 nm and the 660 nm spectral bands showed significant intensity differences, with 625 nm showing minor differences. These observations indicate that there was low absorption of light in the *i*-RBCs at 435 nm, 625 nm and 600 nm. As a result, these three spectral bands are unique spectral bands that show intensity differences in unstained *i*-RBCs in the trophozoite stage. Hence, the 435 nm, 625 nm and 660 nm spectral bands are possible markers for identifying *u*-RBCs and *i*-RBCs in the trophozoite stage.
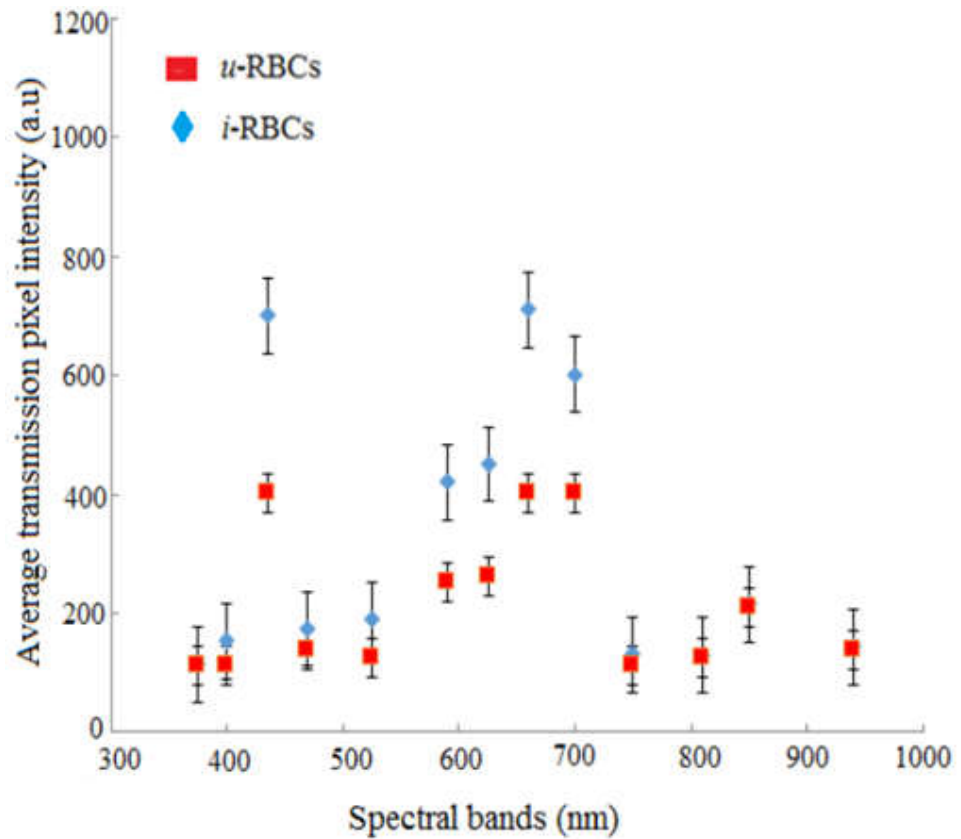
Figure 37: Average transmission grayscale pixel intensity values extracted from images of unstained blood smear slides prepared from the blood samples of the volunteers. The images contain uninfected (*u*-RBCs) and *Plasmodium falciparum* infected RBCs (*i*-RBCs) in their schizont stage.

In the same way, from Figure 37 (schizont stage), the spectral bands that show similar pixel intensity values for *i*-RBCs and *u*-RBCs are 375 nm, 810 nm, 850 nm and 940 nm. This observation may also be attributed to equal light intensity transmitted through the *i*-RBCs and the *u*-RBCs at these spectral bands. Low pixel intensity values for both *u*-RBCs and *i*-RBCs were recorded at 375 nm, 400nm, 470 nm, 525 nm, 750 nm, 810 nm and 940 nm. This also suggests that there was high absorption of light by Hb in the *u*-RBCs and the *i*-RBCs at spectral bands, transmitting low light intensity to the imager. There were also small differences in the pixel intensity values between

155

the *i*-RBCs and the *u*-RBCs at 400 nm, 470 nm, 525 nm and 750 nm. This can also be attributed to similar light intensity which was transmitted to the imager by *i*-RBCs and the *u*-RBCs at these spectral bands.

Furthermore, it can be observed from Figure 37 that, 435 nm, 590 nm, 625 nm, 660 nm and 700 nm spectral bands, show significant differences in transmitted light intensity between the *i*-RBCs and the *u*-RBCs. Yet again, pixel intensity difference of 100 a.u was used as the standard. Also in the stained slides, 435 nm and 660 nm depict significant differences with 590 nm and 625 nm showing slight disparities. These observations indicate that in the schizont stage and at these spectral bands, *u*-RBCs show absorption of light whilst the *i*-RBCs depict high transmitted light intensity. Therefore, 435 nm, 625 nm, 660 nm and 700 nm are mutual spectral bands showing intensity differences in the schizont stage. Hence, these spectral bands could be used as possible markers for identifying *u*-RBCs and *i*-RBCs in the schizont stage.

From Figures 35-37, it can be observed that high light intensity transmitted through the *i*-RBCs than the *u*-RBCs. This observation may be attributed to the fact that the *i*-RBCs more or less have their Hb either partially or completely digested together with their membrane proteins and membrane skeletal proteins by the parasite. The *i*-RBCs therefore become less dense and hence able to transmit more light to the imager (Goldberg et al., 1990; Moore et al., 2006). The intensity differences may also be due to the breakdown of Hb by the parasite, which digests and transports protein chain fragments in the *i*-RBCs.

In general, light transmission through the *u*-RBCs and the *i*-RBCs was determined by the optical properties of the *u*-RBCs and the *i*-RBCs. This

156

general case could be directly related to the amount of Hb being an important determinant of the light transmission. Light absorbance by the *u*-RBCs and the *i*-RBCs importantly contributed to the behaviour of the light passing through a suspension of these cells, with higher absorbance resulting in reduced light transmission. The amount of Hb was also an important determinant of light absorbance and, hence, the level of the light transmission. Absorption spectrum of Hb, with high molar extinction coefficient in the visible part of the EM spectrum, is clearly a critical factor for determining light transmission (Moore et al., 2006). The molar extinction coefficient was high for the Soret band and 660 nm spectral band. Thus, the absorbance of Hb was dependence on the spectral bands of the LED sources. This dependency explains the relationship between the level of light transmission through the *u*-RBCs and the *i*-RBCs at the spectral bands of the LED sources observed in this study. In all the three stages (ring, trophozoite and schizont), the presence of the hemozoin or the decrease of Hb in the *i*-RBCs increased the transmitted light intensity. Therefore, incident radiation in the Soret band and 660 nm spectral band was absorbed by *u*-RBCs with high Hb concentration.

The maximum pixel intensity values extraction procedure and the average pixel intensity values calculations for the *u*-RBCs and the *i*-RBCs were was also followed for the grayscale images for all the unstained slides captured at the 13 spectral bands in scattering and reflection modes. Figures 36-41 show plots of pixel intensity values of the *u*-RBCs and the *i*-RBCs extracted from the grayscale images of the slides with the ring stage, the trophozoite stage and the schizont stage of parasites against the 13 spectral

157

bands of the LED sources in scattering mode (Figure 36-38) and reflection mode (Figure 39-41).

Figures 36-41 show high scattered and reflected pixel intensity values in the *u*-RBCs than the *i*-RBCs in all the three stages. This observation could be attributed to less scattering and reduced reflection in the *i*-RBCs as the parasite develops throughout the 3 stages. And that, consumption of Hb by the parasite in the *i*-RBCs reduces the refractive index (RI) in the *i*-RBCs, affecting the scattered and the reflected light intensities in the *i*-RBCs within the three stages.

From Figure 38 (ring stage), the scattered pixel intensity values values were similar in the *i*-RBCs and the *u*-RBCs at 750 nm, 850 nm and 940 nm spectral bands. This observations may be attributed to even light intensity scattered through the *i*-RBCs and the *u*-RBCs at these spectral bands. All the spectral bands exhibit scattered pixel intensity values of the *i*-RBCs and the *u*-RBCs clustered between 20 a.u and 40 a.u. This observation could be due to the scattering of light of the same frequency to the imager through *u*-RBCs and the *i*-RBCs at these spectral bands. Minor differences in the pixel intensity values between the *i*-RBCs and the *u*-RBCs were observed at 375 nm, 400 nm, 525 nm, 700 nm and 810 nm. This may be as a result of similar light intensity scattered through the *i*-RBCs and the *u*-RBCs to the imager at these spectral bands.

Figure 38: Average scattering grayscale pixel intensity values extracted from images of unstained blood smear slides prepared from the blood samples of the volunteers. The images contain uninfected (*u*-RBCs) and *Plasmodium falciparum* infected RBCs (*i*-RBCs) in their ring stage.

It can also be observed from Figure 38 that, 435 nm, 470 nm, 590 nm, 625 nm and 660 nm spectral bands show differences in scattered pixel intensity values between the *i*-RBCs and the *u*-RBCs. Pixel intensity difference of 10 a.u was used as the standard. The 470 nm and the 660 nm show the major differences. These observations could be due to the scattering of hemozoin in the *i*-RBCs, which conspicuously showed decrease in scattered light intensity at 470 nm and 660 nm. And that, the 470 nm and 660 nm spectral bands could be used as the main potential markers for identifying

159

u-RBCs and *i*-RBCs in the ring stage with scattered light. The 435 nm, 590 nm and 625 nm spectral bands could also be used as alternative markers for the *u*-RBCs and the *i*-RBCs identification in the ring stage.

Figure 39: Average scattering grayscale pixel intensity values extracted from images of unstained blood smear slides prepared from the blood samples of the volunteers. The images contain uninfected (*u*-RBCs) and *Plasmodium falciparum* infected RBCs (*i*-RBCs) in their trophozoite stage.

From Figure 39 (trophozoite stage), the scattered pixel intensity values were similar in the *i*-RBCs and the *u*-RBCs at 750 nm, 850 nm and 940 nm. All the spectral bands in the trophozoite stage display scattered pixel intensity values of the *i*-RBCs and the *u*-RBCs clustered between 20 a.u and 40 a.u. These observations could also be due to the scattering of light of the same frequency to the imager through *u*-RBCs and the *i*-RBCs at these spectral

160

bands. There were minor differences in the scattered pixel intensity between the *i*-RBCs and the *u*-RBCs at 375 nm, 400 nm, 700 nm and 810 nm. This may be as a result of similar light intensity scattered through the *i*-RBCs and the *u*-RBCs to the imager at 375 nm, 400 nm, 700 nm and 810 nm.

Figure 39 also shows differences in scattered pixel intensity values between the *i*-RBCs and the *u*-RBCs at 435 nm, 470 nm, 525 nm, 590 nm, 625 nm and 660 nm. Pixel intensity difference of 10 a.u was used as a measure. Again, the 470 nm and the 660 nm show the main differences. These could also be as a result of the scattering of hemozoin in the *i*-RBCs, which obviously showed a decrease in scattered light intensities at 470 nm and 660 nm. And that, in the trophozoite stage, and with scattered light, 470 nm and 660 nm could be used as major potential markers for identifying *u*-RBCs and *i*-RBCs. The 435 nm, 525 nm, 590 nm and 625 nm spectral bands could also be used as other markers for the *u*-RBCs and the *i*-RBCs identification.

With scattered light, the schizont stage (Figure 40) shows the most significant disparities. There was low intensity of the scattered light through the *u*-RBCs and the *i*-RBCs at 375 nm. The scattered pixel intensity values suddenly increased at 400 nm, and is maintained at all the spectral bands and decreased again at 850 nm to 940 nm. Besides, all the spectral bands, except 375 nm, 850 and 940 nm, depict scattered pixel intensity values of the *u*-RBCs and the *i*-RBCs clustered between 30 a.u and 45 a.u. These observations could be due to weak backscattered light through the *u*-RBCs, and the *i*-RBCs at 375 nm, 850 nm and 940 nm. And that, the *u*-RBCs and the *i*-RBCs appeared dimmer to the imager at 375 nm, 850 nm and 940 nm.
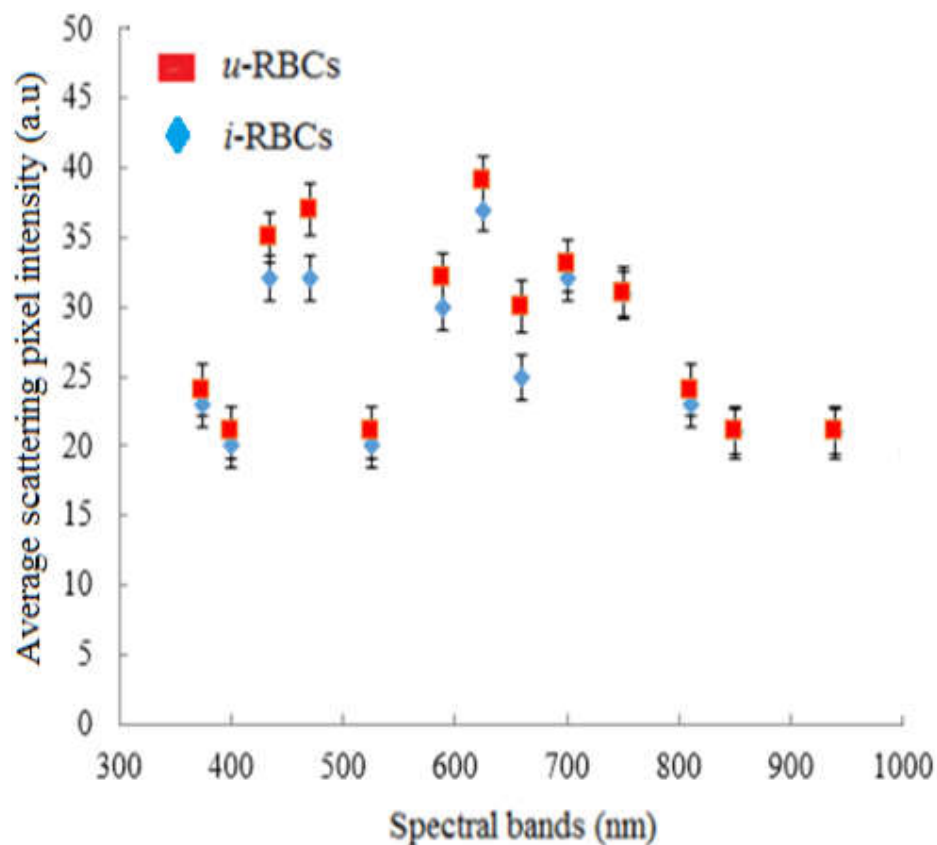
Figure 40: Average scattering grayscale pixel intensity values extracted from images of unstained blood smear slides prepared from the blood samples of the volunteers. The images contain uninfected (*u*-RBCs) and *Plasmodium falciparum* infected RBCs (*i*-RBCs) in their schizont stage.

To add to that, six spectral bands: 435 nm, 470 nm, 525 nm, 590 nm, 625 nm and 660 nm, with pixel intensity difference of 10 a.u, show variations in the scattered pixel intensity values between the *u*-RBCs and the *i*-RBCs. This is more conspicuous in 470 nm and 660 nm. These observations may be attributed to the RI drop in the *i*-RBCs which becomes more significant in the schizont stage with reduced scattering in the *i*-RBCs at the 470 nm and the 660 nm. Therefore, the 470 nm and the 660 nm spectral bands could be used as key potential markers for identifying *u*-RBCs and *i*-RBCs in the schizont stage. The 435 nm, 525 nm, 590 nm and 625 nm spectral bands could also be

162

used as additional markers for the *u*-RBCs and the *i*-RBCs identification in the
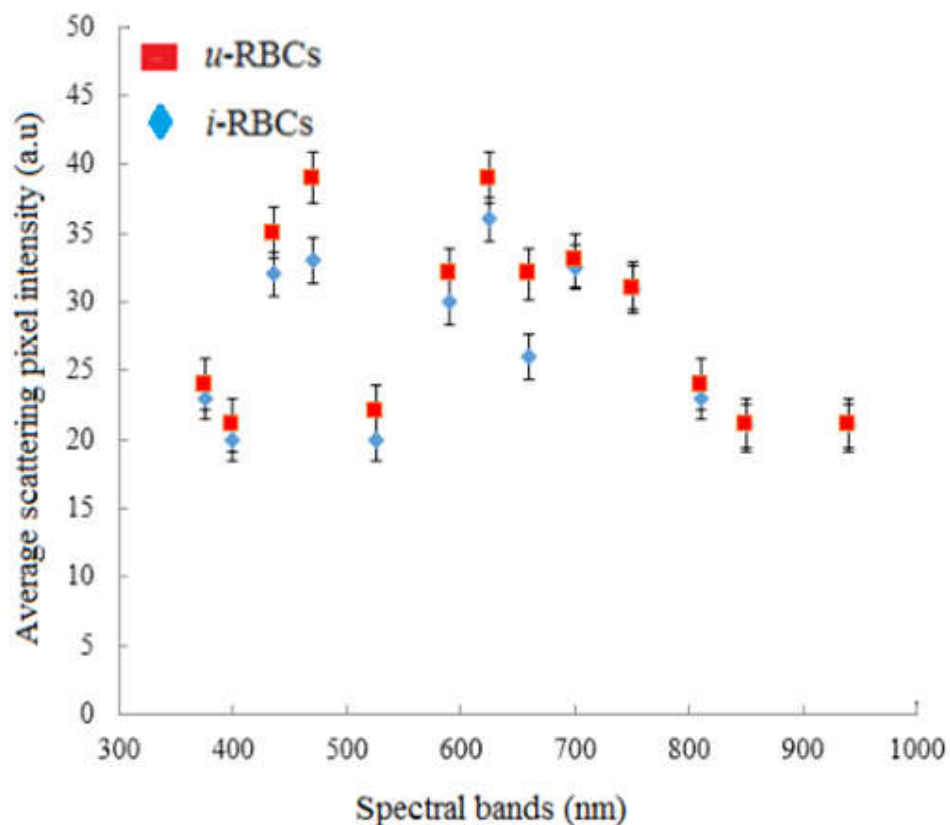
schizont stage.
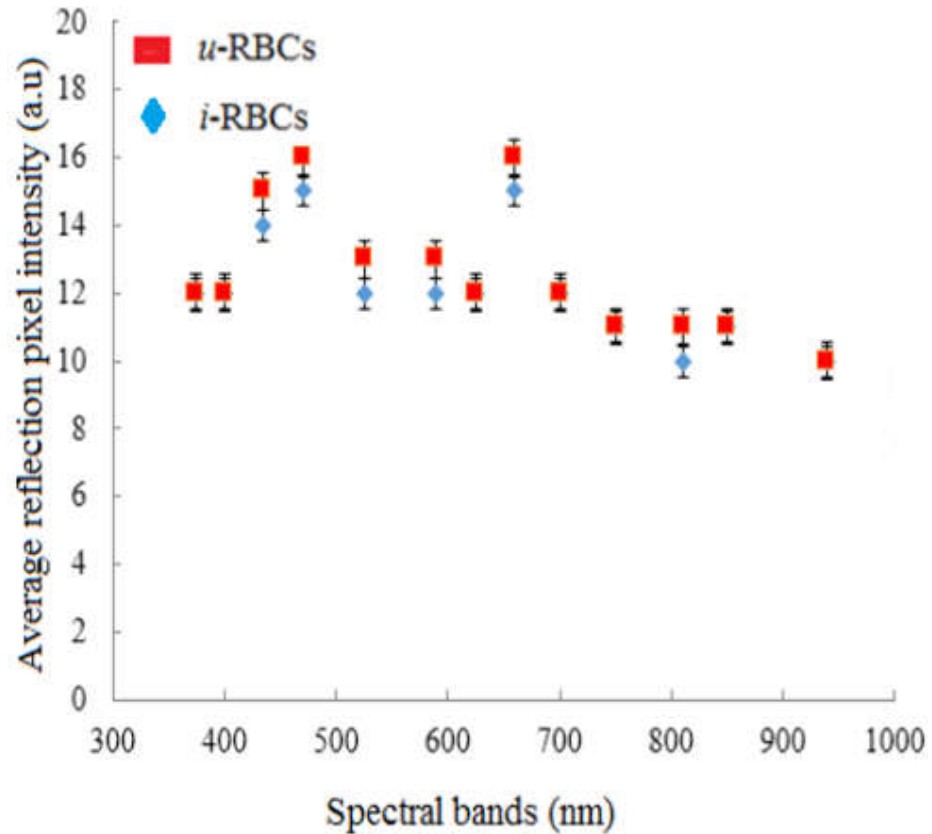
Figure 41: Average reflection grayscale pixel intensity values extracted from images of unstained blood smear slides prepared from the blood samples of the volunteers. The images contain uninfected (*u*-RBCs) and *Plasmodium falciparum* infected RBCs (*i*-RBCs) in their ring stage.

From Figure 41, that is, the ring stage in reflection mode, there is little

variations in the reflected pixel intensity values between the *u*-RBCs and the

i-RBCs. All the 13 spectral bands show minimum reflected pixel intensity

values, and the *u*-RBCs and the *i*-RBCs appear clustered within reflected pixel

intensity values of 12 a.u and 16 a.u. These observations may be attributed to

uniform reflected light intensity through the *u*-RBCs and the *i*-RBCs at all the

13 spectral bands. And that, with reflected pixel intensity values between 12

163

a.u and 16 a.u, both *u*-RBCs and *i*-RBCs exhibit similar characteristics. Five spectral bands show minor differences between the *u*-RBCs and the *i*-RBCs. The spectral bands are: 435 nm, 470 nm, 525 nm, 590 nm and 660 nm. Besides, there was slightly high diffuse reflection in the *i*-RBCs due to the rigidity of the *i*-RBCs as result of the presence of the parasite. This resulted in a reduction of reflected light intensity at the 435 nm, 470 nm, 525 nm, 590 nm and 660 nm spectral bands. The results also show that these 5 spectral bands may offer potential diagnostic markers for identifying the *u*-RBCs and the *i*-RBCs with reflected light at the ring stage.

The reflected light on the *u*-RBCs and the *i*-RBCs in the trophozoite stage (Figure 42) depict low pixel intensity values in the NIR region of the EM spectrum (750 nm, 810 nm, 850 nm and 940 nm). This observation may be as a result of these spectral bands (750 nm, 810 nm, 850 nm and 940 nm) showing weak reflected light intensity in the *u*-RBCs and the *i*-RBCs. At 435 nm, 470 nm and 660 nm, the *u*-RBCs and the *i*-RBCs show significant differences. These indicate that the light intensity reflected onto the imager was high in the *u*-RBCs than the *i*-RBCs. These findings could also mean that there was high backscattering of light by the *u*-RBCs than the *i*-RBCs. The weak backscattered light by the *i*-RBCs was due to their structural rigidity. Hence, at the spectral bands (435 nm, 470 nm and 660 nm), and in the trophozoite stage, the *u*-RBCs show high backscattering whilst the *i*-RBCs depict weak diffuse reflection characteristics indicating that these three spectral bands are unique markers for identifying the *u*-RBCs and the *i*-RBCs with reflected light.
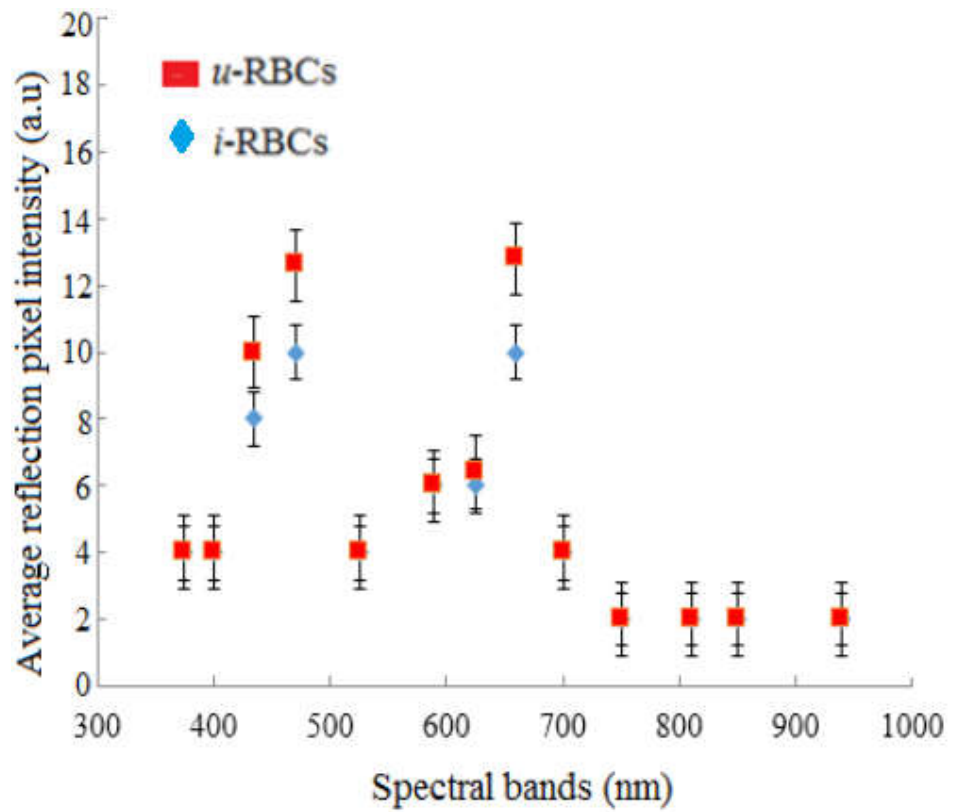
Figure 42: Average reflection grayscale pixel intensity values extracted from images of unstained blood smear slides prepared from the blood samples of the volunteers. The images contain uninfected (*u*-RBCs) and *Plasmodium falciparum* infected RBCs (*i*-RBCs) in their trophozoite stage.
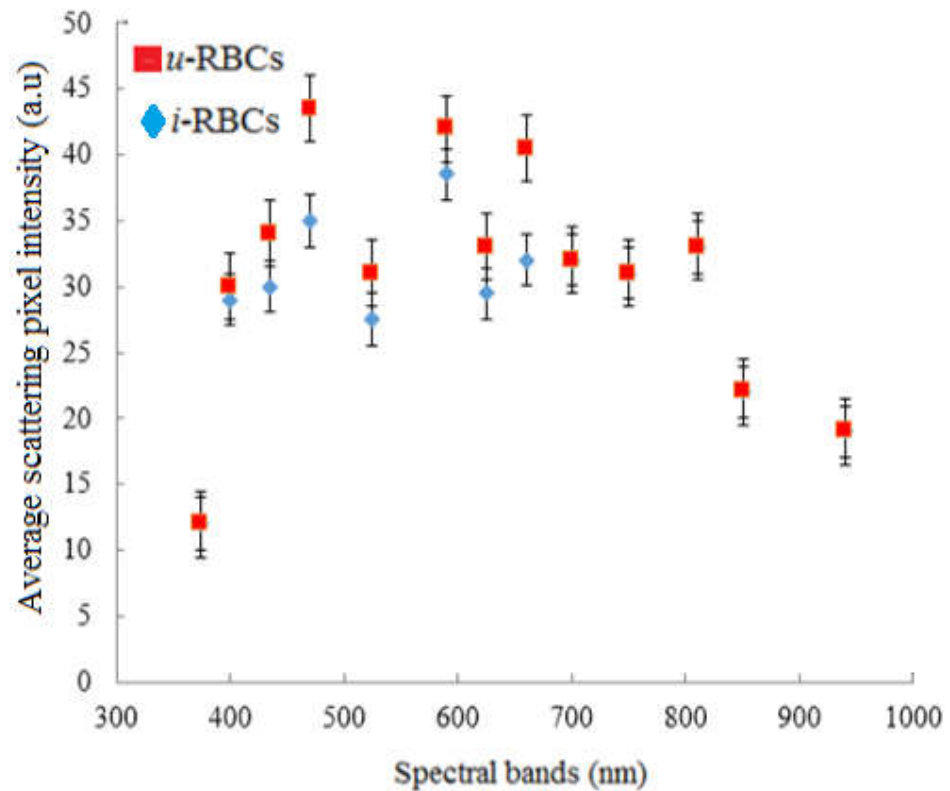
165
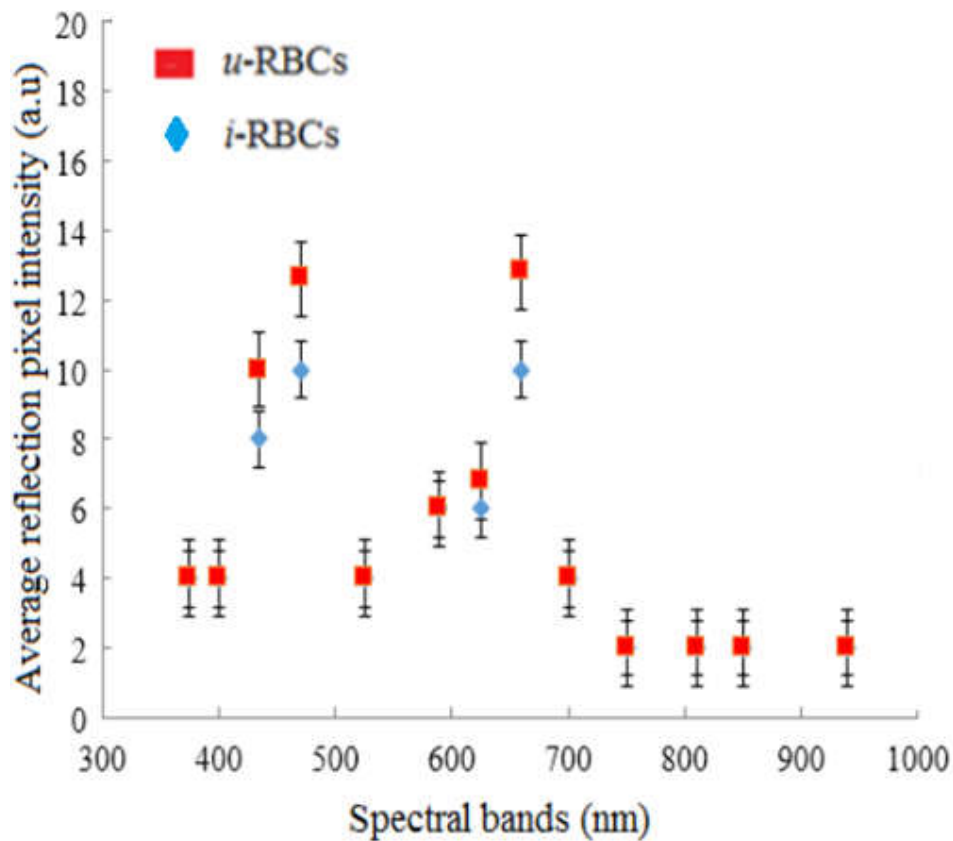
Figure 43: Average reflection grayscale pixel intensity values extracted from images of unstained blood smear slides prepared from the blood samples of the volunteers. The images contain uninfected (*u*-RBCs) and *Plasmodium falciparum* infected RBCs (*i*-RBCs) in their schizont stage.

Figure 43 (schizont stage) show similar optical characteristics trends as the trophozoite stage. Here too, the reflected light on the *u*-RBCs and the *i*-RBCs depict low reflected pixel intensity values at the NIR, suggesting reduced backscattering of the light intensity on the *u*-RBCs and the *i*-RBCs in the NIR region. At 435 nm, 470 nm, 625 nm and 660 nm, the *u*-RBCs and the *i*-RBCs show important differences. These also indicate that the light intensity reflected onto the imager was high in the *u*-RBCs than the *i*-RBCs. And that, these results could also suggest that the *u*-RBCs backscattered the light than the *i*-RBCs. Hence, the 435 nm, 470 nm, 625 nm and 660 nm spectral bands

166

are unique markers for identifying the *u*-RBCs and the *i*-RBCs with reflected light in the schizont stage.

It has been predicted in this work that during the intraerythrocytic life cycle stages of *P.falciparum* development, which starts with the ring stage, followed by the trophozoite stage and culminated with the schizont stage as a result of the growth of the parasite, variations in the optical characteristics of the *u*-RBCs and the *i*-RBCs occurred during this development. Therefore, the appreciable changes in the spectral features was expected. The average pixel intensity extraction procedure was designed to study the spectral features of the *u*-RBCs and the *i*-RBCs at the different stages of the parasite's development. Furthermore, the potential variability in the spectral features of the *u*-RBCs and the *i*-RBCs at each stage and reproducibility of the pixel intensity extraction procedure, can also be appreciated with independent spectral signatures of the *u*-RBCs and the *i*-RBCs.

Generally, light intensity through the *u*-RBCs and the *i*-RBCs at all the 13 spectral bands was high in transmission mode, a little low in scattering mode and very low in reflection mode. In percentages, and with reference to the incident light, there was about 80 % transmission, 10 % scattering, 7 % reflection and the remaining 3 % could be attributed to absorption. Therefore, based on the theory that A+R+S+T = 1, and assuming that A = 0, it can be established in this work that $T \leq 1-(R+\rho)$, since S is a diffuse reflection phenomenon and ρ is a constant. The number and the size of the hemozoin crystals in the *i*-RBCs depended on the stage of the parasite development, with the least amount of the hemozoin detected in the ring stage and the highest amount in the schizont stage.

To further the analysis on the average pixel intensity data in transmission mode, principal component analysis (PCA) was performed using developed Matlab codes. This was to classify the *i*-RBCs into ring, trophozoite and schizont stages. In performing the PCA, light intensity extracted from the spectral images captured at 435 nm and 660 nm were used. The PCA plot was used to determine the number of principle components (PCs) appropriate for the classification. The PCA reduces the dimensionality of variables, which are the light intensity values at the 13 spectral bands. Before the PCA was done, the transmitted light intensity data for all the 13 spectral bands representing the *u*-RBCs and the *i*-RBCs in all the three stages were combined and a scree plot (Figure 44) that best explains the PCs to be selected was done. The scree plot was done with the 13 spectral bands as variables and 1024 light intensity values as observations, forming 13 x 1024 data points. Martinez and Martinez have suggested that in scree plotting, the point where the points in the curve levels off and becomes almost flat are the ideal PCs (Martinez & Martinez, 2005). The eigenvalues drops off rapidly after the third PC. This suggests that the first three PCs are appropriate for PCA.
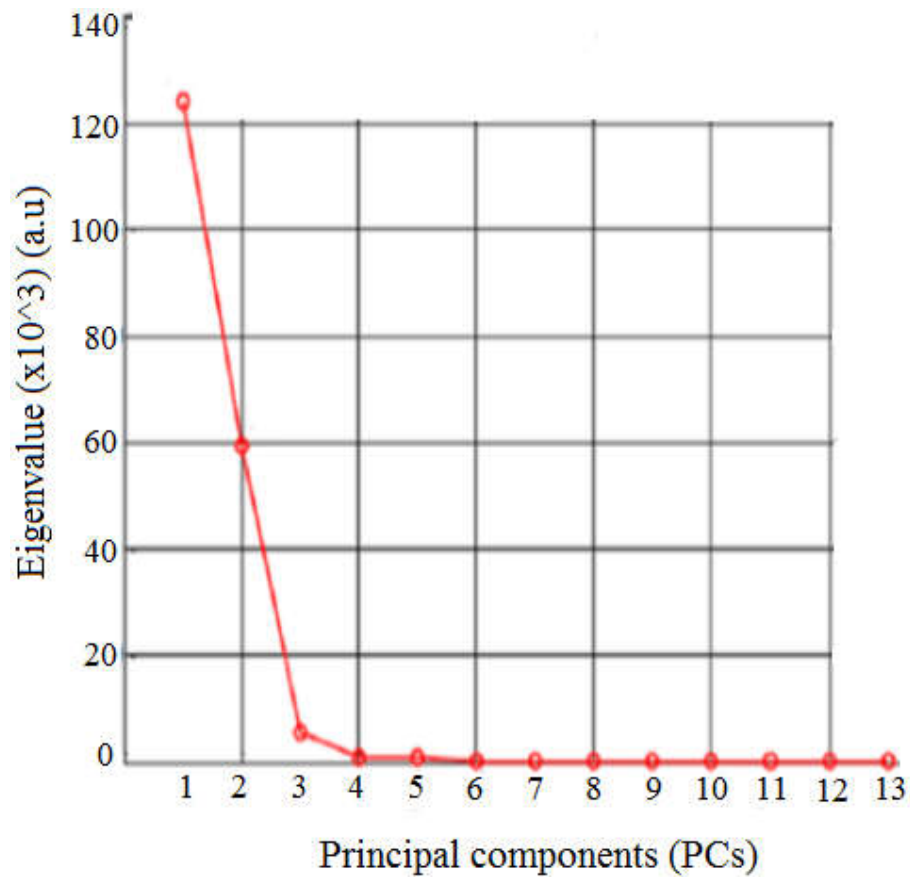
Figure 44: A scree plot indicating the eigenvalues of the principal
        components (PCs), which represent the weights of each PC.

The three PCs (PC1, PC2 and PC3) retained the maximum variations
in the transmitted light intensity data with 96.5 % cumulative variability. Out
of the 96.5 % variability in the transmitted light intensity data, PC1
contributed 63.8 %, PC2 29.8 % and PC3 2.9 %. The PCs are proportional to
the transmitted light intensity from the *i*-RBCs and the *u*-RBCs. The first PC
(PC1) is the linear combination of the intensity data with maximum variance,
PC2 is the linear combination of the next maximum variance orthogonal to
PC1. PC3 is the linear combination of the third maximum variance orthogonal
to both PC1 and PC2 in that order. Based on the results from the PCA, the 3
PCs containing the average transmitted light intensity data extracted from the

169

u-RBCs and the *i*-RBCs at 435 nm and 660 nm were combined for cluster analysis. A dendrogram representing the average intensity data for both *i*-RBCs and *u*-RBCs is shown in Figure 45.
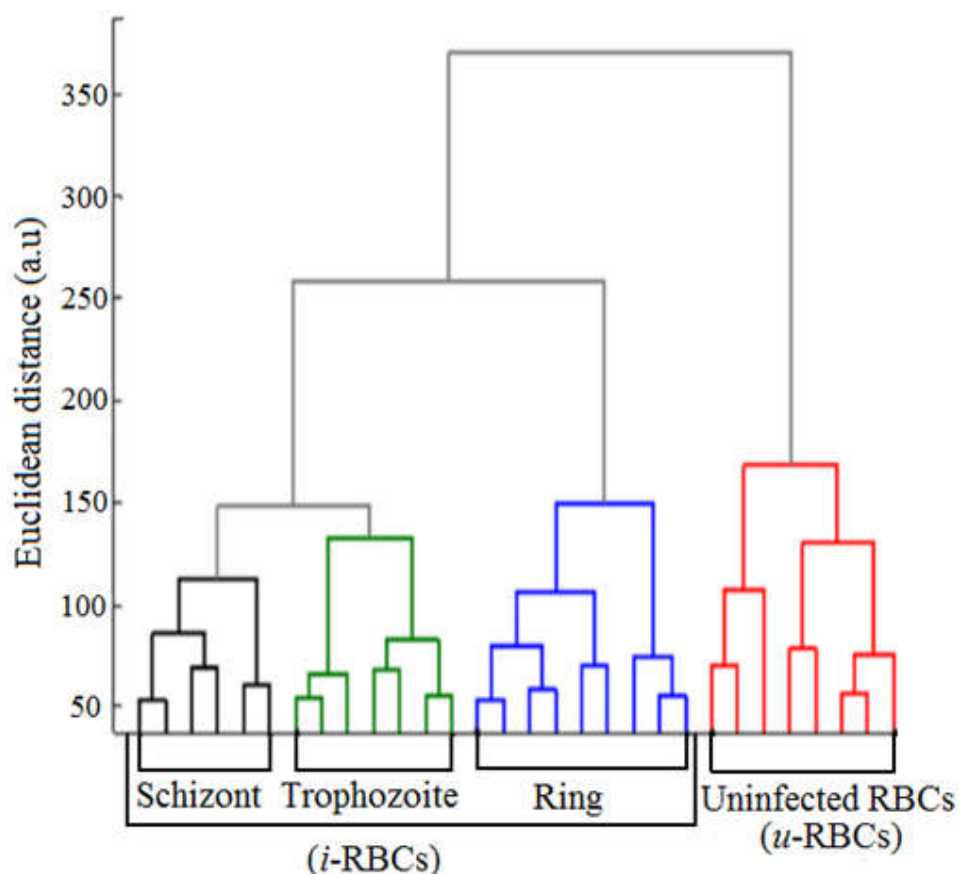
Figure 45: A dendrogram representing intensity values of uninfected RBCs (*u*-RBCs) (red colour) and *Plasmodium falciparum* infected RBCs (*i*-RBCs) in the intraerythrocytic stages: ring (blue colour), trophozoite (green colour) and schizont (black colour).

From Figure 45, it can be deduced that there are four main clusters representing the intensities of both *i*-RBCs and *u*-RBCs. Cluster 1 (*u*-RBCs) is made up of two sub-clusters. The first sub-cluster of cluster 1 consists of five leaf nodes and the second sub-cluster of cluster 1 consists of three leaf nodes. In addition, cluster 2 (ring stage) has two sub-clusters made of three and five leaf nodes for sub-cluster 1 and sub-cluster 2 respectively. Besides, cluster 3

170

(trophozoite stage) contains three sub-clusters with the first sub-cluster having four leaf nodes and the second sub-cluster with two leaf nodes. Finally, Cluster 4 (schizont stage) has two sub-clusters with the first sub-cluster having two leaf nodes and the second sub-cluster with three leaf nodes. Also, from figure 46, it can be observed that the sub-clusters of *u*-RBCs are joined at a higher distance than the sub-clusters of *i*-RBCs. This distance of the sub-clusters reduces in *i*-RBCs in the intraerythrocytic life cycle stages of development of the parasites. These observations may be attributed to low and, or uniform transmitted light intensity values of *u*-RBCs as compared to the intensity values of *i*-RBCs. The formation of four clusters in the dendrogram indicates intensities of *i*-RBCs and *u*-RBCs for the two spectral bands 435 nm and 660 nm used for the dendrogram. This is because each of the two spectral bands formed a cluster of *i*-RBCs and a cluster of *u*-RBCs. Finally, the four clusters were joined together to form a single cluster because they represent intensities of RBCs.

Fluorescence Imaging

Two grayscale images containing the *u*-RBCs and the *i*-RBCs obtained from the multi-functional imaging microscope (MFIM) using 405 nm laser as illumination source are shown in Figure 46. The choice of this illumination laser source was because it shows high Hb absorption spectra (Goldberg et al., 1990; Moore et al., 2006). Figure 46(a) and (b) show images of *i*-RBCs and *u*-RBCs interspersed in a non-uniform background without fluorescence and with fluorescence respectively.

171

(a)   (b)
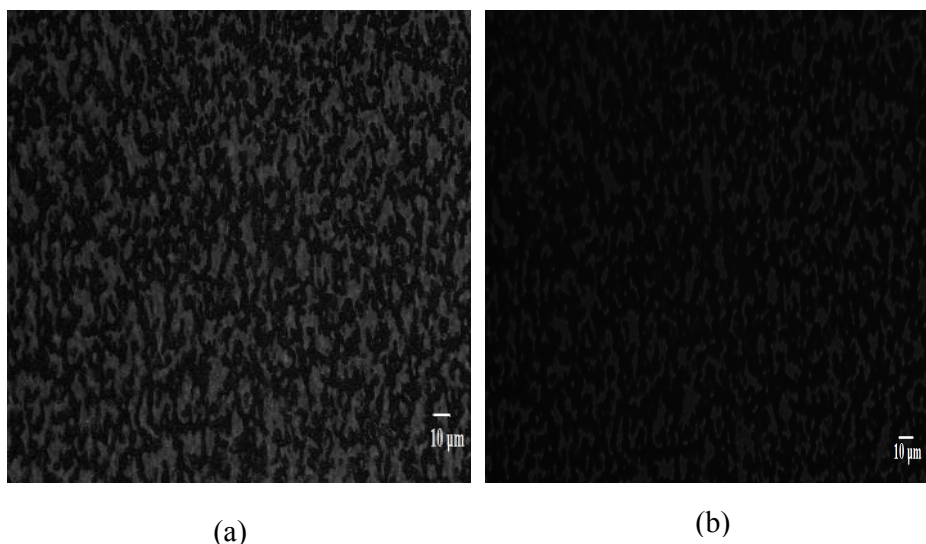
Figure 46: Two grayscale images acquired using multi-functional imaging
microscope (MFIM) at 405 nm laser illumination sources. The
images show infected and uninfected red blood cells exhibiting (a)
non-fluorescence and (b) fluorescence.

Figure 46(a) and (b) show pixel properties with distinct disparities in

the images. It can be observed from Figure 46(a) (no fluorescence image) that

some RBCs show dark spots in the centre and shades of white spots in the

periphery indicating the *u*-RBCs. Others also show shades of white spots in

the centre and dark regions in the periphery suggesting the *i*-RBCs. In Figure

46(b) (fluorescence image), the *u*-RBCs appear in shades of white both in the

centre and the periphery whilst the *i*-RBCs seem to appear as dark spots in the

centre and the periphery with some holes in them. This observation indicates

that the *u*-RBCs absorbed most of the incident light due to their high Hb

content. The high absorption of Hb by the *u*-RBCs triggered high fluorescence

light intensity in the *u*-RBCs. The *i*-RBCs with low Hb content showed little

fluorescence due to their low absorption and/or high transmission

characteristics. Therefore, the *u*-RBCs appear as shades of white and the

172

i-RBCs as dark spots in fluorescence light.

The fluorescence images were imported into Matlab platform for processing and analysis. Figure 47 summarizes the procedure for fluorescence image processing and analysis in a structured flowchart.
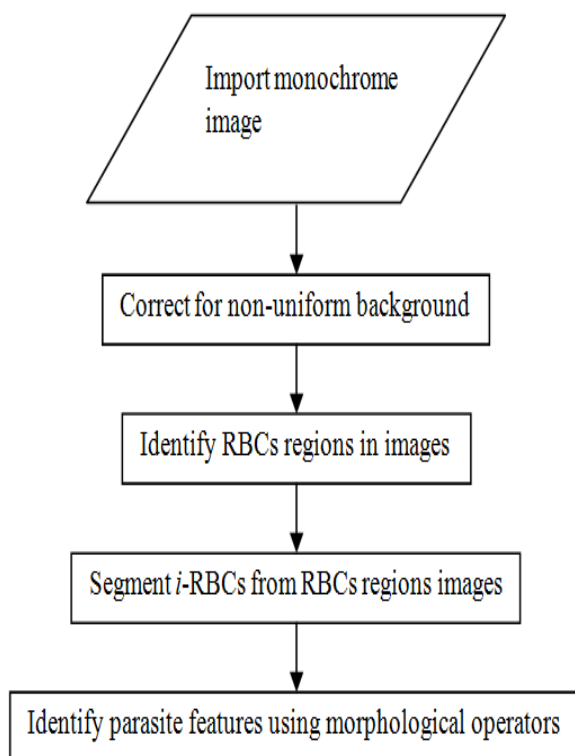
Figure 47: Structured flowchart for processing and analyzing fluorescence images containing uninfected red blood cells (*u*-RBCs) and *Plasmodium falciparum* infected red blood cells (*i*-RBCs).

The fluorescence image shows the *i*-RBCs and the *u*-RBCs in a non-uniform background. To remove this low frequency signal from the image, the size of the image was reduced by saving the rows and columns in the original image. Morphological opening with disk-shaped structuring element was operated on the image. The opened image was then filtered using a Gaussian filter to blur out sharp edges that might have resulted from the opening operation. The filtered image was resized to its original size.

173

The *u*-RBCs and the *i*-RBCs regions had distinct gray-level characteristics compared to dark background around them. To improve the image segmentation, the *u*-RBCs and the *i*-RBCs regions were segmented first. This was done using histogram-based thresholding algorithm (Otsu, 1979) applied to the background illumination pattern. Binary morphological operators were then used to ensure that the enclosed regions with distinctly different sizes and shapes from those of the *u*-RBCs and the *i*-RBCs were removed. Smoothing algorithm was used to eliminate irregularities along the contours of the *u*-RBCs and the *i*-RBCs.

To identify the parasites in the *i*-RBCs, connected-component labeling was performed, labeling each of parasites with the same label. Binary mask was generated where the value 1 represented the area where parasites were present and 0 corresponded to the background. All pixels outside the given range were not included in the parasites segmentation. In order to use morphological methods for parasites identification, the shape and size of the parasites in the image were considered. A disk- shape structural element of radius 2 pixels was chosen and applied onto the filled regions in the image in order to obtain regions where the parasites were located (Sio et al., 2006).

Morphological opening by the structuring element, followed by dilation of the result, was then applied on the image. Ball-shape structuring element of radius 6 pixels and height 2 pixels were then applied on the resulted image. The extent of thickening was controlled by structuring the element shape. The parasites were equated to the dilated image and labeled using a binary labeling system. Figure 48 shows the resulted image depicting

174

P.falciparum parasites after thresholding, morphological operation and dilation.
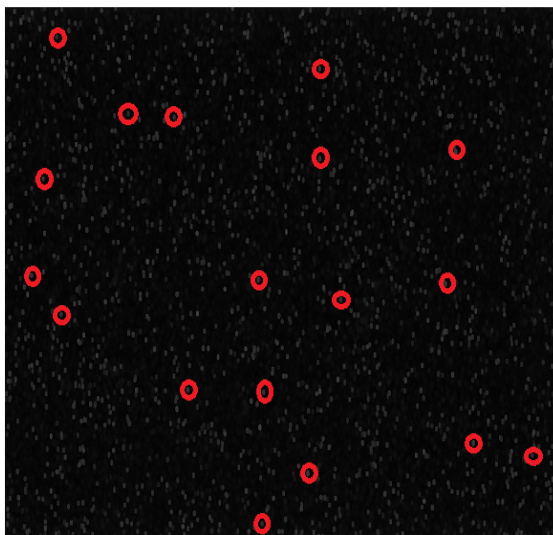
Figure 48: Image showing some identified *Plasmodium falciparum* (*P.falciparum*) parasites (circled) and outliers (not circled) after binary labeling, thresholding, morphological operation and dilation.

Figure 48 shows some identified parasites (circled) and outliers (not circled). Some of the outliers may be classified as parasites but could not be identified due to the limitation of the developed algorithm. From Figure 48, some of the identified parasites appear double and uneven. This might be attributed to image dilation by the disk shape structuring element. The image dilation grew and thickened the identified parasites in the images. This can be attributed to a feature of the parasites in their early developmental stages. The early stage of the parasite generally appears in a form of chromatin dot and a cytoplasm.

175

CHAPTER FIVE

SUMMARY, CONCLUSION AND RECOMMENDATIONS

Summary and Conclusion

In this research work, three optical techniques have been used to study and characterize uninfected red blood cells (*u*-RBCs) and *Plasmodium falciparum* (*P.falciparum*) infected red blood cells (*i*-RBCs) on unstained blood smear slides prepared from uninfected blood (*u*-blood) samples and *P.falciparum* infected blood (*i*-blood) samples collected from volunteers. The *i*-blood samples were grouped based on parasite densities (PDs) (+, ++, +++, ++++) and intraerythrocytic life cycle stages: ring, trophozoite and schizont. The applied optical techniques are laser-induced fluorescence (LIF), spectrophotometry and spectral imaging (SI). In addition, a fourth optical technique using a multi-functional imaging microscope (MFIM) has been assembled and tested for the *i*-RBCs detection using fluorescence imaging technique.

Employing the LIF technique, the *u*-blood samples showed high fluorescence intensity than the *i*-blood samples. PeakFit analysis in combination with Loess smoothing of the fluorescence spectra fitted with Lorentzian curve showed that the fluorescence spectra peak intensity of the *i*-blood samples exhibited red-shifted phenomenon with increasing PDs. The mean fluorescence spectra peak wavelength for the *u*-blood samples was 610.80 nm, and that for the *i*-blood samples were: 611.65 nm, 612.05 nm, 613.14 and 613.22 nm for PDs of +, ++, +++ and ++++ respectively. The

176

Lorentzian curves depicted that increase in PDs in the *i*-blood samples increase fluorescence spectra peak intensity ratio (PIR). The mean PIR for the *u*-blood was found to be less than 0.3 and that of the *i*-blood were in the range of 0.4 to 1.2. The LIF technique concludes that there is energy lost as a result of the growth of the parasite in the *i*-blood samples. Hence, fluorescence spectra peak wavelengths of the *i*-blood samples shift to longer wavelengths with increasing PDs.

Using the spectrophotometry technique, optical densities (ODs) of the *u*-blood samples and the *i*-blood samples at Soret band (S-band) (405 nm), β-band (541 nm) and α-band (577 nm) showed different blood absorption characteristics. At the S-band, ODs of the *u*-blood samples relative to the ODs of the *i*-blood samples ($OD_{R(S-band)}$) showed that increase in the ODs corresponded to increasing PDs in the *i*-blood samples. The ratio of the β-band to the α-band ODs ($OD_{(\beta/\alpha)}$) for the *u*-blood samples was 0.90, and this value reduced by about 2.3 % as compared to a literature value of 0.92. That for the *i*-blood samples showed decreased ODs with increasing PDs. The $OD_{(\beta/\alpha)}$ for the *i*-blood was 0.79, 0.68, 0.60 and 0.40 for PDs +, ++, +++ and ++++ respectively. These $OD_{(\beta/\alpha)}$ values of the *i*-blood samples compared to that of the *u*-blood samples (0.90) correspondingly decreased by 10.75 %, 21.35 %, 29.32 % and 49.84 % for PDs +, ++, +++ and ++++. The spectrophotometry technique establishes that haemoglobin (Hb) reduces drastically as the number of parasites increases in the the *i*-blood samples.

By means of SI technique, PDs could be determined from the *i*-RBCs. Spectral images containing the *i*-RBCs on unstained blood smear slides

177

acquired from a multispectral light-emitting diode imaging microscope (MSLEDIM) in reflection, scattering and transmission modes showed that the spectrally determined light intensity increased in transmission, and decreased in scattering and reflection properties of the *i*-RBCs. These variations in spectral light intensities corresponded to increasing PDs in the *i*-RBCs. Histograms fitted with Gaussian curve showing geometrical and optical parameters: aspect ratio (AR) and integrated optical density (IOD) retrieved from the *u*-RBCs and the *i*-RBCs showed that the *u*-RBCs have $AR < 1.2$ and $IOD < 2000$ a.u. The *i*-RBCs depicted average AR values of 1.5, 1.7, 1.9, 2.0 for PDs of +, ++, +++ and ++++ respectively. The average IOD values for the respective PDs are 5000, 7000, 9000 and 13000 a.u.

Using extracted pixel intensity from the *u*-RBCs and the *i*-RBCs, seven spectral bands in all, consisting of 435 nm, 470 nm, 525 nm, 590 nm, 625 nm, 660 nm and 700 nm, were found to be markers for identifying the *u*-RBCs and the *i*-RBCs at ring, trophozoite and schizont stages. Two spectral bands (435 nm and 660 nm) were common markers for the three stages in reflection, scattering and transmission modes. These two spectral bands showed significant differences between the *u*-RBCs and the *i*-RBCs at the three stages in all the three modes. In both reflection and scattering modes, an additional spectral band (470 nm) was found as a common marker for identifying the *u*-RBCs and the *i*-RBCs in the three stages of the parasite whilst 525 nm, 590 nm and 625 nm were unique spectral band-markers with slight disparities for the identification of the *u*-RBCs and the *i*-RBCs in the ring stage, the trophozoite stage and the schizont stage respectively. In transmission mode, whether the *i*-RBCs is in the ring, the trophozoite or the schizont stages can be

significantly identified from the *u*-RBCs by single markers namely 590 nm, 625 nm and 700 nm respectively. These spectral bands may offer potential diagnostic markers for identifying the *u*-RBCs and the *i*-RBCs, as well as distinguishing ring, trophozoite and schizont stages. Conclusion on the SI technique shows that PDs estimation and identification of the *i*-RBCs in the intraerythrocytic life cycle stages (ring, trophozoite and schizont) can best be studied with transmitted light intensity at unique spectral bands.

By means of fluorescence imaging (FI), the *u*-RBCs appear in shades of white both in the centre and in the periphery whilst the *i*-RBCs seem to appear as dark spots in the centre and in the periphery with some holes in the *i*-RBCs. Developed Matlab code based on the morphological features of the parasites in the *i*-RBCs showed some limitations with some outliers being identified as parasites. The FI technique reveals that optical contrast can be established between the *u*-RBCs and the *i*-RBCs in a staining-free analysis.

The applied optical techniques could be potentially used for improved *P.falciparum* diagnosis, effective control and management of malaria patients. Understanding the spectral changes in the degradation of haemoglobin may offer new targets for anti-malarial drug treatments. The optical identification of the *i*-RBCs may offer a new diagnostic method for the detection of the parasite's presence in the human body. This study shows that a malarial patient's infected blood samples could be distinguished with variations in spectra signatures from uninfected blood samples, as such the infected blood samples are generally flooded with fluorescence spectra decay intensities.

179

Recommendations

It is recommended that the LIF, spectrophotometry and SI techniques be applied on *P.falciparum i*-RBCs to characterize and compare PDs in males and females as well as children of different ages. These techniques could also be applied to other species of the *Plasmodium* parasite. It is also recommended that other optical techniques such as polarization microscopy and confocal microscopy be applied to the *P.falciparum* parasite detection and possibly to the other species. Employing these techniques to the *P.falciparum* parasite *i*-RBCs and the other species of the *Plasmodium* parasite would aid in drug production, successful control of species identification and management of malaria patients.

REFERENCES

Abrardo, A., Alparone, L., Cappellini, V., & Prosperi, A. (1999). Color Constancy from Multispectral Images. *Proc. IEEE Int'l Conf. Image Processing*, **3**, 570-574.

Acheampong, D. O., Appiah, M. G., Boamponsem, L. K., Boampong, J. N., & Afoakwaah, R. (2011). The efficacy of rapid diagnostic test (rdt) in diagnosing *Plasmodium Falciparum* malaria in some selected health facilities in the cape coast metropolis of Ghana. *Advances in Applied Science Research*, **2** (4), 348-356.

Adu-Gyasi, D., Adams, M., Amoako, S., Mahama, E., Nsoh, M., Amenga-Etego, S., Baiden, F., Asante, K. P., Newton, S., & Owusu-Agyei, S. (2012). Estimating malaria parasite density: assumed white blood cell count of 10000/μl of blood is appropriate measure in Central Ghana. *Malaria Journal,* **11**(1), 238.

Afromowitz, M. A., Callis, J.B., Heimbach, D. M., DeSoto, L. A., & Norton, M. K. (1979). Multispectral imaging of burn wounds: a new clinical instrument for evaluating burn depth. *IEEE Trans Biomedical Engineering*, **35**, 842- 850.

Agarwal, P. K., & Procopiuc, C. M. (1998). Exact and approximation algorithms for clustering, Discrete algorithms, Proc. Ninth Ann. *ACM-SIAM Symp.*, 658-667.

Akuwudike, A. R., Chikezie, P. C., & Chilaka, F. C. (2010). Absorption spectra of normal adult and sickle cell hemoglobin treated with hydrogen peroxide at two pH values. *Advances in Bioresearch*, **1**, No. 2, 55-60.

Albani, J. R. (2007). *Principles and Applications of Fluorescence Spectroscopy*. Blackwell Publishing, France.

Alberts, B. M., Barry, J., Bedinger, P., Formosa, T., Jongeneel, C.V., & Kreuzer, K.N. (1983). Studies on DNA replication in the T4 bacteriophage in vitro system. *Cold Spring Harbor Symp. Quant. Biol.*, **47**, 655.

Alexander, N., Schellenberg, D., Ngasala, B., Petzold, M., Drakeley, C., & Sutherland, C. (2010). Assessing agreement between malaria slide density readings. *Malaria Journal*, **9**(4), 1-12.

Allied Vision Technologies[©] (AVT). (2009).

Alonso, P., Smith, T., & Armstrong Schellenberg, J. (1994). Randomised trial of efficacy of spf66 vaccine against plasmodium falciparum malaria in children in southern tanzania. *Lancet*, **344**, 1175-1181.

Al-Salhi, M., Masilamani, V., Vijmasi, T., Al-Nachawati, H., & Vijaya Raghavan, A. P. (2011). Lung cancer detection by native fluorescence spectra of body fluids-a preliminary study. *Journal of fluorescence*, **21**(2), 637-645.

Altshuler, G. B. (2004). Absorption characteristics of tissues as a basis for the optimal wavelength choice in photodermatology. *Palomar Medical Technologies*, Inc., Burlington, 157-163.

Amexo, M., Tolhurst, R., Barnish, G., & Bates, I. (2004). Malaria misdiagnosis: effects on the poor and vulnerable. *Lancet,* **364**, 1896-1898.

Anderson, R., & Parrish, J. (1981). The optics of human skin. *Journal of Investigative Dermatology*, **77**(1), 13-19.

Anderson, B., Buah-Bassuah, P.K., & Tetteh, J.P. (2004). Using violet laser-induced chlorophyll fluorescence emission spectra for crop yield assessment of cowpea (*Vigna unguiculata (L) Walp*) varieties. *Measurement, Science & Technology*, **15**, 255-1265.

Andor technology. (2006). Absorption, Transmission and Reflectance (ATR) Spectroscopy. Retrieved from www.andor.com.

Angulo, J. (2008). A mathematical morphology approach to cell shape analysis. Centre de Morphologie Mathematique - Ecole des Mines de Paris 35, rue Saint-Honore, 77300 Fontainebleau, France.

Arora, S., Raghavan, P., & Rao, S. (1998). Approximation schemes for Euclidean k-median and related problems, Proc. 30th Ann. *ACM Symp*, *Theory of Computing*, 106-113.

Arridge, S. R., & Schweiger, M. (1997). Image reconstruction in optical tomography. *Phil. Trans. R. Soc.*, London, **B 352**, 717-726.

Ayata, C., Dunn, A. K., Gursoy-Özdemir, Y., Huang, Z. Boas, D. A., & Moskowitz, M. A. (2004). Laser speckle flowmetry for the study of cerebrovascular physiology in normal and ischemic mouse cortex. *J. Cereb. Blood Flow Metab.*, **24**, 744-755.

Bahar, S., Suh, M., Zhao, M., & Schwartz, T. H. (2006). Intrinsic optical signal imaging of neocortical seizures: the 'epileptic dip. *NeuroReport*, **17**(5), 499-503.

Baird, J. K., Masbar, S., Basri, H., Tirtokusumo, S., Subianto, B., & Hoffman, S.L. (1998). Age-dependent susceptibility to severe disease with primary exposure to *Plasmodium falciparum. J. Infect. Dis*., **178**, 592-595.

Bajorski, P. (2012). Statistics for Imaging, Optics and Photonics. John Wiley & Sons, Inc., Hoboken, New Jersey, 193-240.

Banchongaksorn, T., Prajakwong, S., Rooney, W., & Vickers, P. (1997). Operational trial of ParaSight-F (dipstick) in the diagnosis of falciparum malaria at the primary health care level. *Southeast Asian Journal of Tropical Medicine and Public Health*, **28**(2), 243-246.

Barócsi, A., Kocsányi, L., Várkonyi, S., Richter, P., Csintalan, Z., & Szente, K. (2000). Two wavelength, multipurpose, truly portable chlorophyll fluorometer and its application in field monitoring of phytoremediation. *Meas. Sci. Technol.*, **11**, 717-729.

Barun, V. V., & Ivanov, A. P. (2009). Localized light absorption by hemoglobins of an erythrocyte suspension. *Journal of Applied Spectroscopy*, **76**(4), 487-495.

Bates, I., Bekoe, V., & Asamoa-Adu, A (2004). Improving the accuracy of malaria-related laboratory tests in Ghana. *Malar J*, **3**(38), 20-28.

Bautista, P. A., & Yagi, Y. (2011). Localization of Eosinophilic Esophagitis from H&E stained images using multispectral imaging. *Diagnostic Pathology*, **6**, 1-8.

Beer, A. (1852). Determination of the absorption of red light in coloured liquids. *Ann. Phys. Chem*, **162**, 78-88.

Belisle, J. M., Costantino, S., Leimanis, L. S., Bellemare, M. J., Bohle, S. D., Geroges, E., & Wiseman, P.W. (2008). Sensitive detection of malaria infection by third harmonic generation imagiflg. *Biophys. J.*, **94**(4), L26-L28.

Belliveau, J. W., Kennedy, D. N., McKinstry, R. C., Buchbinder, B. R., Weisskoff, R. M., Cohen, M. S., Vevea, J. M., Brady, T. J., & Rosen, B. R. (1991). Functional mapping of the human visual cortex by magnetic resonance imaging. *Science*, **254**(5032), 716-719.

Bengtsson, M., Wallström, S., Sjöholm, S., Grönlund, R., Anderson, B., Larsson A., Karlsson, S., Kroll, S., & Svanberg, S. (2005). Fungus covered insulator materials studied with laser-induced fluorescence and principal component analysis. *Appl. Spec.*, **59**, 1037-1041.

Benveniste, H., & Blackband, S. (2002). MR microscopy and high resolution small animal MRI: Applications in neuroscience research. *Prog Neurobiol.*, **67**(5), 393-420.

Bersha, K. S. (2010). *Spectral Imaging and Analysis of Human Skin*. Master Thesis Report, Master Erasmus Mundus in Colour in Informatics and Media Technology (CIMET), University of Eastern Finland.

Berwick, J., Devonshire, I. M., Martindale, A. J., Johnston, D., Zheng, Y., Kennerley, A. J., Overton, P. G., & Mayhew, J. E. (2005). Cocaine administration produces a protracted decoupling of neural and haemodynamic responses to intense sensory stimuli. *Neuroscience (Oxford)*, **132**(2), 361-374.

Beuthan, J., Minet, O., Helfmann, J., Herrig, M., & Muller, G. (1996). The spatial variation of the refractive index in biological cells. *Phys. Med. Biol*. **41**, 369-382.

185

Bilal, M., Saleem, M., Amanat, S. T., Shakoor, H. A., Rashid, R., Mahmood, A., & Ahmed, M. (2015). Optical diagnosis of malaria infection in human plasma using Raman spectroscopy. *J. Biomed. Opt*., **20**(1), 0170021-0170028.

Biritwum, R. B., Gulaid, J., & Amaning, A. O. (2000). Pattern of diseases or conditions leading to hospitalisation at the Korle Bu Teaching hospital. *Ghana Med. J*., **34**, 197-205.

Bleakley, H. (2003). Disease and Development: Evidence from the American South. *Journal of the European Economic Association*, **1.2-3**, 376-386.

Bloland, P. B., Ettling, M., & Meek, S. (2000). Combination therapy for malaria in Africa:hype or hope? *Bulletin of the World Health Organization,* **78**, 1378-1388.

Bloland, P. B. (2001). *Drug resistance in malaria*. Geneva: World Health Organization.

Bloland, P. B. (2001). *Drug resistance in malaria*, *WHO/CDS/CSR/DRSI* 2001.4 World Health Organization, Switzerland.

Bloland, P. B., Kachur, S. P., & Williams, H. A. (2003). Trends in antimalarial drug deployment in sub-Saharan Africa. *J. Exp Biol.,* **206** (Pt 21), 3761-3769.

Bohren, C., & Huffman, D. (1983). *Absorption and scattering of light by small particles*. Wiley, New York.

Bolay, H., Reuter, U., Dunn, A., Boas, D., & Moskowitz, M. (2002). Intrinsic brain activity triggers trigeminal meningeal afferents in a migraine model. *Nat. Med.*, **8**, 136-142.

Boulnois, J. C. (1986). Photophysical processes in recent medical laser developments: a review. *Lasers in medical science*, **1**, 47-48.

Bouguer, P. (1729). *Essai d'optique sur la gradation de la lumière*. Claude Jombert, Paris, France.

Bremard, C., Girerd, J. J., Kowalewski, P., Merlin, J.C., & Moreau, S. (1993). Spectroscopic investigations of malaria pigment. *Appl. Spectrosc.* **47**, 1837-1842.

Brigham, E. O. (1988). *The fast Fourier transform and its applications*. Englewood Cliffs, N.J., Prentice Hall.

Bruce-Chwatt, L. J. (1984). Lessons learned from applied field research activities in Africa during the malaria eradication era. *Bull World Health Organ*, **62**, 19-29.

Brydegaard, M., Guan, Z., & Svanberg, S. (2009). Broad-band multispectral microscope for imaging transmission spectroscopy employing an array of light-emitting diodes. *American Association of Physics Teachers*,**77**, 104-110.

Brydegaard, M., Merdasa, A., Jayaweera, H., Ålebring, J., & Svanberg, S. (2011). Versatile multispectral microscope based on light emitting diodes. *Review of Scientific Instruments*, **82**, 1106-1113.

Brydegaard, M., Haj-Hosseini, N., Wårdell, K., & Andersson-Engels, S. (2011). Photobleaching-Insensitive Fluorescence Diagnostics in Skin. *IEEE Photonics Journal*, **3**, 407-412.

Buxton, R. B. (2002). *Introduction to Functional Magnetic Resonance Imaging: Principles & Techniques*. Cambridge: Cambridge University Press.

187

Calleri, G., Lipani, F., Macor, A., Belloro, S., Riva, G., & Caramello, P.
(1998). Severe and complicated falciparum malaria in Italian travelers.
J. Travel Med., **5**, 39-41.

Campbell, M. C., Cookson, C. J., Bueno, J. M., Seaman, A., & Kisilak, M. L.
(2007). *Confocal polarimetry measurements of tissue infected with
malaria, in Cont. Frontiers in Optics. Seeing the Invisible: Strategies
for Imaging Transparent Cell Types II (FThK)*. OSA, San Jose,
California.

Cambridge Research & Instrumentation, Inc. (CRi). (2010). Retrieved from
www.cri-inc.com

Cannestra, A. F., Pouratian, N., Bookheimer, S. Y., Martin, N. A., Beckerand,
D. P., & Toga, A. W. (2001). Temporal spatial differences observed by
functional MRI and human intraoperative optical imaging. *Cereb.
Cortex*, **11**(8), 773-782.

Carcagni, P., Patria, A. D., Fontana, R., Greco, M., Mastroianni, M.,
Materazzi, M., Pampaloni, E., & Pezzati, L. (2007). Multispectral
imaging of paintings by optical scanning. *Optics and Lasers in
Engineering*, **45**, 360-367.

Cardei, V. C., Funt, B., & Kobus, B. (1999). White point estimation for
uncalibrated images. *Imaging Science and Technology Society*.
Appl.Opt., **44**, 5696-5703.

Carter, W. D. (1996). *Raman spectroscopic study of single red blood cells
infected by the malaria parasite Plasmodium falciparum*. Master
Thesis, Department of Physics, College of Sciences, University of
Central Florida Orlando, Florida, USA.

Center for Disease Control and Prevention (CDC). (2010). Retrieved from

http://phil.cdc.gov/phil/home.asp

Chandramohan, D., Carneiro, I., Kavishwar, A., Brugha, R., Desai, V., &

Greenwood, B. (2001). A clinical algorithm for the diagnosis of

malaria: results of an evaluation in an area of low endemicity. *Tropical

Medicine and International Health*, **6**, 505-510.

Chandramohanadas, R., Park, Y., Lui, L., Li, A., Quinn, D., Liew, K., Diez-

Silva, M., Sung, Y., Dao, M., Lim, C. T., Preiser, P. R., & Suresh, S.

(2011). Biophysics of Malaria Parasite Exit from Infected

Erythrocytes. *PLoS ONE*, **6**, No. 6, 20869-20878.

Chavchich, M., Gerena, L., Peters, J., Chen, N., Cheng, Q., & Kyle, D. E.

(2010). Role of pfmdr1 amplification and expression in induction of

resistance to artemisinin derivatives in Plasmodium falciparum.

Antimicrob Agents Chemother, **54**(6), 2455-2464.

Chen, Y.C., Galpern, W. R., Brownell, A. L., Matthews, R. T., Bogdanov, M.,

Isacson, O., Keltner, J. R., Beal, M. F., Rosen, B. R., & Jenkins, B. G.

(1997). Detection of dopaminergic neurotransmitter activity using

pharmacologic MRI: Correlation with PET, microdialysis, and

behavioral data. *Magn Reson Med.*, **38**(3), 389-398.

Chieu, D., Tran, Y. C., & Sergey, S. (1998). Simultaneous Multispectral

Imaging in the Visible and Near-Infrared Region: Applications in

Document Authentication and Determination of Chemical

Inhomogeneity of Copolymers. *Anal. Chem.*, **70**, 4701-4708.

Cho, S., Kim, S., Kim, Y., & Park, Y. K. (2011). Optical imaging techniques

for thestudy of malaria. *Trends Biotechnol.*, **30**(2), 71-79.

189

Clark, R. N. (1999). *Spectroscopy of rocks and minerals, and principles of spectroscopy*. Remote Sensing for the Earth Sciences. American Societyfor Photogrammetry and Remote Sensing, John Wiley and Sons Inc. New York, New York, USA.

Clark, I. A., & Hunt, N. H. (1983). Evidence for reactive oxygen intermediates causing hemolysis and parasite death in malaria. *Infection and Immunity*, **39**, 1-6.

Coffey, V. C. (2012). Multispectral imaging moves into the mainstream. *Optics and Photonics News*, **23**, 18-24.

Colarusso, P., Kidder, K. L., Levin, I. W., Fraser, J. C., Arens, J. F., & Lewis, E. N. (1998). Infrared spectroscopic imaging: from planetary to cellular system. *Applied Spectroscopy*, **52**,106-120.

Cole, R. W., & Turner, J. N. (2008). LEDs as illumination and detection sources in microscopy. *Microanalysis*, **14**, 243-250.

Colthup, N. (2012). *Introduction to infrared and Raman spectroscopy*. New York: Elsevier Science.

Cojoc, D., Finaurini, S., Livshits, P., Gur, E., Shapira, A, Mico, V., & Zalevsky, Z. (2012). Toward fast malaria detection by secondary speckle sensing microscopy. *Biomedical Optics Express*, **3**, No.5, 991-1005.

Contag, C. H., Contag, P. R., Mullins, J. I., Spilman, S. D., Stevenson, D. K., & Benaron, D. A. (1995). Photonic detection of bacterial pathogens in living hosts. *Mol. Microbiol*.; **18**,593-603.

Cope, M., & Delpy, D. T. (1988). System for long-term measurement of cerebral blood and tissue oxygenation on newbom infants by near infrared transillumination. *Med. Bid. fig. Compur.*, **26**, 289-294.

Cope, M., van der Zee, P., Essenpreis, M., Anidge, S. R., & Delpy, D. T. (1991). Data analysis method for near infrared spectroscopy of tissue: problems in determining the relative cytochrome aa3 concentration. Proc. Time-Resolved Spectroscopy and Imging of Tumes, *Proc. SPIE-lnt. Soc., Opt. Eng.*, **1431**, 251-262.

Cope, M. (1991).*The application of near infrared spectroscopy to non invasive monitoring of cerebral oxygenation in the newborn infant*. Ph.D. thesis, University College, London.

Cosentino, A. (2013). A practical guide to panoramic multispectral imaging. *e-Conservation Magazine*, **25**, 64-73.

De Goes Rocha, F. G., Barbosa Chaves, K. C., Gomes, C. Z., Campanharo, C. B., Courrol, L. C., Schor, N., & Bellini, M. H. (2010). Erythrocyte Protoporphyrin Fluorescence as a Biomarker for Monitoring Antiangiogenic Cancer Therapy. *Journal of fluorescence*, **20**(6), 1225-1231.

Demirka, O., Asyali, M. H., & Sahoo, P. K. (2009). *Image Processing with MATLAB, Applications in Medicine and Biology*. CRC Press, Taylor & Francis Group, New York.

Demtroder, W. (2003). *Laser spectroscopy-Basic concepts and instrumentation*, 3rd ed., Springer-Verlag, Berlin.

Demtroder, W. (2008). *Laser spectroscopy*. Vol. 1: Basic Principles, Springer-Verlag, Berlin, Heldelberg, GmbH.

191

Demtroder, W. (2013). *Laser spectroscopy*: *Spectroscopy with Lasers*. Springer-Verlag, Berlin.

Denninghoff, K. R., Chipman, R. A., & Hillman, L. W. (2007). Blood oxyhemoglobin saturation measurements by blue-green spectral shift. *Journal of Biomedical Optics*, **12**, 4020-4030.

De Oliveira Silva, F. R., Bellini, M. H., Tristao, V. R., Schor, N., Vieira, N. D. Jr., & Courrol, L. C. (2010). Intrinsic fluorescence of protoporphyrin IX from blood samples can yield information on the growth of prostate tumours. *Journal of fluorescence*, **20**(6), 1159-1165.

Devor, A., Dunn, A. K., Andermann, M. L., Ulbert, I., Boas, D. A., & Dale, A. M. (2003). Coupling of total hemoglobin concentration, oxygenation, and neural activity in rat somatosensory cortex. *Neuron*, **39**(2), 353-359.

Diaz, G., Gonzalez, F., & Romero, E. (2007). Infected Cell Identification in thin Blood Images Based on Color Pixel Classification: Comparison and Analysis Color Pixel Classification: Comparison and Analysis. *Springer*, Berlin, 812-821.

Dicko, A., Sagara, I., & Sissoko, M. S. (2008) Impact of intermittent preventive treatment with sulphadoxine-pyrimethamine targeting the transmission season on the incidence of clinical malaria in children in Mali. *Malaria Journal*, **7**, 123.

Dickinson, E., & Davidson, W. (2010). Introduction to Spectral Imaging. Retrieved from: http://zeiss-campus.magnet.fsu.edu/print/spectralimaging/introduction-print.html.

Di Ruberto, C., Dempster, A., Khan, S., & Jarra, B. (2001). Morphological image processing for evaluating malaria disease. *Springer-Verlag*, **4**, 739-748.

Di Ruberto, C., Dempster, A., Khan, S., & Jarra, B. (2002). Analysis infected cell images using morphological operators. *Image and Vision Computing*, **20**, 133-146.

Dondorp, A. M., Pongponratn, E., & White, N. (2004). Reduced microcirculatory flow in severe falciparum malaria: pathophysiology and electron-microscopic pathology. *Acta Trop*, **89**, 309-317.

Dowling, M. A. C., & Shute, G. T. (1966). A comparative study of thick and thin blood films in the diagnosis of scanty malaria parasitaemia. *Bull World Health Organ.*, **34**, 249-67.

Dubey, M., Weingken, C., Ganguly, N., & Mahajan, R. (1999). Comparative evaluation of methods of malaria parasite density determination in blood samples from patients and experimental animals. *Indian J Med Res*, **109**, 20-27.

Duri, S., Majoni, S. Hossenlopp, J. M., & Tran, C. D. (2010). Determination of hemical homogeneity of fire retardant polymeric nanocomposite materials by near-infrared multispectral imaging microscopy. *Analytical Letters*, **43**, 1780-1789.

Eastman, R. T., Dharia, N. V., Winzeler, E. A., & Fidock, D. A. (2011). Piperaquine resistance is associated with a copy number variation on chromosome 5 in drug-pressured Plasmodium falciparum parasites. *Antimicrob Agents Chemother,* **55**(8), 3908-3916.

Edmund Optics©. (2000).

193

Faber, D. J., Aalders, M. C. G., Mik, E. G., Hooper, B. A., van Gemert, M .J. C., & van Leeuwen, T.G. (2004). Oxygen saturation-dependent absorption and scattering of blood. *The American Physical Society, Physical Review Letters*, **93**(2), 0281021-0281024.

Fantini, S. (2004). *Near-infrared spectroscopy for the study of biological tissue*. Department of Biomedical Engineering, Tufts University.

Fauaz, G., Miranda, A. R., Gomes, C. Z., Courrol, L. C., de Oliveira Silva, F. R., de Goes Rocha, F. C., & Bellini, M. H. (2010). Erythrocyte Protoporphyrin Fluorescence as a Potential Marker of Diabetes. *Applied Spectroscopy,* **64**(4), 391-395.

Fedosov, D. A., Caswell, B., Suresh, S., & Karniadakis, G. E. (2010). *Quantifying the biophysical characteristics of Plasmodium-falciparum-parasitized red blood cells in microcirculation*. Princeton University, Princeton, NJ.

Fernando, S. D., Karunaweera, N. D., & Fernando, W. P., (2004). Evaluation of a rapid whole blood immunochromatographic assay for the diagnosis of *Plasmodium falciparum* and *Plasmodium vivax* malaria. *Ceylon Med J,* 49: 7- 11.

Fischer, A. A., Laing, J. E., Stoeckel, J. E., & Townsend, J. W. (1998). Handbook for family planning operations research design. *Population council, New York*.

Frean, J. (2010). Microscopic determination of malaria parasite load: role of image analysis. *Microscopy: Science, Technology. Applications and Education*, **3**, 862-866.

Frey, F. S., & Warda, J. (2008). *American Institute for Conservation of Historic and Artistic Works, Digital Photographic Documentation Task Force: The AIC guide to digital photography and conservation documentation*. Washington, D.C.

Friebel, M., Roggan, A., Muller, G., & Meinke, M. (2006). Determination of optical properties of human blood in the spectral range 250 to 1100 nm using Monte Carlo simulations with hematrocrit-dependent effective scattering phase functions. *J. Biomed. Opt.,* **11**(3), 34021-34031.

Forney, J. R., Magill, A. J., Wongsrichanalai, C., Sirichaisinthop, J., Bautista, C. T., Heppner, D. G., Miller, R. S., Ockenhouse, C. F., Gubanov, A, Shafer, R., DeWitt, C. C., Quino-Ascurra, H. A, Kester, K. E., Kain, K. C., Walsh, D. S., Ballou, W. R., & Gasser, R. A Jr, (2001). Malaria rapid diagnostic devices: performance characteristics of the ParaSight F device determined in a multisite field study. *J Clin Microbiol,* **39**, 2884-2890.

Gallup, J. L. & Sachs, J. D. (2001). The economic burden of malaria. *American Journal of Tropical Medical Hygiene*, **64**, 1-11.

Gao, S., Lan, X., Liu, Y., Shen, Z., Lu, J., & Ni, X. (2004). Characteristics of blood fluorescence spectra using low-level, 457.9 nm excitation from Ar^+ laser. *Chinese Optics Letters*, **2**(3), 160-161.

Garcia, A, Dieng, A, Rouget, F., Migot-Nabias, F., & Le Hesran, J. (2004). Role of environment and behaviour in familial resemblances of plasmodium falciparum infection in a population of senegalese children. *Microbes and Infections,* **6**, 68-75.

Gat, N. (1999). Hyperspectral Imaging. *Spectroscopy*, **14**, No.3, 28-32.

Gat, N. (2000). Imaging spectroscopy using tunable filters: A Review. *The International Society of Optical Engineering (SPIE)*, **4056**, 50-64.

Ginsburg, H., & Atamna, H. (1994). Origin of reactive oxygen species in erythrocytes infected with Plasmodium falciparum. *Molecular Biochemistry, Parasitol*, **1**, 5-13.

Goldberg, D. E., Slater, A. F. G., Cerami, A., & Henderson, G. B. (1990). Hemoglobin degradation in the malaria parasite *Plasmodium falciparum*: An ordered process in a unique organelle. *Biochem.,* **87**, 2931-2935.

Gollin, D., & Zimmermann, C. (2007). Malaria: Disease Impacts and Long-Run Income Differences. *IZA*, **2997**, 1-25.

Gonzalez, R. C., Woods, R. E., & Eddins, S. L. (2004). *Digital Image Processing Using MATLAB.* Prentice Hall.

Graves, E. E., Ripoll, J., Weissleder, R., & Ntziachristos, V. (2003). A submillimeter resolution fluorescence molecular imaging system for small animal imaging. *Med Phys*., **30**, 901-911.

Greenberg, A. E., & Lobel, H.O. (1990). Mortality from *Plasmodium falciparum* malaria in travelers from the United States, 1959 to 1987. *Ann. Intern. Med*., **113**, 326-327.

Günter, W., & Stiles, W. S. (1982). *Colour Science: Concepts and methods, Quantitative Data Formulae*. John Wiley and Sons, 2nd Edition.

Guerin, P. J., Olliaro, P., Nosten, F., Druilhe, P., Laxminarayan, R., Binka, F., Kilama, W. L., Ford, N., & White, N. J. (2002). Malaria: current status of control, diagnosis, treatment and a proposed agenda for research and development. *Lancet: Infect. Dis.,* **2**(9), 564-573.

Gustafsson, U., Somesfalean, G., Alnis, J., & Svanberg, S. (2000) Frequency-
modulation spectroscopy with blue diode lasers. *Appl. Opt*., **39**, 3774-
3780.

Hammami, I., Nuel, G., & Garcia, A. (2013). Statistical Properties of Parasite
Density Estimators in Malaria. *PLoS ONE,* **8**(3), e51987.

Hammer, M., Schweitzer, D., Michel, B., Thamm E., & Kolb, A. (1998).
Single scattering by red blood cells*. Applied Optics*, **37**, No. 31.

Hanbury, A., & Serra, J. (2001). *Mathematical Morphology in the
L*a*b*Colour Space*. Technical report N-36/01/M, Centre of
Mathematical Morphology, France.

Hänscheid, T., Valadas, E., & Grobusch, M. P. (2000). Automated malaria
diagnostics using pigment detection. *Parasitol. Today,* 16(12), 549-

Harwood, L. M., Moody, C. J., & Harwood, L. M. (1989). *Experimental
organic chemistry: principles and practice*. Oxford, United Kingdom:
Blackwell Scientific., 551.

Hauta-Kasari, M. Miyazawa, K. Toyooka, S., & Parkkinen, J. (1999). A
Prototype of the Spectral Vision System. *Proc. 11th Scandinavian
Conf. Image Analysis*, **1**, 79-86.

Hay, S. I., Guerra, C. A., Tatem, A., Noor, A. M., & Snow, R. W. (2004). The
global distribution and population at risk of malaria: past, present and
future. *Lancet. Infect Dis*, **4**, 327-336.

Hempelmann, E. (2007). Hemozoin Biocrystallization in Plasmodium
falciparum and the antimalarial activity of crystallization inhibitors.
Parasitol Res., **100**, 671-676.

Herman, P., Maliwal, B. P., Lin, H. J., & Lakowicz, R. (2001). Exciting bright
field fluorescence with power LEDs. J*ournal of Microscopy*, **203**,176-
183.

Hillman, E. M. C. (2007). Optical brain imaging *in vivo*: techniques and
applications from animal to man. *J. Biomed. Opt*., 12(5), 154021-
1540228.

Hillman, E. M. C., Devor, A., Bouchard, M., Dunn, A. K., Krauss, G. W.,
Skoch, J., Bacskai, B. J., Dale, A. M., & Boas, D. A. (2007).
Depthresolved optical imaging and microscopy of vascular
compartment dynamics during somatosensory stimulation.
Neuroimage, **35**(1), 89-104.

Ho, M., & White, N. J. (1999). Molecular mechanisms of cytoadherence in
malaria. *American Journal of Physiology*, **276**, 1231-1242.

Ho, M., Hickey, M. J., Andonegui, A. G., & Kubes, P. (2000). Visualization
of Plasmodium falciparum-endothelium interactions in human
microvasculature: mimicry of leukocyte recruitment. *J. Exp. Med.*,
192,1205-1211.

Horecker, B. L. (1942). The absorption spectra of hemoglobin and its
derivatives in the visible and near infra-regions. *J. Biol. Chem*., **148**,
178-183.

Hu, Y., Wu, Q., Liu, S., Wei, L., Chen, X., Yan, Z., Yu, J., Zeng, L., & Ding,
Y. (2005). Study of Rice Pollen Grains by Multispectral Imaging
Microscopy, Microscopy Research and Technique, *Wiley-Liss, Inc*.,
68, 335-346.

Hunt, N. H., & Stocker, R., (1990). Oxidative stress and the redox status. *Blood Cells*, **16**, 499-526.

Inaba, M., Katoh, N., & Imai, H. (1994). Applications of weighted Voronoi diagrams and randomization to variance-based k-clustering. Proc. 10th Ann. ACM Symp. *Computational Geometry*, 332-339.

Ishimaru, A. (1978). Wave Propagation and Scattering in Random Media and Rough Surfaces. *Proceedings of the IEEE*, Vol. **79**, No. 10, 1045-1050.

Jablonski, A. (1935). *Zeitschrift fur Physik*, **94**, 38-64.

Jacques, S. L. (1998). Skin Optics Summary. Oregon Medical Laser Center News. Retrieved from http://omlc.ogi.edu/news/jan98/skinoptics.html.

Jacques, S., & Pogue, B. (2008). Tutorial on diffuse light transport. *Journal of Biomedical Optics*, **13**, 302-310.

Jain, A. K., & Dubes, R. C. (1988). *Algorithms for Clustering Data*. New Jersey,Prentice Hall.

Jain, A. K., Murthy, M. N., & Flynn, P. J. (1999). Data clustering: a review. *ACM Computing Reviews*, **31**(3), 264-323.

Jalil, B. (2008). Multispectral Image Processing Applied to Dermatology. MSc thesis, Le2i laboratory, Université de Bourgogne.

Jamieson, J. D., & Palade, G. E. Intracellular transport of secretory proteins in the pancreatic exocrine cell. I. Role of the peripheral elements of the Golgi complex. *J. Cell Biol.*, **34**(2), 577-596.

Jamjoom, G. A. (1983). Dark-field microscopy for detection of malaria in unstained blood films. *J. Clin. Microbiol.,* **17**(5), 717-721.

Josephine F. P., & Nissapatorn, V. (2005). Malaria: the value of the automated depolarization analysis. *Southeast Asian J. Trop. Med. Public Health*, **36**(Suppl 4), 68-72.

Kalnina, I., Kurjane, N., Kirilova, E., Klimkane, L., Kirilov, G., & Zvagule, T. (2010). Correlation of altered blood albumin characteristics and lymphocyte populations to tumor stage in gastrointestinal cancer patients. *Cancer biomarkers*, **7**(2), 91-99.

Kane, K. E., & Lee, W. S. (2007). Multispectral imaging for in-field green citrus identification. *In ASAE Annual International Meeting*, Minneapolis, MN, Paper 073025.

Kanungo T., Mount, D. M., Netanyahu, N. S., Piatko, C. D., Silverman, R., & Wu A. Y. (2002). An Efficient K-means clustering algorithm: Analysis and implementation. *IEEE transactions on pattern analysis and machine intelligence*, **24**, No. 7, 881-892.

Karadaglic, D., Wood, A. D., McRobbie, M., Stojanovic, R., & Herrington, C. S. (2009). Fluorescence spectroscopy of an in vitro model of human cervical neoplasia identifies graded spectral shape changes with neoplastic phenotype and a differential effect of acetic acid. *Cancer epidemiology*, **33(**6), 463-468.

Katsir, A. (1993). *Lasers and optical fibres in medicine*. Academic Press, New York.

Kawamoto, F. (1991). Rapid diagnosis of malaria by fluorescene microscopy with light microscope and interference filter. *Lancet,* **337**(8735), 200-202.

Kelley, S. S., Rials, T. G., Snell, R., Groom, L. R., & Sluiter, A. (2004). Use of near infrared spectroscopy to measure the chemical and mechanical properties of solid wood. *Wood Sci. Technology*, **38**, 257-276.

Khait, O., Smirnov, S., & Tran, C.D. (2001). Multispectral imaging Microscope with millisecond time resolution. *Analytical Chemistry*, **73** (4), 732-739.

Kilejian, A. (1979). Characterization of a protein correlated with the production of knob- like protrusions on membranes of erythrocytes infected with Plasmodium falciparum. *Proc. Natl. Acad. Sci.*, USA, **76**, 4650-4653.

Knee, J. L. (1996). Spectra of Atoms and Molecules by Peter F. Bernath. *Am. J. Phy.*, **64**, 93-93.

Kolliopoulos, S., Rao, S., & Nesetril, J. (1999). A nearly linear-time approximation scheme for the Euclidean k-median problem. Proc. Seventh Ann. *European Symp. Algorithms*, **52**, 362-371.

Kremsner, P., Zotter, G., Feldmeier, H., Graninger, W., & Rocha, R. (1988). A comparative trial of three regimens for treating uncomplicated *falciparum* malaria in Acre, Brazil. *J. Infect Dis,* **158**, 1368-1371.

Krzanowski, W.J. (1977). The performance of Fisher's linear discriminant function under non-optimal conditions. *Technometrics*, **19**, 191-200.

Kwong, K. K., Belliveau, J. W., Chesler, D. A., Goldberg, I. E., Weisskoff, R. M., Poncelet, B. P., Kennedy, D. N., Hoppel, B. E., Cohen, M. S., Turner, R., Cheng, H-M, Brady, T. J., & Rosen, B. R. (1992). Dynamic magnetic resonance imaging of human brain activity during primary sensory stimulation. *Proc. Natl. Acad. Sci. U.S.A.*, **89**(12), 5675-5679.

Kyowa Optical. (2007). Retrieved from

  http://www.kyowaopt.co.jp/English/malaria/malaria.htm

Lakowicz, J. R. (1999) *Principles of Fluorescence Spectroscopy*, 2nd ed.

  Kluwer, Academic /Plenum publishers, New York.

Lakowicz, J. R. (2006). *Principles of Fluorescence Spectroscopy*. New York:

  Springer Science & Business Media.

Lambert, J. H. (1760). *Photometry, or, On the measure and gradations of*

  light, colors, and shade. Augsburg , Germany: Eberhardt Klett.

Lawrence C., & Olson, J. A. (1986). Birefringent hemozoin identifies malaria.

  Am. J. Clin. Pathol., **86**(3), 360-363.

Le Port, A, Cottrell, G., Dechavanne, C., Bouraima, A., & Briand, V. (2011).

  Prevention of malaria during pregnancy: assessing the effect of the

  distribution of iptp through the national policy in benin. *Am. J. Trap.*

  Med., **82***,* 270-275.

Lee, W. G., Kim, Y. G., Chung, B. G., Demirci, U., & Khademhosseini, A.

  (2010). Nano/microfluids for diagnostic of infectious diseases in

  developing countries. *Adv. Drug Deliv. Rev.,* **62**(4-5), 449-457.

León, K., Mery, D., & Pedreschi, F. (2005). Colour Measurement in L*a*b*

  units. *Journal of Food Engineering*, **36**, 150-162.

Levenson, R. M., & Hoyt, C. C. (2000). Spectral imaging and microscopy. *Am*

  Lab, **32**, 26-33.

Lewis, I. R., & Edwards, H. (2001). *Handbook of Raman spectroscopy: from*

  the research laboratory to the process line. New York: Marcel

  Dekker.

Lewis-Beck, M., Bryman, A., & Futing, T. (2003). Multivariate Analysis. *Social Sciences Research Methods*, Thousand Oaks (CA), **86**, 220-235.

Liu, G. Y., & Peng, Y. X. (2000). Biological Physics (in Chinese). Wuhan University Press, Wuhan.

Lopez-Alvarez, M. A., Hernandez-Andres, J., Valero, E. M., & Romero, J. (2007). Selecting algorithms, sensors, and linear bases for optimum spectral recovery of skylight. *J. Opt. Soc. Am.*, **24**, 942-956.

Lothian, G. F., & Levis P. C. (1956). Absorption spectrophotoinetry. *Nature*, **178**, 1342-1351.

Loyevsky, M., LaVaute, T., Allerson, C. R., Stearman, R., Kassim, O. O., Cooperman, S., Gordeuk, V. R., & Rouault, T. A. (2001). An IRP-like protein from *Plasmodium falciparum* binds to a mammalian iron-responsive element. *BLOOD*, **98**(8), 2555-2562.

Lüersen, K., Walter, R. D., & Müller, S. (2000). Plasmodium falciparum infected red blood cells depend on a functional glutathione de novo synthesis attributable to an enhanced loss of glutathione. *Biochemical Journal*, **346**, 545-552.

Luker, G. D. & Luker, K. E., (2008). Optical Imaging: Current Applications and Future Directions. *J. Nucl. Med.*, **49**, 1-4.

Ma, C., Harrison, P., Wang, Ross, L., & Coppel, L. (2010). Automated estimation of parasitaemia of Plasmodium yoelii-infected mice by digital image analysis of Giemsa-stained thin blood smears. *Malaria Journal*, **9**, 348-352.

MacRae, R. A., McClure, J. A., & Latimert, P. (1961). Spectral transmission and scattering properties of red blood cells. *Journal of the Optical Society of America*, **51**, No. 12, 1366-1372.

Makkapati, V. V., & Naik, S. K. (2009). Clump Splitting based on Detection of Dominant Points from Contours. *5th Annual IEEE Conference on Automation Science and Engineering Bangalore*, India, 220-233.

Makler, M. T., Palmer, C. J., & Ager, A. L. (1998). A review of practical techniques for thediagnosis of malaria. Annals of Tropical Medicine & Parasitology, **92**, No. 4, 419-433.

Marieb, E. (1995). *Human Anatomy and Physiology*, (3rd Ed.). The Benjamin/Cummings Publishing Company, Inc., Redwood City, CA.

Martinez, W. L., & Martinez, A. R. (2005). *Exploratory Data Analysis with MATLAB$^{®}$*. Computer Science and Data Analysis Series, Chapman & Hall/CRC.

Masilamani, V., Trinka, V., Al Salhi, M., Elangovan, M., Raghavan, V., Al Diab, A. R., & Al-Nachawati, H. (2011). A new lung cancer biomarker-a preliminary report. *Photomedicine and laser surgery*, **29**(3), 161-170.

Masilamani, V., Devanesan, S., Ravikumar, M., Perinbam, K., AlSalhi, M. S, Prasad, S., Palled, S., Ganesh, K. M., & Alsaeed, A. H. (2014). Fluorescence spectral diagnosis of malaria-a preliminary study. *Diagnostic Pathology*, **19**(182), 1-7.

Mathworks Inc. (2014). R2012a Matlab 8.3.0.532.

Matousek, J. (2000). On Approximate Geometric k-clustering. *Discrete and Computational Geometry*, **24**, 61-84.

Matthias, F. (2006). Spectral image processing in real-time. *J. Real-Time Image Proc*, **1**, 25-32.

Matthews, P. M., Honey, G. D., & Bullmore, E. T. (2006). Applications of fMRI in translational medicine and clinical practice. *Nat. Rev. Neurosci.*, **7**(9), 732-744.

Mauritz, J. M. A., Tiffert, T., Seear, R., Lautenschläger, F., Esposito, A., Lew, V. L., Guck, J., & Kaminski, C. F. (2010). Detection of Plasmodium falciparum-infected red blood cells by optical stretching. *Journal of Biomedical Optics (JBO)*, **15**, No. 3, 0305171-0305173.

McCreery, R. L. (2005). *Raman spectroscopy for chemical analysis* (Vol. 225). Toronto, Canada: John Wiley & Sons.

Mejac, I., Bryan, W. W., Lee, T. R., & Tran, C. D. (2009). Visualizing the size, shape, morphology, and localized surface plasmon resonance of individual gold nanoshells by near-infrared multispectral imaging microscope. *Anal. Chem.*, **81**, 6687-6694.

Mendelow, B. V., Lyons, C., Nhlangothi, P., Tana, M., Munster, M., Wypkema, E., Liebowitz, L., Marshall, L., Scott, S., & Coetzer, T. L. (1999). Automated malaria detection by depolarization of laser light. *Br. J. Haematol.*, **104**(3), 499-503.

Mens, P.F., Matelon, R. J., Nour, B. Y. M., Newman, D. M., & Schallig, H. D. F. H. (2010). Laboratory evaluation on the sensitivity and specificity of a novel and rapid detection method for malaria diagnosis based on magneto-optical technology (MOT). *Malaria J.,* **9**,207.

Merdasa, A. (2010), *Multispectral Microscopy with application to Malaria Detection*. Master thesis, Division of Atomic Physics, Lund University.

205

Merdasa, A., Brydegaard, M., Svanberg, S., & Zoueu, J. T. (2013). Staining-free malaria diagnostics by multispectral and multimodality light-emitting-diode microscopy. *J.Biomed Opt*., **18**(3), 0360021-03600210.

Michaelis, J., Hettich, C., Mlynek, J., & Sandoghdar, V. (2000). Optical microscopy using a single-molecule light source. *Nature*, **405**(6784), 325-328.

Mie, G. (1908). Contributions to the optics of diffuse media, especially colloid metal solutions. *Ann Phys*., **25**, 377-445.

Mika, A.M. (1990). Linear-Wedge Spectrometer. *Proc. SPIE Imaging Spectroscopy of the Terrestrial Environment*, **1298**, 127-131.

Mittal, G., Locharam, S., Sasi, S., Shaffer, G. R., & Kumar, A.K. (2006). An efficient video enhancement method using L*a*b* analysis. *IEEE Computer Society*, **79**, 66-70.

Molla, S., de La Rubia, J., Arriaga, F., Fernandez, M. J., Caprio, N., & Marty, M. L. (2001). Role of exchange transfusion in patients with severe *P. falciparum* malaria: report of six cases. *Haematologica*, **86**, 208-209.

Monnet, G. (1995). 3D Spectroscopy with Large Telescopes: Past, Present and Prospects. *Tridimensional Optical Spectroscopic Methods in Astronomy*, **71**, 12-17.

Montet, X., Ntziachristos, V., Grimm, J., & Weissleder, R. (2005). Tomographic fluorescence mapping of tumor targets. *Cancer Res.,* **65**, 6330-6336.

Moody, A. H., & Chiodini, P. L. (2000). Methods for the detection of blood parasites. *Clin. Lab. Haem*., **22**,189-202.

206

Moody, A. (2002). Rapid diagmostic test for Malaria parasites. *Clin. Microbial. Rev.,* **15**(1), 66-78.

Moore, L. R., Fujioka, H., Williams, P. S., Chalmers, J. J., Grimberg, B., Zimmerman, P. A., & Zborowski, M. (2006). Hemoglobin degradation in malaria-infected erythrocytes determined from live cell magnetophoresis. *The FASEB Journal*, **20**, No. 6, 747-749.

Morris, M. D. (1993). *Microscopic and spectroscopic imaging of the chemical State*. New York, Marcel Dekker.

Mourant, J. R., Tamara, M. J., Gerrit, L., & Irving, J. B. (1998). Non-invasive measurement of chemotherapy drug concentrations in tissue: preliminary demonstrations of in vivo measurements. *Phys. Med. Biol*., **44**, 1397-1417.

Mourant, J. R., Johnson, T. M., Carpenter, S., Guerra, A., Aida, T., & Freyer, J. P. (2002). Polarized angular dependent spectroscopy of epithelial cells and epithelial cell nuclei to determine the size scale of scattering structures. *J. Biomed. Opt.*, **7**, 378-387.

Murray, R. K. (2003). Porphyrins & Bile Pigments. In: *Harper's Illustrated Biochemistry,* 26th Ed., Lange Medical Books/McGraw-Hill, New York.

Murray, C. K. (2008). Update on rapid diagnostic testing for malaria. *Clin. Microbial. Rev.,* **21**(1), 97-110.

Mwangi, T. W., Bethony, J., & Brooker, S. (2006). Malaria and helminth interactions in humans: an epidemiological viewpoint. *Ann Trop Med Parasitol*., **100**(7), 551-570.

Mycek, M. A., & Progue, B. W., Eds. (2003). *Handbook of Biomedical Fluorescence*. Boca Raton, FL: CRC, 688.

Nabil, G. M. (2008). A biophysical study on hemoglobin molecule irradiated by near ultraviolet waves. *Global Veterinaria*, **2**, 165-168.

Nagai, M., Nagai, Y., Aki, Y., Imai, K., Wada, Y., Nagatomo, S., & Yamamoto, Y. (2008). Effect of reversed heme orientation on circular dichroism and cooperative oxygen binding of human adult hemoglobin. *Biochemistry Journal*, **15**, 517-25.

Nakamoto, K. (1977). *Infrared and Raman spectra of inorganic and coordination compounds*. Hoboken, New Jersey: John Wiley & Sons.

Narendran, N., Maliyagoda, N., Deng, L., & Pysar, R. M. (2001). "Characterizing LEDs for General Illumination Applications: Mixed-colour and phosphor -based white sources". *Proceeding of SPIE*, **65**, 4445-4450.

Narendran, N., Bullough, J., Maliyagoda, N., & Bierman, A. (2001). What's useful life for white LEDs?. *J. Illum. Eng. Soc.*, **30**, 57-70.

Nassir, S. (2006). Image Segmentation Based on Watershed and Edge Detection Techniques. Computer Science Department, Zarqa Private University, Jordan.

Nash, G. B., O'Brien, E., Gordon-Smith, E. C., & Dormandy, J. A. (1989). Abnormalities in the Mechanical Properties of Red Blood Cells Caused by Plasmodium Falciparum. *Blood*, **74**, No. 2, 855-861.

National Instruments[©] (NI). (2008)

National Instruments[©] (NI). (2010)

National Population Census. (2010). Retrieved from:

    http://www. ghana.gov.gh/census/phc2010.pdf

Nelson, L., & Cox, M. (2005). *Protein Function*. In: *Lehinger Principles of*

    Biochemistry, 4th Ed., Freeman W. H and Company, New York.

Nieves, J. L., Valero, E. M., Nascimento, S. M. C., Hernandez-Andres, J., &

    Romero, J. (2005). Multispectral synthesis of daylight using a

    commercial digital CCD camera. *Appl. Opt.*, **44**, 5696-5703.

Nieves, J. L., Valero, E. M., Nascimento, S. M. C., Hernandez-Andres, J.,

    & Romero, J. (2007). Recovering fluorescent spectra with an RGB

    digital camera and color filters using different matrix factorizations.

    Appl. Opt., **46**, 4144-4154.

Nischan, L. M., Joseph, R. M., Libby, J. C., & Kerekes, J. P. (2003). Active

    spectral imaging. *Lincoln Laboratory Journal*, **14**, No.1, 131-144.

Nishigaki, T., Wood, C. D., Shiba, K., Baba, S. A., & Darszon, A. (2006).

    Stroboscopic illumination using light-emitting diodes reduces

    phototoxicity in fluorescence cell imaging. *BioTechniques*, **41**, No. 2,

    191-197.

Nogueira, F., & da Rosario, V. E. (2010). Methods for assessment of

    antimalarial activity in the different phases of the Plasmodium life

    cycle. *Rev. Pan-Amaz Saude*, 109-124.

Ogawa, S., Lee, T. M., Kay, A. R., & Tank, D. W. (1990). Brain magnetic

    resonance imaging with contrast dependent on blood oxygenation.

    PNAS, **87**(24), 9868-9872.

O'Meara, W. P., McKenzie, F. E., Magill, A. J., Forney, J. R., Permpanich, B., Lucas, C., Gasser, R. A., & Wongsrichanalai, C. (2005). Sources of variability in determining malaria parasite density by microscopy. *American Journal of Tropical Medicine and Hygiene*, **73**, 593-598.

Ong, C. W., Shen, Z. X., Ang, K. K. H., Kara, U. A. K., & Tang, S. H. (2002). Raman microspectroscopy of normal erythrocytes and Plasmodium berghei-infected erythrocytes. *Appl. Spectrosc*., **56**, 1126-1131.

Opoku-Ansah, J. (2012). Development of a multispectral light emitting diode imaging microscope for malaria red blood cells diagnostics. Master of Philosophy Thesis, University of Cape Coast.

Opoku-Ansah, J., Eghan, M. J., Anderson, B., & Boampong, J. N. (2014). Wavelength Markers for Malaria (*Plasmodium Falciparum*) Infected and Uninfected Red Blood Cells for Ring and Trophozoite Stages. *Applied Physics Research*, **6**(2), 47-55.

Oppenheim, A. V., Schafer, R. W., & Buck, J. R. (1999). Discrete-time signal processing. Upper Saddle River, N.J., Prentice Hall.

Optronic Laboratories Inc. (2009). OL Series 700-80 high precision LED holders and Luxeon LED holders.

Otsu, N. (1979). A Threshold Selection Method from Gray-Level Histograms. *IEEE Transactions on Systems*, *Man and Cybernetics*, **9**, No. 1, 62-66.

Oyelade, O. J., Oladipupo, O. O., & Obagbuwa, I. C. (2010). Application of K-Means Clustering algorithm for prediction of Students' Academic Performance. *International Journal of Computer Science and Information Security (IJCSIS)*, **7**, No. 1, 292-295.

Palmer, J. M., & Grant, B. G. (2009). *The Art of Radiometry*. Vol: PM 184, SPIE PRESS, Bellingham, Washington, USA.

Pammenter, M. D. (1988). Techniques for the diagnosis of malaria. *S Afr Med J.*, **74**, No. 2, 55-57.

Park, Y., Yamauchi, T., Choi, W., Dasari, R. R., & Field, M. S. (2009). Spectroscopic phase microscopy for quantifying hemoglobin concentrations in intact red blood cells. *Optics Letters*, **34**, No. 23, 3668-3670.

Park, J. I., Lee, M. H., Grossberg, M. D., & Nayar, S. K. (2007). Multispectral imaging using multiplexed illumination. *IEEE 11th International conference on computer vision*, 1-8.

Park, Y. K., Diez-Silva, M., Fu, D., Popescu, G., Choi, W., Barman, I., Suresh, S., & Feld, M. S. (2010). Static and dynamic scattering of healthy and malaria-parasite invaded red blood cells. *J. Biomed. Opt.*, **15**(2), 020506.

Paton, D., Faragher, B., Mustaffa, K. M. F., Szestak, T., Barrett, S. D., & Craig, A. G. (2011). Automated counting for *Plasmodium falciparum* cytoadherence experiments. *Malaria Journal*, **25**, 10-91.

Payne, D. (1988).Use and limitations of light microscopy for diagnosing malaria at the primary health care level. *Bulletin of the World Health Organization*, **66**, No. 5, 621-626.

Peng, C., & Liu, J. (2013). Studies on Red-Shift Rules in Fluorescence Spectra of Human Blood Induced by LED. *Applied Physics Research*, **5**(1), 1-6.

Petersen, E., Marbiah, N. T., New, L., & Gottschau, A. (1996). Comparison of two methods for enumerating malaria parasites in thick blood films. *Am. J. Trop. Med. Hyg*., **55**, 485-489.

Petteri, T. (2008). *Multispectral Imaging. Course Project for AS-75.2128*. Imaging and Display Technology, Helsinki University of Technology.

Peyron, F. G., Martet, J. P., & Vigler, A. (1994). Dipstick antigen-capture assay for malaria detection. *Lancet*, **i**:1502-1503.

Pico Quant. (2011). Course on fluorescence techniques. Retrieved from http://www.picoquant.com

Pitas, I. (2000). *Digital Image Processing Algorithms and Applications*. Wiley- IEEE.

Planche, T., Krishna, S., Kombila, M., Engel, K., & Faucher, J. F. (2001). Comparison of methods for the rapid laboratory assessment of children with malaria. *Am* J. *Trop Med Hyg,* **65**, 599-602.

Platt, U., & Stutz, J. (Eds). (2008). Differential absorption spectroscopy. In Y. Kim, U. Platt, M. B. Gu, & H. Iwahashi. *Atmospheric and Biological Environmental Monitoring* (pp. 135-174). Heidelberg, Berlin: Springer.

Polglase, A. L., McLaren, W. J., Skinner, S. A., Kiesslich, R., Neurath, M. F., & Delaney, P. M. (2005). A fluorescence confocal endomicroscope for in vivo microscopy of the upperand the lower-GI tract. *Gastrointest Endosc*., **62**:686-695.

Pouratian, N., Cannestra, A. F., Martin, N. A., & Toga, A. W. (2002). Intraoperative optical intrinsic signal imaging: a clinical tool for functional brain mapping. *Neurosurg. Focus*, **13**(4): e1.

212

Prasad, P.N. (2003). *Introduction to biophotonics*, Hoboken, NJ: Wiley-
Interscience.

Premji, Z., Minjas, J. N., & Shiff, C. J. (1994). Laboratory diagnosis of
malaria by village health workers using the rapid manual ParaSight™-
F test. *Transactions of the Royal Society of Tropical Medicine and
Hygiene*, **88**(4), 418.

Raman, C. V., & Krishnan, K. S. (1928). A new type of secondary radiation.
Nature, **121**(3048), 501-502.

Ravichandran, K. S., & Ananthi, B. (2009). Colour skin segmentation using
K-means cluster. *International Journal of Computational and Applied
Mathematics*, ISSN 1819-4966, **4**, No. 2, 153-157.

Rayleigh, L. (1881). On the electromagnetic theory of light. *Philos. Mag.,*
12(73), 81, 101.

Richard, M., Paul, J., & Neal, R. (2002). *Spectral Imaging and Biomedicine*.
New Devices New Approaches, Proceedings of the 31st Applied
Imagery Pattern Recognition Workshop.

Richarme, M. (2002). Eleven multivariate analysis techniques: Key tools in
your marketing research survival kit, Decision analyst. *Strategic
Research*, *Analytics, Modeling and Optimization*, **25**, 11-16.

Roessler, M. (2002). How to find hidden cameras. Retrieved from
http://www.franken.de/users/tentacle/papers/

Rogier, C., & Trape, J. F. (1993). Malaria attacks in children exposed to high
transmission: who is protected?. *Transactions of the Royal Society of
Tropical Medicine and Hygiene*, **87**, 245-246.

Roithner Laser Techniques. (2011). GmbH Austria. Retrieved from

    http://www.roithner-laser.com

Romagosa, C., Menendez, C., Ismail, M. R., Quintó, L., Ferrer, B., Alonso, P.

    L., & Ordi, J. (2004). Polarisation microscopy increases the sensitivity

    of hemozoin and Plasmodium detection in the histological assessment

    of placental malaria. *Acta Trop*., **90**(3), 277-284.

Rosenthal, P. J., McKerrow, J. H., Aikawa, M., Nagasawa, H., & Nagasawa,

    J. H. (1988). A Malarial cysteine proteinase is necessary for

    hemoglobin degradation by Plasmodium falciparum. *J. Clin. Invest*.,

    The American Society for Clinical Investigation, **82**, 1560-1566.

Ross, J. R. (1967). *Constraints on variables in syntax*. PhD. Thesis,

    Massachusetts Institute of Technology, USA.

Ross, N. E., Pritchard, C. J., Rubin, D. M., & Duse, A. G. (2006). Automated

    image processing method for the diagnosis and classification of

    malaria on thin blood smears. *Medical and Biological Engineering*

    and Computing, **44**, 427-436.

Rowe, J. A., Obiero, J., Marsh, K., & Raza, A. (2002). Short report: positive

    correlation between rosetting and parasitemia in *Plasmodium*

    falciparum clinical isolates. *Am. J. Trop. Med. Hyg*., **66**, 458-460.

Ruebush, T. K., Kern, M. K., Cambell, C. C., & Oloo, A. J. (1995). Self-

    treatment of malaria in a rural area of western Kenya. *Bull. World*

    Health Org., **73**(2), 229-236

Sachs, J., & Melaney P. (2002). The economic and social burden of malaria.

    Malaria Journal, **415**, 680-685.

Saleh, B. E. A., & Teich, M. C. (2007). *Fundamentals of Photonics*. 2nd edition, John Wiley & Sons, 682-702.

Sarkar, D., Ray, S., Saha, M., Chakraborty, A., & Talukdar, A. (2013). Clinico-laboratory profile of severe Plasmodium vivax malaria in a tertiary care centre in Kolkata. *Trop Parasitol*, **3**, 53-57.

Sauer, M., Hofkens, J., & Enderlein, J. (2010). *Handbook of Fluorescence Spectroscopy and Imaging: From Ensemble to Single Molecules*. Weinheim, Germany: John Wiley & Sons.

Savkare, S. S., & Narote, S. P. (2011). Automatic Detection of Malaria Parasites for Estimating Parasitemia. *International Journal of Computer Science and Security (IJCSS)*, **5**, 310-315.

Schaepman, M. E., Ustin, S. L., Plaza, A. J., Painter, T. H., Verrelst, J., & Liang, S. (2009). Earth system science related imaging spectroscopy-An assessment. *Elsevier Inc*., *Remote Sensing of Environment*, **113**, 123-137.

Schmidt, M. H., Bajic, D. M., Reichert, K. W., Martin, T. S., Meyer, G. A., & Whelan, T. H. (1996). Light-emitting diodes as a light source for intraoperative photodynamic therapy. *Neurosurgery*, **38**, No. 3, 552-556.

Scholl, P. F., Kongkasuriyachai, D., Demirev, P. A, Feldman, A. B., Lin, J. S., Singh, N., Valencha, M., & Sharma, V. P. (1997). Malaria diagnosis by field workers using an immunochromatographic test. *Trans. R. Soc. Trop. Med. Hyg*., **91**, 396-397.

Schubert, E. F. (2006). *Light-Emitting Diodes*, 2nd Ed., Cambridge University Press, 432.

Sever, M., Lajovic, J., & Rajer, B. (2005). Robustness of the Fisher's Discriminant Function to Skew-Curved Normal Distribution. *Metodološki zvezki*, **2**, No. 2, 231-242.

Shahrooz, A. M., Park, Y., Lue, N., Dasari, R. R., Badizadegan, K., Fiueld, M. S., & Popescu, G. (2007). Microrheology of red blood cell membranes using dynamic scattering microscopy. *Optics Express*, **15**, No. 25, 11-19.

Sharma, G., & Trussell, H. J. (1997). Digital color imaging. *IEEE Trans. on Image Processing*, **6**(7), 901-932.

Shatkay, H. (1995). *The Fourier Transform*- A Primer. Department of Computer Science, Brown University, Providence, Rhode Island 02912.

Shekalaghe, S., Alifrangis, M., Mwanziva, C., Enevold, A., Mwakalinga, S., Mkali, H., Kavishe, R., Manjurano, A., Sauerwein, R., Drakeley, C., & Bousema, T. (2009). Research Article, Low Density parasitaemia, red blood cell polymorphisms and Plasmodium falciparum specific immune responses in low endemic area in northern Tanzania. *BMC Infectious Diseases*, 9-69.

Shelby, J. P., White, J., Ganesan, K., Rathod, P. K., & Chiu, D. T. (2003). A microfluidic model for single-cell capillary obstruction by Plasmodium falciparum-infected erythrocytes. *Proc Nat'l Acad Sci*, USA, **100**, 14618-14622.

Sigrist, M. W. (1994). *Air monitoring by spectroscopic techniques*. New York: John Wiley & Sons.

Sio, S. W. S., Sun, W., Kumar, S., Bin, W. Z., Tan, S. S., Ong, S. H., Kikuchi, H., Oshima, Y., & Tan, K. S. W. (2006). Malaria Count: An image analysisbased program for the accurate determination of parasitemia. *Journal of Microbiological Methods*, **68**, 8-11.

Sjöholm, M., Somesfalean, G., Alnis, J., Andersson-Engels, S., & Svanberg, S. (2001). Analysis of gas dispersed in scattering media. *Opt. Lett.,* **26**, 16 -18.

Slater, D., & Healey, G. (1999). Material Classification for 3D Objects in Aerial Hyperspectral Images. *Proc. Computer Vision and Pattern Recognition*, **2**, 268-273.

Small, D. S., Cheng, J., & Have, T. R. T. (2010). Valuating the efficacy of a malaria vaccine. *The International Journal of Biostatistics*, **6**(2), 1-20.

Soille, P. (2003). *Morphological Image Analysis: Principles and Applications*, Springer Verlag, Heidelberg.

Somesfalean, G., Andersson-Engels, S., & Svanberg, S. (2002). Concentration measurement of gas embedded in scattering media by employing absorption and time-resolved laser spectroscopy. *Appl. Opt*., **41**, 3539-3544.

Somesfalean, G. (2004). *Environmental Monitoring using Diode Laser Spectroscopic Techniques*. Phd Thesis, Lund Report on Atomic Physics, 329.

Spires, T. L., Meyer-Luehmann, M., Stern, E. A., McLean, P. J., Skoch, J., Nguyen, P. T., Bacskai, B. J., & Hyman, B. T. (2005). Dendritic spine abnormalities in amyloid precursor protein transgenic mice demonstrated by gene transfer and intravital multiphoton microscopy. *J. Neurosci.*, **25**, 7278-7287.

Špringl, V. (2009). *Automatic Malaria Diagnosis through Microscopy Imaging*. Diploma thesis, Czech Technical University, Faculty of Electrical Engineering, Prague.

Steinke, J. M., & Shepherd, A. P. (1986). Role of light scattering in whole blood oximetry. *IEEE Trans. Biomed. Eng.*, **33**, 294-301.

Steinke, J. M., & Shepherd, A. P. (1988). Comparison of Mie theory and the light scattering of red blood cells. *Appl. Opt.*, **27**, 4027-4033.

Stone, N., Kendall, C., Smith, J., Crow, P., & Barr, H. (2004). Near-infrared Raman spectroscopy for the classification of epithelial pre-cancers and cancers. *J. Raman Spectrosc.*, **33**, 564 573.

Stone, N., Kendall, C., Smith, J., Crow, P., & Barr, H. (2004). Raman spectroscopy for identification of epithelial cancers. *Faraday Discuss*, **126**, 141-57.

Stuart, B. H. (2004). *Infrared Spectroscopy: Fundamentals and Applications*. Wiley, United Kingdom.

Suh, M., Bahar, S., Mehta, A. D., & Schwartz, T. H. (2006). Blood volume and hemoglobin oxygenation response following electrical stimulation of human cortex. *Neuroimage*, **31**(1), 66-75.

Sullivan, D. J. Jr., & Kumar, N. (2004). Rapid detection of malaria infection in vivo by laser desorption mass spectrometry. *Am. J. Trop. Med. Hyg.,* **71***(5),* 546-551.

Sulzer, A. J., Wilson, M., & Hall, E. C. (1969). Indirect fluorescent antibody test for parasitic desease. An evaluation of a thick-smear antigen in the IFA test for malaria antibodies. *Am. J. Trop. Med. Hyg*., **18**, 199-205.

Sun, X., & Anderson, J. M. (1993). A Spatially Variable Light-Frequency-Selective Component-Based, Airborne Pushbroom Imaging Spectrometer for the Water Environment. *Photogrammetric Eng. & Remote Sensing*, **59**(3), 399-406, 1993.

Svanberg, S. (1992). *Atomic and molecular spectroscopy*, 2nd ed., Springer Verlag, Berlin.

Svanberg, S. (2004). *Atomic and Molecular spectroscopy*: Basic Aspects and Practical Applications, 4th ed., *Springer*, Berlin.

Svanberg, S. (2009). Optical analysis of trapped gas-gas in scattering media absorption spectroscopy. *Laser Physics*, **19**, 1-10.

Svanberg, S. (2012). *Atomic and molecular spectroscopy*, 6th ed., Springer Verlag, Berlin.

Svenson, J. E., MacLean, J. D., Gyorkos, T. W., & Keystone, J. (1995). Imported malaria: clinical presentation and examination of symptomatic travelers. *Arch Intern Med*., **155**, 861-868.

Teikari, P. (2008). Multispectral imaging. Course project for AS-75.2128 imaging and display technology, Helsinki University of Technology.

Tek, F. B., Dempster, A. G., & Kale, I. (2005). Blood cell segmentation using minimum area watershed and circle radon transformations. Mathematical Morphology*, Springer*, 441-454.

Tek, F., Dempster, A., & Kale, I. (2006). Malaria parasite detection in peripheral blood images. *Proceeding of British Machine Vision Conference*, 1-10.

Tek, F., Dempster, A., & Kale, I. (2009). Computer vision for microscopy diagnosis of malaria. *Malaria Journal*, **8**, 1-14.

Thomson, S. (2000). External Quality Assessment in the Examination of Blood Films for Malarial Parasites within Ontario, Canada. *Arch Pathology Laboratory Medicine*, **124,** 57-60.

Tou, J. T., &. Gonzalez, R. C. (1974). *Pattern Recognition Principles*, Massachusetts, Addison-Wesley.

Tran, C. D. (2000). Visualizing chemical composition and reaction kinetics by near infrared multispectral imaging technique. *J. Near-Infrared Spectrosc*., **8**, 87-99.

Tran, C. D. (2001). Development and analytical applications of multispectral imaging techniques. *Fresenius J. Anal. Chem.*, **369**, 313-319.

Tran, C. D. (2003). Infrared multispectral imaging: Principles and instrumentation. *Appl. Specrosc. Rev*., **38**, 133-153.

Tran, C. D. (2005). Principles, instrumentation and applications of infrared multispectral imaging, an overview. *Anal. Lett*., **38**, 735-752.

Tran, C. D., Grishko, V., & Challa, S. (2008). Molecular state and distribution of fullerenes entrapped in sol-gels by multispectral imaging techniques. *J. Phys. Chem. B*., **112**, 14548-14559.

220

Tran, C. D., & Kong, X. (2000). Determination of identity and sequence of tri- and tetrapeptides by near-infrared spectrometry. *Anal. Biochem*., **286**, 67-74.

Tran, C. D., Oliveira, D., & Grishko, V. (2004). Determination of enantiomeric composition of pharmaceutical products by near-infrared spectrometry. *Anal. Biochem*., **325**, 206-214.

Trape, J. F. (1985) Rapid evaluation of malaria parasite density and standardization of thick smear examination for epidemiological investigations. *Transactions of the Royal Society of Tropical Medicine and Hygiene,* **79**, 181- 184.

Tuchin, V. (2007). *Tissue Optics: Light Scattering Methods and Instruments for Medical Diagnosis*. 2nd ed., SPIE, Bellingham.

U.S. Department of Health and Human Services. (2007).Understanding Malaria. *NIH*, **7**, 7139.

Utzinger, U., & Richards-Kortum, R.R. (2003). Fiber optic probes for biomedical optical spectroscopy. *J. Biomed. Opt*., **8**(1), 121-147.

van de Hulst, V. H. C. (1981). *Light scattering by small particles*. Dover Publications Inc., New York.

Van Den Berg, F. M., Van Amstel, P. J., Janse, C. J., Meis, J. F. G. M., & Mons, B. (1991). Detection of different developmental stages of malaria parasites by non-radioactive DNA in situ hybridization. *Histochemical Journal*, **23**, 109-115.

Van Der Linden, A., Van Camp, N., Ramos-Cabrer, P., & Hoehn, M. (2007). Current status of functional MRI on small animals: Application to physiology, pathophysiology, and cognition. *NMR Biomed.*, **20**(5), 522-545.

Vennerstrom, J. L., & Eaton, J. W. (1988). Oxidants, Oxidant Drugs and Malaria. *Journal of Medical Chemistry*, **31**, 1269-1277.

Vo-Dinh, T. (2003). *Biomedical Photonics Handbook*, CRC Press LLC, New York.

Wang, H., & Chow, S. (2007). Sample size calculation for comparing proportions. *Wiley Encyclopedia of Clinical Trials; John Wiley & Sons, Inc.*

Warhurst, D. C., & Williams, J. E. (1996). Laboratory diagnosis of malaria. *Journal of clinical pathology*, **49**, 533-538.

Weatherall, J. D., Miller, H. L., Baruch, D. I., Marsh, K., Doumbo, K. O., Casals-Pascual, C., & Roberts, D. J. (2002). Malaria and the Red Cell. *American Society of Hematology*, 35-57.

Weissleder, R., & Ntziachristos, V. (2003). Shedding light onto live molecular targets. *Nat. Med.*, **9**,123-128.

Wellman, J. B. (1981). Multispectral Mapper: Imaging Spectroscopy as Applied to the Mapping of Earth Resources. *Proc. SPIE Imaging Spectroscopy*, **268**, 64-73.

Wilson, B. K., Behrend, M. R., Horning, M. P., & Hegg, M. C. (2011). Detection of malarial byproduct hemozoin utilizing its unique scattering properties. *Opt. Express,* **19**(13), 12190-12196.

Wolter, A. (1932). Uber die Schnelldiagnose der Malaria mit Hilfe des Dunkelfeldes. *Dermat. Zeitschrift*, **63**(1-2), 69-72.

Wongsrichanalai, C., Barcus, M. J., Muth, S., Sutamihardja, A., & Wernsdorfer, W. H. (2007). A review of malaria diagnostic tools: microscopy and rapid diagnostic test (RDT). *Am. J. Trop. Med. Hygiene*, **77**(Supply 6), 119-127.

Wood, B. R., Steven, J. L., Cooke, B. M., Glenister, F. K., Lim, J., & McNaughton, D. (2003). Raman imaging of hemozoin within the food vacuole of *Plasmodium falciparum* trophozoites. *FEBS Lett.*, **554**, 247-252.

Wood, B. R., Langford, S. J., Cooke, B. M., Lim, J., Glenister, F. K., Duriska, M., Unthank, J. K., & McNaughton, D. (2004). Resonance Raman spectroscopy reveals new insight into the electronic structure of *β*-hematin and malaria pigment. *J. Am. Chem. Soc.*, **126**, 9233-9239.

Wood, B. R., Hermelink, A., Lasch, P., Bambery, K. R., Webster, G. T., Khiavi, M. A., Cooke, B. M., Deed, S., Naumann, D., & McNaughton, D. (2009). Resonance Raman microscopy in combination with partial dark-field microscopy lights up a new path in malaria diagnostics. *Analyst (Lond.)*, **134**(6), 1119-1125.

World Health Organization (WHO). (1991). *Basic malaria microscopy Part I Learner's Guide* World Health Organization.

World Health Organization (WHO). (1996). Basic Malaria microscopy. World Health Organization Report, Geneva. Retrieved from http://www.who.int/Basic+Malaria+microscopy&0q

World Health Organization (WHO). (2000). New perspectives in malaria
    diagnosis. World Health Organization, Geneva, Switzerland. Retrieved
    from http://www.who/maI/2000.1091

World Health Organization (WHO). (2006). Guidelines for the Treatment of
    Malaria. Retrieved from
    http://www.who.int/guidelines+for+the+treatment+of+malaria+2006&
    oq

World Health Organization (WHO). (2010). World Malaria Report. Geneva.
    Retrieved from
    http://www.who.int/World+Health+Organization+(WHO).+(2010)

World Health Organization (WHO). (2010). Basic Malaria Microscopy: Part I.
    Learner's Guide, Second Edition, World Health Organization.

World Health Organization (WHO). (2013). World Malaria Report. World
    Health Organization.

Wozencraft, A. O. (1986). Oxygen radical release by adherent cell populations
    during the initial stages of a lethal rodent malarial infection,
    Immunology, **56**, No. 3, 523-531.

Yuval, G., Ian, T., & McNamara, G. (2006). Spectral Imaging: Principles and
    Applications.

Zijlstra, W. G., Buursma, A., & Meeuwsen-van der Roest, W. P. (1991).
    Absorption spectra of human fetal and adult oxyhemoglobin, de
    oxyhemoglobin, carboxyhemoglobin and met hemoglobin. *Clinical
    Chemistry*, **37**, 1633-1638.

APPENDICES

Appendix A

Letter of ethical approval from the Ghana Health Service Ethical Review Committee.

GHANA HEALTH SERVICE ETHICAL REVIEW COMMITTEE

In case of reply the number and date of this Letter should be quoted

Research & Development Division
Ghana Health Service
P. O. Box MB 190
Accra
Tel: +233-302-681109
Fax + 233-302-685424
Email: Hannah.Frimpong@ghsmail.org

My Ref. :GHS-ERC: 3
Your Ref. No.

31ˢᵗ July, 2014

Jerry Opoku-Ansah
UCC
Cape Coast

ETHICAL APPROVAL - ID NO: GHS-ERC: 09/05/14

The Ghana Health Service Ethics Review Committee has reviewed and given approval for the implementation of your Study Protocol titled:

"Optical spectroscopic characterization of plasmodium falciparum infected and uninfected red blood cells"

This approval requires that you inform the Ethical Review Committee (ERC) when the study begins and provide Mid-term reports of the study to the Ethical Review Committee (ERC) for continuous review. The ERC may observe or cause to be observed procedures and records of the study during and after implementation.

Please note that any modification without ERC approval is rendered invalid.

You are also required to report all serious adverse events related to this study to the ERC within seven days verbally and fourteen days in writing.

You are requested to submit a final report on the study to assure the ERC that the project was implemented as per approved protocol. You are also to inform the ERC and your sponsor before any publication of the research findings.

Please always quote the protocol identification number in all future correspondence in relation to this approved protocol

SIGNED...
DR. CYNTHIA BANNERMAN
(GHS-ERC VICE-CHAIRPERSON)

Cc: The Director, Research & Development Division, Ghana Health Service, Accra

Appendix I: Copy of approved letter from Ghana Health Service Ethical Review Committee (GHS-ERC-09/05/14).

225

Appendix B

Sample size calculation

The sample size, 360, was calculated using the following method as described in (Chavchich, et al., 2010; Eastman et al., 2011);

$$n = \frac{z^2 pq}{d^2}$$

where n = the desired sample size (when population is greater than 10,000); z = the standard normal deviation, usually set at 1.96, which corresponds to the 95% confidence interval; p = the proportion in the target population estimated to have a particular characteristic(s). If there is no reasonable estimate, then 50% is used; $q = 1.0 - p$; d = degree of accuracy desired, usually set at 0.05 level or occasionally at 0.02.

Each selected site has population greater than 10, 000. The standard deviation (z) was set at 1.96, which corresponds to the 95% confidence level. 37.5% outpatient department (OPD) prevalence of malaria (Fischer, et al., 1998) was used as the proportion in the target population estimated to have a particular characteristic (which, in this case is malaria)(p).

Therefore p = 0.375, and q = 1-0.375 = 0.625. The degree of accuracy was set at 0.05. Hence,

$$n = \frac{z^2 pq}{d^2} = \frac{(0.96)^2 (0.375)(0.614)}{(0.05)^2} = \frac{3.8416 x 0.234375}{0.0025} = \underline{\mathbf{360}}$$

PUBLICATIONS

Jerry Opoku-Ansah, Moses Jojo Eghan, Benjamin Anderson, Johnson
Nyarko Boampong & Paul Kinsley Buah-Bassuah. (2016). Laser-
Induced Auto-fluorescence for *Plasmodium falciparum* Parasite
Density Estimation. *Applied Physics Research*, **8**(2), 43-51.
http://dx.doi.org/10.5539/apr.v8n2p43

Jerry Opoku-Ansah, Moses Jojo Eghan, Benjamin Anderson & Johnson
Nyarko Boampong. (2014). Wavelength Markers for Malaria
(P.Falciparum) Infected and Uninfected Red Blood Cells at Ring and
Trophozoite Stages. *Applied Physics Research*, **6**(2), 47-55.
http://dx.doi.org/10.5539/apr.v6n2p47

.